The Dynamics of Near-Surface Dust on Airless Bodies

by

Christine M. Hartzell

B.S., Aerospace Engineering (Highest Honors)

Georgia Institute of Technology, 2008

A thesis submitted to the

Faculty of the Graduate School of the

University of Colorado in partial fulfillment

of the requirements for the degree of

Doctor of Philosophy

Department of Aerospace Engineering Sciences

2012

This thesis entitled:
The Dynamics of Near-Surface Dust on Airless Bodies
written by Christine M. Hartzell
has been approved for the Department of Aerospace Engineering Sciences

Dr. Daniel Scheeres

Dr. Joshua Colwell

Dr. Mihály Horányi

Dr. Hanspeter Schaub

Dr. Zoltan Sternovsky

Date

The final copy of this thesis has been examined by the signatories, and we find that both the content and the form meet acceptable presentation standards of scholarly work in the above mentioned discipline.

Hartzell, Christine M. (Ph.D., Aerospace Engineering Sciences)

The Dynamics of Near-Surface Dust on Airless Bodies

Thesis directed by Dr. Daniel Scheeres

The behavior of dust particles under the influence of electrostatic forces has been investigated near the surface of asteroids and the Moon. Dust particle motion on airless bodies has important implications for our understanding of the evolution of these bodies as well as the design of future exploration vehicles. Electrostatically-dominated dust motion has been hypothesized to cause the observed Lunar Horizon Glow and dust ponds on the asteroid Eros.

The first major contribution of this thesis is the identification of the electric field strength required in order to electrostatically loft dust particles off the surface of the Moon and asteroids Eros and Itokawa, taking into account the gravity of the body (assumed to be spherical) and the cohesion between dust grains (assumed to have the material properties of lunar regolith). In order to solve for the electric field strength required as a function of dust particle size (assumed to be spherical), we assumed that the charge on the dust particle was given by Gauss law. It can be seen that it is easiest to launch intermediate-sized particles, rather than the submicron-micron sized particles that have been previously considered due to the dominance of cohesion for small particle sizes. Additionally, the electric field strength required to loft particles is orders of magnitude larger than is likely to be present *in situ*, unless grain charging is amplified beyond the levels predicted by Gauss' law.

The significance of cohesion in electrostatic dust lofting has also been demonstrated experimentally. Piles of uniformly sized dust grains are placed on a biased conducting plate in a plasma. We see that the pile of 15 micron dust spreads more than piles of 5, 10, 20, and 25 micron dust grains. This observation confirms our theory-based prediction of the importance of cohesion for small grain sizes. The experimental proof presented also has implications for interpretations of horizon glow observations and studies of electrostatic dust lofting feasibility.

The dynamics of dust particles moving in the plasma sheath, independent of the launching mechanism, is of interest since dust particle levitation could significantly change our understanding of the evolution of asteroids as well as pose a hazard to future exploration vehicles. By studying the levitation behavior in a 1D system for a range of particle sizes, a range of central body masses and three different plasma sheath models, we have gained a more detailed understanding of the drivers of the dynamics of the particles. The equilibria about which dust particles are expected to levitate are identified. The equilibria can be generalized to non-spherical grains (as actual lunar and asteroidal grains are highly angular) by presenting the results as a function of the particles charge-to-weight ratio. Notably, we see that the behavior of levitating dust is driven by the particle size rather than the mass of the central body. Additionally, we can begin to constrain the range of initial launching conditions that result in levitation.

Finally, we expand our 1D analysis of dust levitation to a 3D system. Due to the rotation of the central body (particularly with fast rotating asteroids), the plasma environment will be changing radically through a particle's trajectory. Additionally, asteroids have highly non-spherical shapes, thus variations in the bodys gravity may significantly influence the trajectory of a given particle. For the case of a spherical asteroid, it can be seen that the time variation of the plasma environment will not cause the particle to reimpact prematurely. We also find that the transverse electric fields present in a 3D model noticeably influence particle trajectories.

This thesis presents detailed investigations of electrostatic dust lofting and the dynamics of electrostatic levitation. The results have implications for understanding the evolution of airless bodies, the interpretation of spacecraft observations, and the design of future spacecraft. It is possible to expand the experimental work presented here by testing the influence of grain shape and polydispersity on electrostatic dust lofting. Our theoretical studies of dust levitation in a 3D model could be improved by using an accurate asteroid shape model coupled with a high fidelity plasma simulation.

Dedication

To my horses, Lylly, Chyna and Nick, who taught me about success and failure, love and loss, courage, and the value of hard work.

Acknowledgements

I could not have completed this research without the assistance of my advisor Dr. Dan Scheeres. Dan's continual efforts to understand me when I was far from eloquent, his belief in my abilities when I was unsure, his calm when I was stressed, and his understanding when 'life' got in the way of 'research' made my journey to the PhD possible. 'Thank you' does not seem sufficient.

I would also like to thank my committee: Dr. Josh Colwell, Dr. Mihály Horányi, Dr. Hanspeter Schaub, and Dr. Zoltan Sternovsky. The experimental work discussed in this dissertation would not have happened without the guidance of Dr. Xu Wang, who decided to give my experiment (and me) a chance. Thank you also to Dr. Erian Armanios and Dr. Charles Norton for their invaluable mentoring.

I never would have made it to grad school without the support of my biggest cheerleader, my mom, Joanne Hartzell. Although Mom tells me that she never sacrificed for me, I would like to thank her for working hard to stay alive. I would also like to thank her oncologist, Dr. Saul Rivkin, for helping her slow the progression of her cancer to see me through this journey.

To Dmitriy Bekker - thank you for providing an island of normalcy in my life, for joining frequent flyer programs, clipping coupons, and going along with my various crazy ideas.

Thank you also to the rest of my family: Barry Hartzell, Judy Weber, Sheryl and Craig Hansen, Linda and Steve Tilford, Bill Rockenfeller and the rest of the village that raised me. Thanks to my friends: Dr. Aurore Sibois, Dr. Andy Klesh, Dr. Paul Sanchez, Simon Tardivel, Dr's Holzinger and McMahon (who mainly teased me and resisted my purchase of a lab couch), and the rest of the Celestial and Spaceflight Mechanics Lab.

Contents

Chapter

Tables

Table

Figures

Figure

Chapter 1

Introduction and Motivation

Electrostatically dominated dust motion has been hypothesized to occur since the Lunar Horizon Glow was observed by the Surveyor spacecraft [43]. The Lunar Horizon Glow, observed after the spacecraft had pass through local sunset, was thought to be caused by light scattering off of 10 micron diameter dust particles floating above the lunar surface. According to Rennilson and Criswell's [43] analysis, the flux of dust particles emitted during micrometeoroid bombardment was too low to account for the density of dust grains observed (interpreted as $50/\text{cm}^2$). Thus, it was hypothesized that these dust particles were ejected from the surface due to electrostatic forces.

Additional evidence for the motion of small, charged dust grains above the surface of the Moon was observed after Apollo 17. During Apollo 17, the Lunar Ejecta and Micrometeorite (LEAM) instrument was placed on the lunar surface. Although this instrument was designed to detect charged interplanetary dust impacting the lunar surface, the anomalous data received was interpreted as the result of impacts of charged dust grains of lunar origin [2, 3, 19]. The LEAM instrument was turned off during the lunar day to prevent overheating. Most impacts detected by the instrument occurred near lunar sunrise and sunset [2]. Astronaut observations of light streaks above the lunar horizon (the so-called 'lunar streamers') during Apollo 17 have also been attributed to electrostatic dust motion [62].

The surfaces of the Moon and other airless bodies (such as asteroids) interact with the solar wind plasma and the solar UV radiation. The solar UV radiation causes the surfaces of these bodies to emit electrons. Taking into account the interaction of the surface of these bodies with

the solar wind plasma and the solar wind UV radiation, the day sides of these bodies are generally positively charged. Since the night sides of the bodies are not exposed to the UV radiation, and thus do not photoemit, the night sides are generally negatively charged. The dusk/dawn regions (called the terminator region) undergo more complex charging and will be discussed in more detail in Chapter 2. Considering the day side of an airless body, electrons in the solar wind plasma will be attracted to the positively charged surface. Thus, although plasmas typically have the same number density of positively and negatively charged species, there will be a higher density of electrons than positively charged ions near the surface. Moving away from the surface, the density of the electrons decreases until the density of electrons is equal to the density of the ions. This variation in the density of the electrons and ions (called the plasma sheath) gives rise to an electric field that is pointing away from the surface. Since the dust grains on the surface are charged, they feel an electrostatic force equal to the product of the dust grain's charge and the electric field. If the electrostatic force is large enough to overcome the retarding forces that hold the dust particle on the surface, then the dust particle detaches from the surface and is said to be 'electrostatically lofted'. Once the particle detaches from the surface, its motion is controlled by gravity and electrostatic forces. Note that both the particle charge and the electric field that it experiences change with its location above the surface. Computational studies have shown that under certain conditions dust particles can hover above the surface, called 'electrostatic levitation'.

Since electrostatic dust motion had been hypothesized to occur on the Moon, it was naturally extended to asteroids [32], which have much lower surface gravities than the Moon. The main observational evidence for electrostatic dust motion on asteroids is the Eros dust ponds observed by the Near Earth Asteroid Rendezvous (NEAR) mission [47]. The Eros dust ponds are simply collections of fine grains in the bottoms of craters on the asteroid Eros. It has been suggested that electrostatic dust motion could have preferentially deposited small grains in these craters [47].

None of the extant observational evidence for electrostatically-dominated dust motion definitively proves that that electrostatic lofting or electrostatic levitation occur *in situ*. It may be possible to explain the existing observational data with other phenomena, including dust lofting

during micrometeoroid bombardment in the case of Lunar Horizon Glow or mass wasting in the case of the Eros dust ponds. The topic remains controversial in the planetary science community [31]. However, if electrostatically-dominated dust motion does occur, it will have important implications for both our understanding of the evolution of airless bodies and the design of future exploration vehicles.

If electrostatically-dominated dust motion occurs on airless bodies, it will provide a method to redistribute regolith across the surfaces of these bodies. Thus, understanding electrostatic dust motion will give us a more complete understanding of the evolution of the surfaces of these bodies. It is necessary to understand the electrostatic motion of dust in order to correctly interpret future limb observations of these bodies. Additionally, if electrostatic dust lofting occurs, it could have significant implications for the design of surface exploration vehicles. For instance, electrostatically lofted dust could coat surface vehicles, as has been observed with the Mars rovers, which decreases the efficiency of solar panels and thermal control devices. Electrostatic methods that rely on artificially charging surface dust grains have been suggested to clear dust from spacecraft [5]. However, the trajectories of these artificially charged grains after removal from the spacecraft have not been studied. If the ejected grains levitate near the spacecraft, science observations may be contaminated. Finally, surface operations on asteroids are likely to eject small plumes of dust. Again, if these plumes do not settle quickly, science observations could be negatively impacted. Thus, we are interested in understanding the feasibility and characteristics of electrostatic dust motion due to the implications for both planetary science and the design of future exploration vehicles.

This thesis is concerned with two general topics: electrostatic dust lofting and electrostatic dust levitation. As mentioned previously, there is no conclusive evidence that either of these phenomena actually occur *in situ*. We have conducted theoretical and experimental studies to understand the conditions under which electrostatic lofting and levitation will occur. This work will inform future efforts to detect these phenomena, understand the evolution of airless bodies, and design future exploration vehicles. The four main contributions of this work are:

- A theory for the dust particle size most likely to be electrostatically lofted, considering the effects of cohesion.
- Experimental validation of the effects of cohesion in electrostatic lofting.
- A theoretical framework for understanding what range of launching conditions lead to electrostatic levitation in a 1D system and what size dust particles are capable of levitation.
- An understanding of the influence of rotation and changing plasma environment on electrostatic levitation.

Thesis Statement

Applying engineering analysis techniques to study the motion of dust particles under the influence of electrostatic forces near airless bodies will increase our understanding of the feasibility and implications of electrostatic dust lofting and electrostatic levitation. Cohesion is significant when calculating the electric field necessary to electrostatically loft particles smaller than 100 microns on the Moon and asteroids. As a result, smaller electric fields are required to loft intermediately-sized particles than larger or smaller particles. The equilibrium heights, charges, and size range of levitating dust particles can be numerically identified given a central body and depend on the plasma sheath model used. From the equilibria, the timescales of levitation can be identified and the behavior of levitating grains and range of initial launching conditions resulting in levitation can be predicted. Levitation is not impeded by a continuously varying plasma environment.

Publications

The publications directly and tangentially related to this thesis are listed below for reference.

Journal Articles

- C. Hartzell, X. Wang, D. Scheeres, M. Horányi. "Experimental Demonstration of the Dominance of Cohesion in Electrostatic Lofting of Small Dust Grains" In Preparation.

- C. Hartzell, D. Scheeres. "Dynamics of Levitating Dust Particles Near Asteroids and the Moon" In Preparation.

- C. Hartzell, D. Scheeres. "The Role of Cohesive Forces in Particle Launching on the Moon and Asteroids" *Planetary and Space Sciences*. 2011. Vol 59, pp 1758-1768.

- D. Scheeres, C. Hartzell, P. Sánchez, M. Swift. "Scaling Physics to Asteroid Surfaces: The Role of Cohesion" *Icarus*. 2010. Vol 210, pp 968-984.

- J.R. Masiero, C.M. Hartzell, D.J. Scheeres. "The Effect of the Dust Size Distribution on Asteroid Polarization" *The Astronomical Journal*. Dec. 2009. Vol 139, pp 1557-1562.

Conference Papers

- C. Hartzell, D. Scheeres. "Studies of 3D Dust Motion about Asteroids" *IEEE Aerospace Conference*. March 2012.

- C. Hartzell, D. Scheeres. "Implications of Electrostatics and Cohesion for Asteroid Surface Exploration" *IEEE Aerospace Conference*. March 2011.

- C. Hartzell, D. Scheeres. "Dynamics of Levitating Dust Particles near Asteroids" *AIAA/AAS Spaceflight Mechanics Conference*. Feb 2011.

Conference Abstracts

- C. Hartzell, X. Wang, D. Scheeres, M. Horányi. "Experimental Demonstration of the Importance of Cohesion in Electrostatic Lofting of Small Grains". *Workshop on the Physics of Dusty Plasmas*. May 2012.

- C. Hartzell, D. Scheeres. "Understanding 1D Dust Levitation" *American Geophysical Union Fall Meeting*. December 2011. Poster.

- C. Hartzell, D. Scheeres. "Dynamics of Levitating Dust Near Equilibria on Asteroids" *Division of Planetary Sciences (AAS) Conference*. October 2011.

- C. Hartzell, D. Scheeres. "Granular Mechanics and Dusty Plasmas" Contributed Talk. *Granular Flows: From Simulations to Astrophysical Applications.* June 2011.

- C. Hartzell, D. Scheeres. "Electrostatic Dust Launching Methods" *Division of Planetary Sciences Conference.* October 2010.

- C. Hartzell, D. Scheeres. "The Significance of Cohesive Forces in Understanding Planetary Electrostatic Dust Lofting" *Scientific Assembly of the Committee on Space Research.* July 2010.

- C. Hartzell, D. Scheeres. "The Implications of Lunar Water on Electrostatic Dust Levitation" *Lunar and Planetary Science Conference.* March 2010. Poster.

- C. Hartzell, D. Scheeres. "The Dynamics of Electrostatically Levitated Particles from Asteroids" *Lunar Dust, Plasma and Atmosphere: The Next Steps Meeting.* January 2010.

- C. Hartzell, D. Scheeres. "The Dynamics of Dust Levitated from Asteroids" *Division of Planetary Sciences Conference.* October 2009. Poster.

Chapter 2

Literature Review

The prior relevant research can be broken into three categories, based on the research method used. Observational evidence for electrostatic dust motion on planetary bodies is perhaps the most import, but weakest of these investigations. There have been a number of solid computational studies of electrostatic levitation. There is also a large body of experimental work that mainly proves the feasibility of these phenomena in the laboratory environment, but cannot prove its existence in relevant planetary environments. The strengths and weaknesses of the prior research will be discussed in detail here and briefly refreshed at the beginning of the relevant chapters.

2.1 *In-Situ* Observations

2.1.1 Moon

As mentioned in Chapter 1, the first evidence for electrostatic dust levitation was the Lunar Horizon Glow observed by the Surveyor spacecraft [43]. It was suggested that electrostatically lofted 10 micron diameter dust particles caused the glow seen above the lunar horizon after local sunset. Electrostatic lofting was hypothesized since Rennilson and Criswell's calculations showed that the flux of micrometeoroid bombardment on the lunar surface was not great enough to produce the required density of lofted dust grains [43]. The Surveyor data has recently been reanalyzed by Glenar *et al.* [19] and only one of the five Surveyor observations previously interpreted as showing Lunar Horizon Glow has been confirmed as Horizon Glow during reanalysis.

The Lunar Ejecta and Micrometeoroid instrument was placed on the lunar surface during

Apollo 17 [3]. The instrument carried three sensors, facing up, West and East [2]. Although initially designed to measure cosmic dust particles, the anomalous results of the LEAM instrument have been interpreted as the impact of charged lunar dust particles [2]. The instrument was turned off during to the lunar day to avoid overheating. The instrument sensed the most impacts around the lunar sunrise and sunset [2].

Similar to the Lunar Horizon Glow, astronauts on Apollo 17 observed streaks of light 5-20 km above the lunar surface [62]. It was hypothesized that the so-called 'lunar streamers' were caused by electrostatically lofted 0.2 micron (diameter) dust particles. The only records of the 'lunar streamers' are found in astronaut sketches.

2.1.2 Asteroids

The main observational evidence of electrostatic dust motion on asteroids are the 'dust ponds' on the asteroid Eros, observed by the NEAR mission [47]. The NEAR mission observed that some of the craters on Eros were filled with very small dust particles. The dust particles are known to be smaller than a centimeter in diameter, which is the highest resolution image captured by the NEAR mission. Additionally, the dust ponds have a higher 550nm to 760nm reflectance ratio than the surrounding surface, which could be caused by light scattered off of grains smaller than 50 microns [47]. Thus, it was suggested that electrostatic forces may have caused small dust grains to be deposited in the craters. The preferential deposition of dust grains in craters has been confirmed through numerical simulations [13, 28]. Seismic shaking is an alternate formation mechanism for the Eros dust ponds [10].

The Hayabusa mission visited the asteroid Itokawa. Itokawa has few well-defined craters and no evidence of dust ponding. However, some regions of Itokawa are covered with small grains, while others appear to be covered in boulders [36]. While no strong evidence for electrostatic dust motion on Itokawa exists, there is some anecdotal evidence [61]. Upon Hayabusa's initial descent to Itokawa's surface, the spacecraft autonomously executed an obstacle avoidance maneuver [61]. This may have been due to the spacecraft's detection of dust above the asteroid's surface. Additionally,

the Hayabusa mission was designed to collect surface material by shooting a projectile into the surface [18]. Despite the projectile not being fired, the spacecraft was able to collect 10-50 micron dust particles [30]. The collection of grains of this size may have been influenced by electrostatic forces.

The most recent evidence of asteroid regolith motion has been observed on Lutetia. It has been hypothesized that the mass wasting observed on Lutetia is a result of seismic shaking and gravity slopes [53]. However, electrostatic dust motion may also be important in the movement of regolith grains on this body.

2.2 Computational Studies

Criswell and De [15, 14] were the first to explore the electrostatic environment near the terminator of the Moon, a topic that remains challenging today. The goal of their work was to determine what electric field was likely to be present in the terminator region. In [15, 14], they use a simple numerical model to calculate the electric field near a protrusion in a static terminator environment and near a moving shadow. It was found that the electric field in both the static and time varying terminator environments could be as much as 1000 V/cm [15]. The electric fields calculated in these papers are likely optimistic since the neutralizing current is neglected.

P. Lee [32] was the first to suggest that electrostatic dust lofting could occur on asteroids. His calculations considered gravity and a simplistic understanding of the electrostatic environment near an asteroid's surface. Lee did not consider the cohesion between dust grains and the surface [32]. Additionally, the electric field was essentially modeled as constant with altitude.

Colwell *et al.* have studied the dust levitation and motion into craters [13, 28] using a simplified, monotonically-decreasing sheath potential model. These papers showed that dust levitation was possible and could result in particles being deposited in craters. In these papers, dust particles were launched with an arbitrary range of initial velocities and launch angles. Thus, the particle launching conditions may not be representative of those *in situ*.

Nitter *et al.* present detailed derivations of the plasma environment near the surface of airless

bodies and show trajectories of levitating dust grains [38]. The potential profiles and dust charging currents given by [38] will be used extensively in this work. Nitter *et al.* have also studied the case of levitation of multiple charged grains [37].

Poppe and Horányi [42] used a 1D Particle-In-Cell (PIC) code to study the plasma sheath near the Lunar surface, given a non-Maxwellian photoelectron distribution function. Additionally, dust grains were levitated in this model, assuming a constant gravitational acceleration and considering discretized grain charging [42]. In [41], a PIC code was used to show that non-monotonic sheaths were consistent with Lunar Prospector measurements of the plasma potential above the Lunar surface.

Sternovsky *et al.* [55] showed that photoemission varies with varying UV intensity, which has implications for electrostatically-dominated dust activity on airless bodies.

2.3 Experimental Investigations

Sheridan *et al.* [50, 17] conducted the first experiment that showed that electrostatic lofting was possible. A conducting sphere was covered in dust and then rotated in a plasma. It was seen that dust particles would detach from the top of the sphere when exposed to the plasma and an electron beam, but there was no dust loss when the plasma was turned off. Thus, it was shown that electrostatic dust lofting is physically possible. This experiment made no attempt to control the cohesion of the sample and alumina dust grains were used [50].

Sickafoose *et al.* [52] experimentally produced dust particle levitation. In addition to demonstrating that electrostatic levitation is possible, this study was one of the few to discuss the cohesion between dust grains in electrostatic lofting. Sickafoose *et al.* saw that at high enough plate potentials (which correspond to electric field strength), particles were electrostatically lofted and mechanical agitation was not required.

Wang *et al.* [59] also definitively demonstrated electrostatic dust lofting. A pile of Mars regolith simulant (used due to its easy visibility) was placed on a conducting plate in a plasma next to a small insulating block. The plate was biased and it was seen that the pile of dust spread

and coated the side and top of the insulating block. Thus, it was demonstrated that the dust did undergo some vertical motion. Additionally, Wang *et al.* [60] experimentally proved that the time variation in the illumination conditions (for instance, at the terminator during sunset) can cause increased charging on a surface, as had been previously hypothesized by [14].

2.4 Summary

In situ observations suggest that electrostatic dust motion may occur. However, each observation that may be explained by electrostatic dust motion could also be explained by other phenomena. Electrostatic dust motion is simply a unifying theory that may explain several characteristics of airless bodies. Computational studies have focused on either a) directly proving the feasibility of producing a specific physical characteristics (such as the Eros dust ponds) or b) developing a better model of the plasma environment. In this thesis, I instead focus on developing a more complete and general understanding of the dynamics of levitating grains and electrostatic dust lofting. Experimental studies have demonstrated the feasibility of electrostatic dust lofting and levitation (both of which had been predicted by theory). Experimental studies have also attempted to measure that which is left unexplained by theory; most notably, grain charging. In this thesis, we use experimentation to prove and calibrate our theoretical results concerning dust lofting.

Chapter 3

Electrostatic Dust Lofting

Significant uncertainty exists as to the physical mechanism through which particles are released from the surfaces of airless bodies. Previous numerical simulations of particle motion [13, 28] have launched particles with a specific velocity and zero initial charge, which is unphysical since electrostatic lofting is directly due to the charge of the dust grain. Subsequent particle behavior is very sensitive to the state of the particle (i.e., its charge and velocity) at the time when the particle leaves the surface. Specifically, over a certain range of initial velocities particles are seen to levitate, while at other initial velocities ballistic motion is observed. Without tying the modeled initial conditions to physical launching phenomena, it is difficult to predict the actual behavior of particles in the lunar and asteroid environments. We will demonstrate that there exists a discrepancy between the amount of electrostatic force required to launch particles and the electrostatic environment, as it is currently understood, on the lunar surface when particle charging is assumed to be dictated by Gauss' law. Additionally, we will show that there is a preferential size of particle for electrostatic lofting to occur. Specifically, particles on the order of hundreds of microns or larger are more likely to be electrostatically launched than submicron particles, due to the effects of cohesive forces. We also discuss the limited influence of seismic shaking on particle lofting and the scaling of these results to asteroids. We will show that cohesion remains an important force when determining the electric field strength required to loft particles even if the charging of dust particles is amplified beyond the levels predicted by Gauss' law, as has been suggested by experimental results. The inclusion of cohesion may be an important factor in the still poorly understood physics of dust

particle lofting on airless bodies.

3.1 Particle Equations of Motion

A dust particle resting on the surface of an airless body is subject to four forces: gravity (F_{grav}), cohesion (F_{co}), electrostatics (F_{es}), and the normal force (N). A diagram of a dust particle resting on a planar surface can be seen in Figure 3.1.

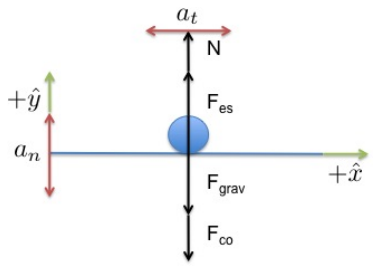

Figure 3.1: Particle resting on planar, sunlit surface, subject to gravity, cohesion, electrostatics and the normal force. Note that the magnitude of the normal force depends on the acceleration of the planar surface (a_t, a_n). The electrostatic force is assumed to be directed upwards. The positive directions ($\hat{x}$, $\hat{y}$) have been indicated.

As a first order approximation for seismic activity, we model every point on the planar surface to have both vertical and horizontal sinusoidal acceleration:

$$\mathbf{a} = A_t \sin(\Omega_t t)\hat{x} + A_n \sin(\Omega_n t)\hat{y} \tag{3.1}$$

where A_t is the amplitude of the transverse oscillations, A_n is the amplitude of the normal accelerations, and Ω indicates the frequency of the oscillation. We define the instantaneous transverse (a_t) and normal (a_n) accelerations of the surface:

$$a_t = A_t \sin(\Omega_t t) \tag{3.2}$$

$$a_n = A_n \sin(\Omega_n t) \tag{3.3}$$

The vertical equation of motion for a particle resting on the accelerating surface (assuming positive vertical acceleration to be in the upwards direction and $A_t = 0$) is:

$$m_d \ddot{y}_{rel} = F_{es} + F_{grav} + F_{co} + N - m_d a_n \tag{3.4}$$

where m_d is the mass of the dust particle and $\ddot{y}_{rel}$ is the vertical acceleration of the dust particle with respect to the accelerating planar surface. The equation of motion of the particle in the inertial frame is:

$$m_d\ddot{y}_i = m_d\ddot{y}_{rel} + m_d a_n \tag{3.5}$$

If the particle remains in contact with the planar surface, then it has the same vertical acceleration as the surface ($\ddot{y}_{rel} = 0$). If the acceleration of the particle is larger than that of the plane ($\ddot{y}_{rel} > 0$), then the particle will separate from the plane and the normal force will be zero. Once the particle has separated from the planar surface, the cohesive force is no longer active and the equation of motion of the particle is given by:

$$m_d\ddot{y}_i = F_{es,gen} + F_{grav} \tag{3.6}$$

assuming that the particle does not have any further interactions with the seismically active surface. $F_{es,gen}$ is the general form of the electrostatic force ($F_{es,gen} = QE$, where Q is the time- and height-dependent particle charge).

Although a given particle has separated from the surface ($\ddot{y}_{rel} > 0$), its inertial acceleration may be negative ($\ddot{y}_i < 0$). Henceforth, the condition for separation of a particle from the surface is $\ddot{y}_{rel} > 0$ and the condition for the particle to be launched from the surface is $\ddot{y}_i > 0$. Note that if there is no seismic shaking, $\ddot{y}_{rel} = \ddot{y}_i$ and the conditions for separation and launching are identical. Additionally, the initial velocity of the particle depends on the velocity of the surface at the time of separation. For instance, a particle could have a positive initial velocity with a negative initial acceleration if it is separated from the surface on the upstroke of the seismic activity. If the particle separates from the surface on the seismic acceleration downstroke, it will have a negative initial velocity, but could have a positive or negative initial acceleration. The behavior of the particle once separated from the surface has complicated dynamics that will be discussed in Chapter 5 and Chapter 6. The distinction between particle separation ($\ddot{y}_{rel} > 0$) and particle launching ($\ddot{y}_i > 0$) will be discussed due to its potential implications on the lateral distance traveled by the particle.

Seismic motion may also have a sinusoidal horizontal component (a_t). For a particle that is

in contact with a surface undergoing both normal and transverse seismic accelerations, there will be a horizontal friction force in addition to the vertical forces shown in Figure 3.1. The horizontal equation of motion of the transverse position of the particle with respect to the accelerating frame ($\ddot{x}_{rel}$) will be given by:

$$m_d \ddot{x}_{rel} = \zeta \mu N - m_d a_t \tag{3.7}$$

where μ is the coefficient of friction (which is admittedly related to the cohesive force). Since the maximum value of the friction force is μN, ζ is a scaling factor from zero to one that is included to accurately model the force on the particle. Substituting the normal force from Eq. (3.4) (assuming $\ddot{y}_{rel} = 0$) into Eq. (3.7), gives us the expanded equation of motion:

$$m_d \ddot{x}_{rel} = \zeta \mu \left(m_d a_n - F_{es} - F_{grav} - F_{co} \right) - m_d a_t \tag{3.8}$$

If $\ddot{x}_{rel} = 0$, the particle remains in contact with the accelerating planar surface. If the horizontal seismic shaking is large enough, the friction force will not be able to force the particle to move with the planar surface. The particle will move independently of the horizontal motion of the plane if $\ddot{x}_{rel} \neq 0$. Assuming $a_t > 0$, this condition becomes:

$$m_d a_t > \mu \left(m_d a_n - F_{es} - F_{grav} - F_{co} \right) \tag{3.9}$$

Note that $\zeta = 1$ because the friction force is at its max strength. The separation condition for transverse seismic shaking is similar to that of normal seismic shaking. Thus, for simplicity, only vertical seismic accelerations will be discussed.

The three forces acting on the particle will now be discussed in detail.

3.1.1 Gravitational Force

The simplest of the three forces acting on the particle, the gravitational force can be described by:

$$F_{grav} = -\frac{4}{3} \pi r_d^3 \rho \left(g_s - \omega^2 r_c \right) \tag{3.10}$$

Dust particles are assumed to be spherical with radius r_d and density ρ. The gravitation at the surface of the body is given by g_s. The gravitation of the body can be altered to account for the rotation of the body (ω is the rotation rate and r_c is the radius of the spherical central body). This chapter will consider only a non-rotating frame ($\omega = 0$).

3.1.2 Cohesion Force

Past work has investigated, theoretically and experimentally, the characteristics of the van der Waals force in granular materials [29, 26, 8]. The cohesion between two spherical particles (sizes r_1 and r_2) can be approximately described by [8, 39, 48]:

$$F_{co} = \frac{-D}{48\left(t+d\right)^2}\frac{r_1 r_2}{r_1 + r_2} \tag{3.11}$$

where D is the Hamaker constant for the powder (4.3×10^{-20} Joules for lunar soil [39]), t is the minimum distance between the particle surfaces due to adsorbed molecules and d is width of any additional separation between the particles beyond that caused by the presence of the adsorbed molecules.

Since we assume that the cohesion force is only active when particles are in contact, d is neglected. Assuming that the desired cohesion occurs between the particle and a flat plate, $\frac{r_1 r_2}{r_1+r_2}$ approaches r_d [8]. Additionally, we substitute $S = B/t$ into Eq. (3.11), where B is the diameter of an O^{-2} ion ($B = 1.32 \times 10^{-10}$ m) [39]. S is the approximate cleanliness of the granular powder and can be thought of as the inverse of the number of layers of adsorbed molecules separating the plate and the dust grain. A perfectly clean surface has cleanliness (S) equal to one. A powder in Earth's atmospheric environment has a cleanliness of approximately 0.13 [39]. Perko *et al.* [39] estimate the cleanliness on the lunar surface to be 0.88 during the day and 0.75 at night [39]. The powder cleanliness is thought to be higher during the day due to the increased surface temperature, resulting in fewer adsorbed molecules. Thus, Eq. (3.11) reduces to:

$$F_{co} = -CS^2 r_d \tag{3.12}$$

(in Newtons, where the radius of the particle is in meters) where $C = 5.14 \times 10^{-2}$ kg/s^2. Additional discussion of the importance of cohesion on asteroids can be found in [49]. Additionally, since there is uncertainty in the magnitude of the cohesive force due to variations in the angularity and orientation of dust particles and the Hamaker constant of asteroid regolith, in the subsequent analysis we allow two orders of magnitude variation in the cohesive force by varying the cleanliness ($S = 0.1 - 1$). This approach to dealing with uncertainty in the cohesive force magnitude was suggested in [49].

3.1.3 Electrostatic Force

The general form of the electrostatic force felt by a particle is given by:

$$F_{es,gen} = QE \tag{3.13}$$

where Q is the charge on the particle and E is the electric field strength felt by the particle. The charge and electric field strength felt by a single particle are subject to significant uncertainty due to the complex charging environment on the particle-scale. For example, charge separation can occur on a single dust particle due to the dielectric nature of the material. Additionally, highly localized shadowing between grains can cause elevated electric fields. However, we can relate the average charge distribution to the electric field strength over some area (A) through Gauss' law:

$$Q = EA\epsilon_0 \tag{3.14}$$

where ϵ_0 is the permittivity of free space. By substituting the surface area of the grain into Eq. (3.14), we can express the average charge on a particle of a given size as a function of the local electric field strength. The charge on the particle may fluctuate above or below the value given in Eq. (3.14) since charging is a discrete event and regolith is dielectric. The discretization of charging can have a significant effect on the force felt by a particle if the level of charging is small. In this chapter, we assume that the discretization effect is negligible because the charge on each dust particle is much greater than one electron, an assumption that will be validated in Section 3.3.1.2.

Substituting Eq. (3.14) into Eq. (3.13), we get an expression for the electrostatic force on a particle of radius r_d:

$$F_{es} = 4E^2 \pi r_d^2 \epsilon_0 \tag{3.15}$$

Once a particle is separated from the surface, the electrostatic force is given by Eq. (3.13), where the particle charge Q is a time varying state variable and E varies with altitude. Hughes *et al.* [28] and Nitter *et al.* [38] present detailed discussions of the 1D equations of motion once a particle has separated from a seismically quiet surface ($A_n = 0$) and particle levitation will be discussed in Chapter 5 and Chapter 6. This chapter is only concerned with the case of the particle in contact with the surface and the initial time step after launching.

3.2 Particle Launching and Separation

For the purposes of this work, a dust particle will be said to be launched if its initial inertial acceleration is in the positive direction (up) and has a magnitude greater than the positive acceleration rate of the surface (considering vertical seismic acceleration). For instance, a particle with a negative inertial acceleration ($\ddot{y}_i < 0$) will not be considered to be launched although it may no longer be in contact with the planar surface ($\ddot{y}_{rel} > 0$). A particle is said to be separated from the surface if the normal force acting on the particle is zero ($\ddot{y}_{rel} \geq 0$).

3.2.1 Particle Separation

In order for a dust particle to become separated from the surface, the following relationship (from Eq. (3.4) assuming $\ddot{y}_{rel} \geq 0$) must hold:

$$m_d a_n \leq F_{es} + F_{grav} + F_{co} \tag{3.16}$$

where a_n is positive when the surface is accelerating in the $+\hat{y}$ direction and negative when the surface is accelerating in the $-\hat{y}$ direction. Given some level of vertical acceleration, we can solve for the electrostatic force that is required to separate a particle from the surface:

$$F_{es} \geq m_d a_n - F_{grav} - F_{co} \tag{3.17}$$

Expanding Eq. (3.17) given the definitions of the forces given in Section 3.1 gives:

$$4E_{req}^2 \pi r_d^2 \epsilon_0 \geq \frac{4}{3}\pi r_d^3 \rho \left(g_s + a_n\right) + CS^2 r_d \tag{3.18}$$

This force balance equation assumes that the electric field is normal to the surface. We then solve for the electric field strength required to separate a particle from the vertically accelerating plane:

$$E_{req} \geq \left[\frac{1}{3\epsilon_0} r_d \rho \left(g_s + a_n\right) + \frac{CS^2}{4\pi\epsilon_0 r_d}\right]^{1/2} \tag{3.19}$$

Recall that the acceleration of the surface may be positive or negative since the seismic acceleration is assumed to be sinusoidal. If the surface is accelerating upwards ($a_n > 0$), the seismic shaking will cause an increase in the electric field strength required to separate the particle from the surface, as expected. Since we would like to minimize the electric field strength required to separate a particle from the surface, we will consider only negative surface accelerations throughout the following development ($a_n < 0$).

E_{req} closely resembles a hyperbolic function of r_d. At small particle radii, the electric field strength required to separate a particle is dominated by the cohesive force, while at large particle radii, it is dominated by the gravitational force. Given Eq. (3.19) and assuming that launching will occur during a downwards seismic acceleration ($a_n \leq 0$), we can solve for the particle radius at which the minimum electric field strength will be required to separate a particle from the surface.

$$r_{d,minES} = \sqrt{\frac{3CS^2}{4\pi\rho\left(g_s + a_n\right)}} \tag{3.20}$$

The corresponding minimum electric field strength required to separate that particle is:

$$E_{min} = \sqrt{\frac{1}{\epsilon_0}}\left[\frac{CS^2\rho\left(g_s + a_n\right)}{12\pi}\right]^{1/4} \tag{3.21}$$

Particles of this size ($r_{d,minES}$) will, in essence, be the easiest to separate from the surface. Note that the minimum electric field strength is proportional to $g_s^{1/4}$. Thus, in order to see an order of magnitude decrease in the minimum electric field strength required to separate a particle from the surface, the surface gravity of the body must be decreased by a factor of 10,000.

Once a particle becomes separated from the surface, the inertial equation of motion becomes:

$$m_d \ddot{y}_i = F_{es} + F_g \tag{3.22}$$

because the cohesive bond between the particle and the surface is only active when the particle is in contact with the surface. While $\ddot{y}_{rel}$ is defined with respect to the accelerating surface, $\ddot{y}_i$ is defined with respect to an inertially fixed altitude. At the initial time, the electric field strength will be given by Eq. (3.19). Since the electrostatic force must overcome both gravity and cohesion in order for the particle to separate from the surface, once the cohesive force disappears (due to the separation of the particle from the surface) there exists some extra force on the particle (due to the electric field strength required to break the cohesive bond), which causes an initial acceleration. Substituting Eq. (3.19) into Eq. (3.22) and assuming that lofting occurs during a negative amplitude seismic acceleration ($a_n \leq 0$), we can determine the inertial acceleration that the particle experiences at the initial timestep:

$$\ddot{y}_i = \frac{3CS^2}{4\pi r_d^2 \rho} + a_n \tag{3.23}$$

Note that Eq. (3.23) is independent of the local surface gravity. The local surface gravity term in Eq. (3.19) is canceled by the gravity term in Eq. (3.22). Essentially, Eq. (3.23) is an expression for the excess electrostatic force on the particle since the cohesive force has disappeared. The downwards seismic acceleration will reduce the initial inertial acceleration compared to the $a_n = 0$ case because the downwards acceleration of the surface essentially makes it easier for the particle to separate from the surface. Note that the initial inertial acceleration given in Eq. (3.23) is not strictly positive. Additionally, the initial acceleration of the particle could be slightly larger than that given in Eq. (3.23) due to the discretized nature of particle charging.

In Eq. (3.23), we saw that downwards accelerations of the surface reduce the initial inertial acceleration of a dust particle. In fact, for a given level of negative seismic acceleration, there exists a particle radius where no electrostatic force is needed to separate a particle from the surface. By setting $E_{req} = 0$ in Eq. (3.19), we can derive an expression for the minimum particle size where no

electrostatic force is required to separate a particle from the surface (assuming $a_n < 0$):

$$r_{d,E=0} = \sqrt{\frac{3CS^2}{4\pi\rho\left(-a_n - g_s\right)}} \tag{3.24}$$

All particles larger than $r_{d,E=0}$ will become separated from the surface without any electrostatic force, although it is not guaranteed that they will have positive inertial accelerations.

3.2.2 Particle Launching

The initial inertial acceleration given by Eq. (3.23) is not strictly positive. For a negatively accelerating surface, particles may be accelerating downwards less quickly than the surface ($\ddot{y}_{rel} > 0$, $\ddot{y}_i < 0$). By setting the inertial acceleration (Eq. (3.23)) to zero, we can derive an equation for the maximum particle size that will have a positive acceleration due to the electric field strength given in Eq. (3.19) for a negatively accelerating surface ($a_n < 0$):

$$r_{d,a=0} = \sqrt{\frac{3CS^2}{-4\pi a_n \rho}} \tag{3.25}$$

All particles larger than $r_{d,a=0}$ will require a stronger electric field than E_{req} (Eq. (3.19)) to be positively accelerated. Positively accelerating particles are of interest because they are likely to have a longer flight time before reimpact and, thus, larger translational motion. Also, Eq. (3.25) is independent of the local surface gravity, since Eq. (3.23) is independent of the local surface gravity. We note that for a surface experiencing an instantaneously positive acceleration at the time of separation, the particle may experience a positive initial velocity and negative initial acceleration. This scenario will not be considered here as we seek to minimize the electric field strength required to launch a particle, thus necessitating negative or zero seismic accelerations ($a_n \leq 0$).

In order for the initial inertial acceleration to be positive for particles larger than $r_{d,a=0}$,

$$m_d \ddot{y}_i = F_{es} + F_g \geq 0 \tag{3.26}$$

must hold. Again assuming uniform charge distribution, we can solve for the electric field strength required for these particles to have a positive initial acceleration:

$$E_{pos} \geq \left[\frac{\rho r_d g_s}{3\epsilon_0}\right]^{1/2} \tag{3.27}$$

For particles larger than $r_{d,a=0}$, the electric field strength required to give the particles a positive inertial initial acceleration is given by Eq. (3.27), which is stronger than E_{req}, given by Eq. (3.19). If $r_{d,a=0} < r_{d,minES}$, then the minimum in the electric field strength required to launch a particle as a function of particle radius occurs at the intersection of E_{req} and E_{pos} rather than at $r_{d,minES}$. It can be seen that if $-a_n/g_s > 1/2$ (assuming $a_n < 0$), $r_{d,a=0} < r_{d,minES}$. For smaller ratios of seismic to gravitational acceleration, the minimum in the electric field strength required to launch a particle as a function of particle radius occurs at $r_{d,minES}$.

3.2.3 Particle Initial Conditions

Once a particle has been launched from the surface, its initial acceleration can be calculated from Eq. (3.22), substituting the appropriate electric field strength. If $A_n = 0$, $a_n > 0$, or $a_n < 0$ and $r_d < r_{d,a=0}$, the electric field strength will be described by Eq. (3.19). If $a_n < 0$ and $r_d \geq r_{d,a=0}$, the electric field strength will be described by Eq. (3.27). The initial particle acceleration can be used in numerical particle dynamics models if it is assumed that sufficient electric fields for particle launching occur, which is not a foregone conclusion considering the large magnitudes of the electric fields required. Additionally, instead of modeling an initial particle acceleration in numerical models, it is possible to translate the initial acceleration to an initial energy and subsequently to an initial particle charge given the surface potential.

Initial particle velocities with zero initial particle charges have been used in previous numerical particle transport models [13, 28]. If the body is assumed to be seismically quiet ($A_n = 0$), the initial particle velocity will be zero with a nonzero initial particle charge that contains the initial energy. If the body is seismically active, the particle dynamics are more complicated. The initial particle velocity will be the velocity of the surface at the time of separation. However, the initial velocity is then likely to be negative, since it will be easiest to launch a particle on the downstroke of the seismic acceleration cycle. Regardless of the initial acceleration direction of the downwards traveling particle, the particle may reimpact with the seismically active surface. If the surface cleanliness of the particle decreases after lofting and before reimpact, then the interaction with

surface could provide an energy impulse to the particle. Alternatively, upon reimpact, the particle could become embedded in the surface and potentially cause the release of other particles. The dynamics of particles launched from a seismically active surface have not yet been completely described and require further investigation.

3.3 Results

3.3.1 Effects of Cohesion Neglecting Seismic Shaking

Given Eq. (3.19) and assuming no seismic acceleration ($A_n = 0$), we can plot the required electric field strength for particles of different sizes to be launched (Figure 3.2), given varying surface gravitation (see Table 3.1) and varying surface cleanliness (S). Essentially, Figure 3.2 provides the necessary electric field strength as a function of particle size in order for electrostatic dust lofting to occur, if the charge on a dust particle can be approximated by Gauss' law. From Figure 3.2, we can see that the minimum in the curve of electric field strength required does not occur at the smallest particle radius size, which is expected since the cohesion term in Eq. (3.19) is inversely proportional to the particle radius. Thus, at small particle sizes, the cohesive forces dictate the electric field strength required to loft a particle. For larger particles, the cohesive force ($F_{co} \propto r_d$) becomes insignificant compared to the gravitational force ($F_{grav} \propto r_d^3$). Additionally, the minima in the curves for the Moon's gravity occur at particle radii of 100-1000 microns. As the surface gravity decreases, the minima in the curves shift to the right, indicating that it becomes increasingly easy to electrostatically loft larger particles.

Table 3.1: Surface gravity used in creating Figure 3.2.

Moon	1.622 m/s^2
Eros	0.0055 m/s^2
Itokawa	8.603×10^{-5} m/s^2

The second significant result from Figure 3.2 is the magnitudes of the electric field strengths required to electrostatically loft particles. For 100 micron particles on the Moon with a surface

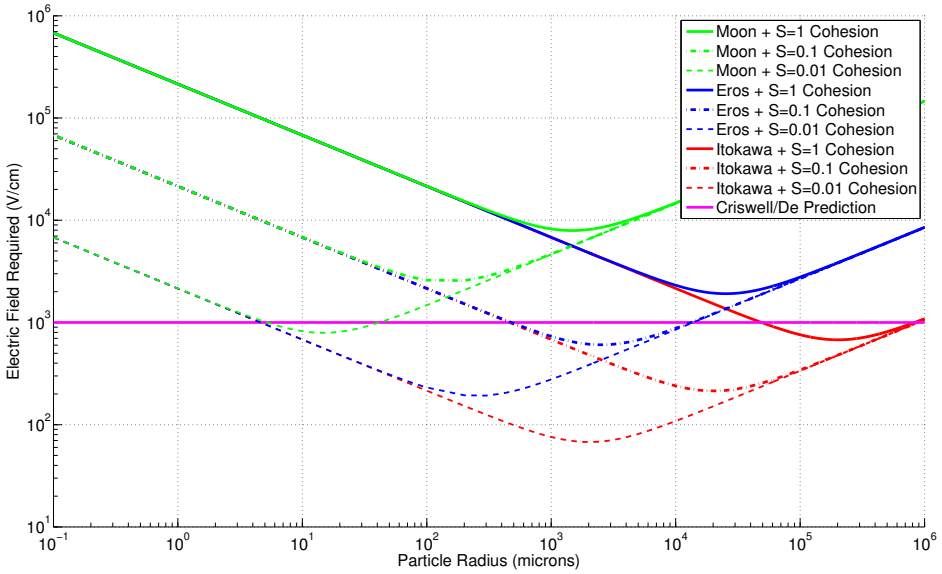

Figure 3.2: Electric field strength required to electrostatically loft spherical particles with a density of 3.5 g/cm^3. A seismically quiet surface is assumed. Perko [39] estimates the cleanliness of pristine lunar dust to be 0.75-0.88.

cleanliness of 0.1 (which is relatively unclean as compared to predictions of Perko *et al.* [39] of S=0.75-0.88), the required electric field strength is $\sim 3,000$ V/cm. Considering that the largest nominal electric field strength on the lunar surface is approximately 0.08896 V/cm (following Hughes' development [28], calculated at the subsolar point), the electric field strength required to loft a particle when cohesion is included in the force balance equation is extremely large. Often the terminator region (essentially dusk and dawn) is cited as a probable region of electrostatic lofting because of the increased electric field strengths hypothesized to exist in this region due to the close proximity of lit and shadowed grains. De and Criswell present a numerical study of the possible electric field strengths in the sunset terminator by assuming that no charge neutralization occurs in this region and that electric fields may act over very short distances [15]. The assumption that no neutralization occurs in the terminator region is now known to be false, since the thermalization of solar wind plasma electrons will result in some neutralization in the lunar sunset terminator despite the solar wind velocity aberration in this region. Additionally, the electric field

strengths hypothesized by De and Criswell [15] act only locally. Thus, De and Criswell's [15] estimated electric field strength of 1000 V/cm is an optimistic upper bound on the maximum electric field strength possible on the lunar surface. However, even considering this optimistic estimation of the maximum electric field strength on the lunar surface, we see that there is a gap between the minimum electric field strength required to electrostatically loft particles and the maximum electric field strength possible on the lunar surface, when particle charging is assumed to be given by Gauss' law.

Often results concerning electrostatics and dust particles on the Moon are extended to asteroids with the argument that dust movement will be easier in the reduced gravity environments of these bodies. From Figure 3.2, we can see that results cannot be so easily ported between bodies. Although the minimum electric field strength required for electrostatic lofting does decrease on asteroids, the particle radius where this minimum occurs increases. Thus, if sufficiently strong electric fields exist, increasingly large particles may be mobile on asteroids. From Eq. (3.21), we see that the minimum electric field strength required to loft a particle is proportional to $g_s^{1/4}$. Thus, an order of magnitude drop in the electric field strength required to loft a particle requires a four order of magnitude decrease in the surface gravitation. Additionally, for dust particle radii that are in the cohesion-dominated region of the E_{req} curve (Figure 3.2, $r_d < 10^3$ microns), we note that there is no difference in the electric field strength required to launch particles on the asteroids as compared to the Moon. Thus, it is not significantly easier to launch small particles off of asteroids than the Moon. Even if the optimistic De and Criswell estimation of the maximum electric field strength is applied to asteroids, only very large particles ($> 10^3$ microns) are able to be launched at very low surface cleanlinesses ($S = 0.1$).

3.3.1.1 Possible Variations in the Cohesive Force Magnitude

By varying the cleanliness from $S = 0.01$ to $S = 1$, the magnitude of the cohesive force in Figure 3.2 is varied over four orders of magnitude since $F_{co} \propto S^2$. Thus, by including large variations in cleanliness, we allow for variations in the magnitude of the cohesive force due to

variations in the Hamaker constant, particle cleanliness and surface asperities of the dust particles. Additional discussion of the inclusion of surface asperities by varying S can be found in [49], where it is stated that "a grain with surface asperities one tenth of the particle's radius will have a cleanliness of 0.3." If dust particles are assumed to be spherical, Perko *et al.* [39] predict that the cleanliness (S) should range form 0.75 to 0.88 due to the expected levels of adsorbed molecules in the lunar regolith. Variations in gravitation due to surface topography are incorporated by plotting the results for multiple central bodies of different mass.

3.3.1.2 Charge Quantization Effects

Note that this development assumes that the charge on the dust particle is $Q = 4E_{req}\pi r_d^2\epsilon_0$, which does not take into account the discrete nature of charging: a dust particle cannot have a fraction of an electron of charge. For the case of a dust particle with a small charge (for instance, less than 10 electrons), quantization effects (where a particle is modeled to have a charge of $+6.5e$ instead of $6e$ or $7e$) would clearly significantly influence the electrostatic force felt by the particle. At the lunar subsolar point, the surface electric field strength is approximately 8.896 N/C, following the calculations by Hughes *et al.* [28]. This corresponds to a charge of 9.89×10^{-20} C on a 10 micron radius grain, which is less than the charge of one electron. Essentially, two in every three dust particles will have a charge of $+1e$ (where e is the charge of an electron), assuming that all dust particles are 10 microns in radius. However, the electric fields shown in Figure 3.2 for the particle sizes considered correspond to charges of more than 22 electrons (and for most cases, several hundred electrons), at which point quantization effects do not significantly alter the electrostatic force felt by a dust particle.

3.3.1.3 Non-Gaussian Charging Effects

The results shown in Figure 3.2 assume that the charge on a given dust particle is given by Gauss' law. Applying Gauss' law assumes that the dust grain has the same charge as is contained by a sphere in the plasma at a given electric field strength. However, it is very unlikely that the dust

particle will be surrounded by a uniform electric field. However, charging is a discrete phenomena and regolith is dielectric, both of which could result in variations of the charge of particles away from the average value given by Gauss' law. On average, the charge on the particle will agree with the prediction from Gauss' law. Increasing the charge on the dust particle will reduce the electric field strength required to loft the particle. Experimental work indicates that non-Gaussian charging could be significant in dust lofting. A discussion of the effects of non-Gaussian charging is included in Section 3.4.

3.3.2 Effects of Seismic Shaking

From our analysis of the electric field strength required to launch particles without considering seismic shaking, we have seen that the particle radius at which the minimum electric field strength is required for lofting occurs is several orders of magnitude larger than the particle radii that are expected to produce the observed lunar horizon glow. Additionally, the minimum electric field strength required to loft particles off the Moon is an order of magnitude larger than the most optimistic estimate of the terminator electric field strength, when particle charging is assumed to be given by Gauss' law. We now consider the effect of seismic shaking on the electric field strength required to launch particles.

Figure 3.3 shows the electric field strength required to launch (or separate) a particle of a given radius off the lunar surface at various magnitudes of negative surface acceleration for $S = 1$. Neglecting cohesion, any accelerations above 1 G_L (where G_L is the gravitational acceleration at the lunar surface) will separate particles from the surface. However, this is not true for all particle sizes when cohesion is included. The accelerations shown in Figure 3.3 were chosen in order to explore the region where seismic shaking reduces (but does not eliminate) the electrostatic force required to loft particles. Note that at small particle sizes, the electric field required to launch a particle for any level of seismic activity approaches the $A_n = 0$ curve, since E_{req} is dominated by the cohesive force in this region. As the particle size increases, we begin to see variation between the electric fields required to launch particles at different levels of seismic activity. As expected, at stronger seismic

accelerations, particles can be separated at weaker electric field strengths. However, as the particle size continues to increase (transition from solid to dashed lines in Figure 3.3), the electric field strength required for separation of the particle (E_{req}) becomes less than the electric field strength required for positive inertial acceleration (E_{pos}). All particles in a plasma environment with an electric field strength greater than E_{req} (dashed line) will be separated from the surface and have a non-zero initial velocity with respect to the accelerating surface. The electric field strength required to launch particles larger than $r_{d,a=0}$ (i.e. the particle must separate from the surface and have a positive initial inertial acceleration) is given by E_{pos} in Eq. (3.27) (solid lines in Figure 3.3) and dictated by the local gravitation. Although particles launched at electric field strengths greater than E_{pos} (solid line) will have a positive initial inertial acceleration, they may have a downwards initial velocity, depending on the velocity of the surface when the particle is released. As the particle size continues to increase, it can be seen that the electric field required to launch particles experiencing seismic acceleration is approximated by the $A_n = 0$ curve. Thus, we can see that vertical seismic accelerations only change the electric field strength required to launch particles slightly and are only significant over a very small range of particle sizes. Consequently, seismic shaking does not significantly reduce the electric field strength required to launch dust particles. Thus, seismic accelerations do not bridge the gap between the electric field strength required to launch particles and that provided by our understanding of the terminator environment.

For $S = 0.1$, the curves in Figure 3.3 are shifted down and left. As expected, reducing the cleanliness of the powder shifts the electric field curve minimum to a smaller particle radius. Additionally, lowering the cleanliness results in a decrease in $r_{d,a=0}$. Varying the cleanliness of the dust has a larger effect on the electric field strength required to launch particles than seismic activity.

Figure 3.4 shows the electric field strength required to launch particles off of the surface of asteroids as compared to that of the Moon, assuming that all bodies are undergoing vertical seismic accelerations of $a_n = 0.5G_L$, where G_L is the gravitational acceleration of the Moon. Following the work of Richardson *et al.* [45] and the modeling of asteroid disruption completed by Benz

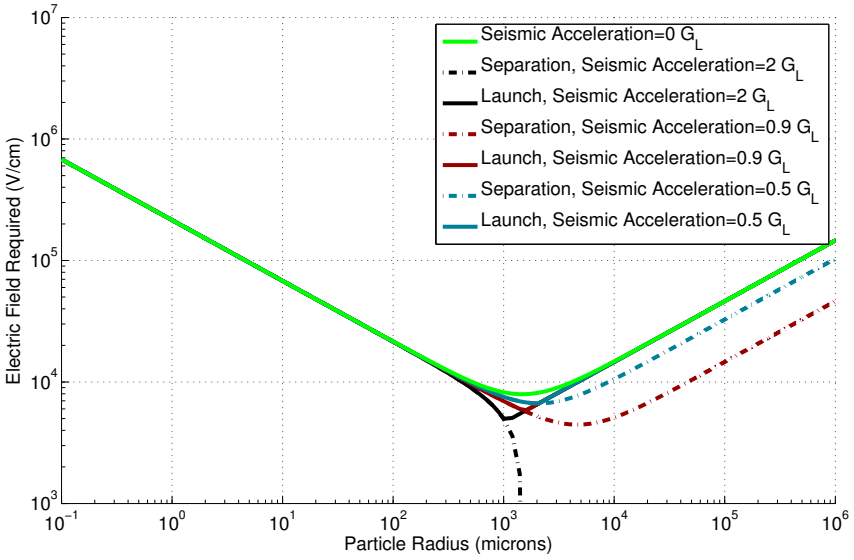

Figure 3.3: Electric field strength required to launch (or separate) spherical particles with a density of 3.5 g/cm^3 and $S = 1$ off the lunar surface with varying levels of seismic accelerations (G_L is lunar gravity, 1.622 m/s^2). Downwards seismic accelerations are assumed. Note that dashed lines show the electric field required to separate a particle from the accelerating surface and solid lines show the electric field strength required to give the particle an initial positive inertial acceleration. Particles in electric fields stronger than the dashed lines will be mobile, however, their initial inertial acceleration may not be positive.

and Asphaug [1], we can see that surface accelerations of $0.5G_L$ would not result in the disruption of Eros or Itokawa and thus are reasonable to consider. Note that for particle sizes smaller than 10^3 microns, cohesion dominates the electric field strength required and there is little difference between the electric field strength required for launching on the three bodies considered. For larger particles on Itokawa, we see that some may be launched at the electric field strengths proposed by De and Criswell.

3.4 Experimental Agreement

There have been a series of experiments looking at the motion of dust particles initially resting on a surface and subjected to a plasma sheath. Experimental evidence for the preferential movement of intermeidately-sized grains will be discussed in Chapter 4.

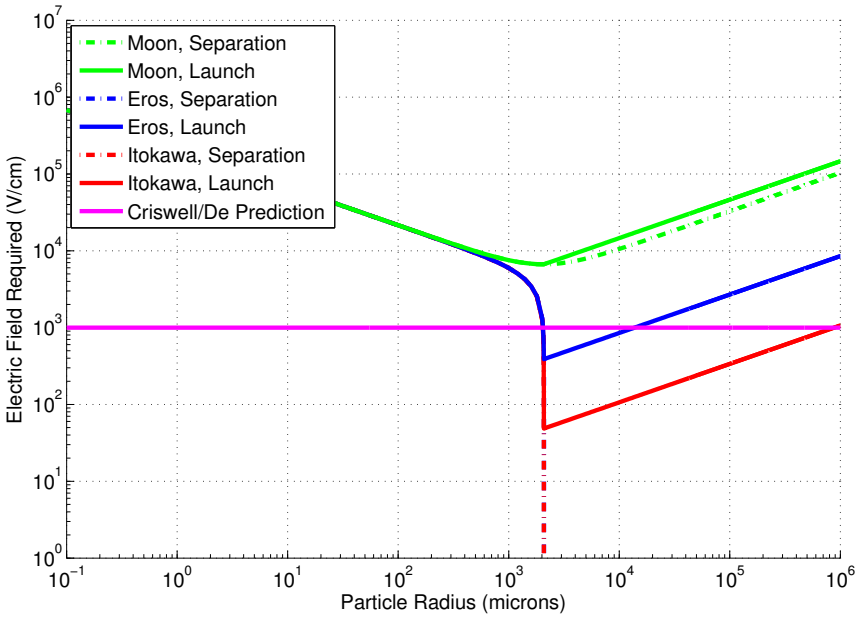

Figure 3.4: Electric field strength required to launch (or separate) spherical particles with a density of 3.5 g/cm^3 and $S = 1$ off lunar and asteroid surfaces with seismic accelerations of $0.5G_L$ (G_L is lunar gravity, 1.622 m/s^2). Downwards seismic accelerations are assumed. Note that dashed lines show the electric field required to separate a particle from the accelerating surface, although the particles will maintain a downwards acceleration.

There are two main experimental setups that have been used to study the movement of dust particles in a plasma. First, we discuss the observations of Sickafoose *et al.* [52], Colwell *et al.* [12] and Wang *et al.* [59]. Their experimental setup includes a negatively biased plate immersed in an argon plasma. When the plate is biased to below -30 V, particles are seen to loft off the plate without direct mechanical agitation ([52, 12]). Wang *et al.* [59] observes the spreading of a pile of dust when it is exposed to the plasma and attempts to measure the charge on test particles, although the measurement technique is complicated by the possibility of triboelectric charging. There is limited discussion of the sizes of the particles that are launched in all experiments. It is difficult to assess the cohesion of the powders used in these experiments since the powder samples were not baked prior to experimentation.

The second experimental setup (used by Goree and colleagues [50, 17]) consists of an insulating sphere covered in dust and rotating in a plasma. In these experiments, the investigators

find that the dust particles must be exposed to both a plasma and an electron beam in order to be released from the surface, in contrast to the experiments by Sickafoose *et al.*, Colwell *et al.* and Wang *et al.* that do not require the presence of an electron beam. Additionally, they see that the rate of dust release varies with the plasma density. No particles larger than 20 microns were included in these experiments. In these experiments, there is no effort to ensure high particle cleanliness by reducing the number of absorbed molecules in the dust sample.

By conducting simple force balances using the measured (in the case of Wang *et al.* [59]) and calculated electric field strengths (Goree and colleagues [50, 17]), it can be seen that it would be impossible for dust particles to separate from their surfaces, even neglecting cohesion, if their charge is given by Gauss' law. Note that this simple force balance analysis has only been discussed by [17]. Thus, since these dust particles are seen to move experimentally, the charge on the dust particles must be greater than that predicted by Gauss' law. Gauss' law will give the average charging on the dust particles. However, the charge on the dust particles will be time varying as the emission of photoelectrons and collisions with electrons from the plasma are discrete events. Thus, there will be a nonuniform distribution of charges on the dust particle scale, while adhering to Gauss' law on the larger scale. For all three experiments considered ([59, 50, 17]), the average charge on the dust particle is given by:

$$Q_{avg} = 4E_0\pi r_d^2\epsilon_0 \tag{3.28}$$

where E_0 is the electric field at the surface that is measured in the experiments. The Wang *et al.* [59] experiment considers the movement of a dust particle off of a flat plate. Thus, the charge that the dust particle requires to break the cohesive bond and overcome gravity is given by:

$$Q_{req} = \frac{1}{E_0}\left[m_d g_E + CS^2 r_d\right] \tag{3.29}$$

where $g_E = 9.81$ m/s^2, since the experiment was performed under terrestrial gravitation conditions.

In the Goree and colleagues [50, 17] experiments, the dust particles are attracted to a rotating sphere. Thus, we must take into account both the rotation of the sphere and the detachment of

the dust from the top of the sphere (due to the presence of an electron beam) when writing the expression for the charge required for the particle to detach from the surface:

$$Q_{req} = \frac{1}{E_0}\left[CS^2 r_d + m_d g_E - m_d r_c \omega^2\right] \tag{3.30}$$

where r_c is the radius of the rotating sphere and ω is the rotation rate of the sphere, both of which are given in [50, 17].

Given expressions for the charge required to separate dust particles from the surfaces in these experiments (Q_{req}) and the average charge likely to be on the dust particles (Q_{avg}), it is possible to characterize the degree of nonuniformity needed in charging in order for dust particles to be lofted. We characterize the required degree of nonuniformity by calculating the charge amplification ratio for the experiments. We define the charge amplification ratio by:

$$C_{amp} = \frac{Q_{req}}{Q_{avg}} \tag{3.31}$$

Due to uncertainties in the cleanliness of the dust used in the experiments and the dust particle sizes that were seen to move, the charge amplification ratio ranges from 1.01×10^4 to 2.60×10^8 in the experiments considered. If the electric field strengths reported in [59, 50, 17] are correct, then this large degree of nonuniformity in charging must exist since dust particles are seen to move. As none of the experiments to date seek to exactly reproduce the lunar environment, it is not known if this level of charge nonuniformity would occur on the Moon or asteroids. However, we will investigate the impact of this high level charge nonuniformity on the electric fields required to separate a dust particle from the surface of the Moon or asteroids. Modifying Eq. (3.19) to include the charge amplification ratio gives:

$$E_{req} \geq \left[\frac{r_d \rho \left(g_s + a_n\right)}{3\epsilon_0 C_{amp}} + \frac{CS^2}{4\pi\epsilon_0 r_d C_{amp}}\right]^{1/2} \tag{3.32}$$

Assuming an intermediate value of the charge amplification ratios calculated from the experimental data, the electric field strength required to loft dust particles (given by Eq. (3.32)) is shown in Figure 3.5, assuming $A_n = 0$. There are several notable features of Figure 3.5. Firstly, it can

be seen that assuming a large level of charge inhomogeneity shifts the curves in Figure 3.2 down, so that the electric field strength required is below that predicted by De and Criswell to occur in the terminator regions for all the particle sizes considered. However, we note that the cohesive force continues to dominate the electric field strength required to loft the smallest particles. Additionally, we note that the minima in the curves for all of the bodies considered occurs above 10^{-1} V/cm, which is likely to be the highest electric field strength on the surface outside the terminator region (to occur at the subsolar point). Thus, even considering the very large charge amplification ratios that are predicted by experimental results, it is difficult to loft dust particles outside of the terminator region. Additionally, the minima in the curves are unchanged by the inclusion of the charge amplification ratio, indicating that, even assuming nonuniform charging, larger particles will be easier to loft off the surface of the Moon than submicron particles.

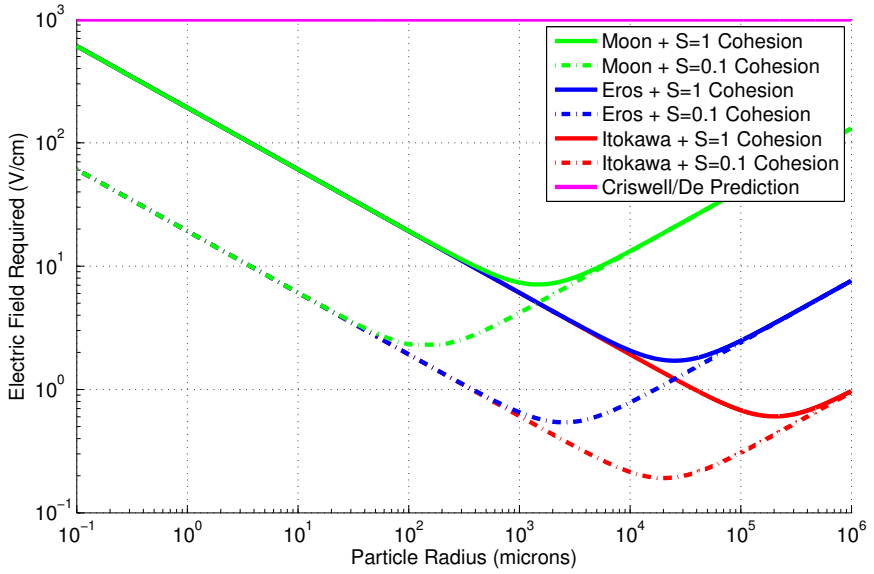

Figure 3.5: Electric field strength required to electrostatically loft spherical particles with a density of 3.5 g/cm^3 assuming a charge amplification ratio (C_{amp}) of 1.25×10^6, which is within the range that has been seen in experimentation. The bodies are assumed to be seismically quiet. The Criswell and De prediction is an optimistic estimate of the electric field strength that could occur at the terminator regions of these bodies.

3.5 Discussion

We have shown that cohesive forces are significant when considering the particle sizes that could be launched off the surface of the Moon and asteroids. The particles that will be launched from the Moon at the lowest electric field strength will be 100-1000 microns in radius. A discussion of the experimental support for the preferential motion of intermediately-sized particles will be discussed in Chapter 4.

Although we have shown that intermediately-sized dust particles (potentially significantly larger than the submicron to micron-sized grains that have previous been considered) require the smallest electric field to loft, it is important to note that these dust particles will receive the smallest impulse due to the removal of the cohesive force when the particle is lofted. Thus, intermediately-sized grains may be lofted much more frequently than both smaller and larger grains, but the vertical extent of their motion will be limited. Thus, spacecraft may be more likely to observe small grains due to their higher peak altitudes.

We have also shown that the electric field strength required in order for particles to be launched is an order of magnitude larger than our most optimistic estimate of the lunar electric field strength in the terminator region, if particle charging is assumed to be given by Gauss' law. Noting the shortcomings in particle launching through electrostatic forces alone, the impact of seismic shaking on the electric field strength required for lofting was explored. It can be seen that seismic acceleration only slightly reduces the electric field strength required to launch particles over a small range of particle sizes. Thus, seismic shaking does not bridge the gap between the electric field strength required for particle launching and that provided by our most optimistic estimate of the electric field strengths possible in the lunar terminator region.

Additionally, it has previously been asserted that electrostatic lofting on asteroids will be easier due to the decreased surface gravity. We note that the gravitational force acting to hold a dust particle on the surface may be decreased beyond the values used here since, due to the aspherical shapes of asteroids, the gravity vector is unlikely to be normal to the surface. The

electric field strength required to launch particles smaller than 10^3 microns is dominated by the cohesive force. Thus, we show that both with and without seismic shaking, surface gravity has very little impact on the electric field strength required to launch particles smaller than 10^3 microns off of asteroids. Reducing the local gravity does not significantly reduce the electric field strength required to launch particles in the particle size range of interest (1-1000 microns) as compared to the Moon.

Through simple force balance calculations based on the results from previous experimental work ([59, 50, 17]), it can be seen that some additional level of charging beyond that predicted by Gauss' law is required to explain the dust motion that has been observed experimentally. Applying this level of charge amplification to our theoretical calculations, we see that our predicted required electric field strength for particle motion is significantly reduced. If such a high level of charge amplification is observed *in situ*, it may be possible for a wide range of dust particle sizes to be lofted in the terminator region. However, the particle size that requires the least electric field strength to loft is not affected by the inclusion of charge amplification. Thus, even considering a high level of charge inhomogeneity, particles larger than 10 microns remain easier to loft off the surface of the Moon than submicron particles. More work should be done to understand the physical basis of the charge amplification that has been observed experimentally and to determine if these levels of charge amplification could occur *in situ*.

Previous work has attributed the observed lunar horizon glow to 5 micron (radius) airborne particles [43]. We have shown that the minimum electric field required to launch particles occurs for 0.1-1mm-sized objects on the Moon. This discrepancy between the interpretations of earlier observations and our results, derived from a more complete model of the forces on a dust particle, could potentially be resolved through several means:

- Small (<1 mm) dust particles could be launched off the surface of the Moon due to high levels of charging beyond that predicted by Gauss' law,
- Larger particles launched through electrostatic lofting could break into smaller particles

once detached from the surface,

- Particles could be launched off the surface through a mechanism other than electrostatic lofting,
- Particles could be electrostatically lofted during sporadic periods of vastly increased surface electric field strength or decreased cohesion,
- Cohesion of the dust could be reduced by the asphericity or material properties of the grains.

We will provide a brief description of these ideas, which require additional detailed investigation in order to assess their feasibility.

As mentioned previously, experimental investigations of dust motion in plasmas indicate that dust particle charge levels are considerably amplified beyond the levels predicted by Gauss' law. In this case, the electric field required for dust motion is greatly reduced (see Figure 3.5). Additionally, numerical simulations of charge fluctuations of insulating grains indicate a 1-2 order of magnitude fluctuation of the charge about the average value [51]. If small dust particles are lofted, then it is likely that larger dust particles will also be lofted since the electric field strength required for their movement will be less than that of the small dust particles. Our observations of dust motion on the Moon could thus be due to the population of lofted small dust particles.

For the case of large particles lofted off the surface of a body, it is possible that larger particle conglomerates could disrupt (break into many smaller particles) after launching to produce a population of 5 micron particles. A conglomerate of particles could disrupt once freed from the surface if it collects sufficient charge to break the cohesive bonds between its constituent grains. However, the exact charging profile of a particle or conglomerate depends on its initial conditions, thus making it difficult to predict the occurrence of such disruption without an accurate initial state (charge and velocity).

Micrometeoroid bombardment could provide an alternate means to launch particles, however this energy would only affect directly impacted grains or those in close proximity to the impact,

given our discussion of the efficacy of seismic accelerations. Previous investigations [43] indicate that micrometeoroid bombardment alone does not produce the necessary mass churning rate to produce the observed lunar horizon glow phenomena. However, this conclusion should be reexamined considering the potential for particles to be undergo sustained altitude oscillations above the surface of a body [13], thus reducing the required mass churning rate. Horányi *et al.* [27] have proposed a theory where particles are lofted by localized extreme plasma environments generated due to the impact of micrometeoroids.

Many other potential dust launching mechanisms exist and warrant additional investigation to assess feasibility. Dust particles initially launched due purely to seismic shaking (at sizes above $r_{d,E=0}$) could adsorb additional molecules when separated from the surface and thus reduce the strength of the cohesive bonds that they form when they reimpact. In this case, it is possible that the particle could experience an upwards impulse when it 'bounces' off the seismically active surface on the surface's next upward cycle.

The effect of powder cleanliness (S) on the electric field strength required for launching has also been considered. From Figure 3.2, it can be seen that reducing the cleanliness from 1 to 0.1 results in about an order of magnitude decrease in the electric field strength required for launching. Since we expect most dust lofting to occur in the cohesion-dominated region of the electric field required curve, it is clear that the most promising mechanism for reducing the electric field strength required to launch particles is to reduce the strength of the cohesive force. Perko *et al.* have previously estimated the cleanliness of lunar regolith to range from 0.75 to 0.88 [39]. The recent discovery of significant amounts of lunar water, its diurnal variation and temperature sensitivity [40, 57, 11], suggests that cohesion would be decreased even further in the terminator, specifically the cooler sunrise terminator, if the water is in small enough quantities to behave like adsorbed molecules rather than exhibiting capillary behavior, which would increase the inter-particle cohesion. Thus, particle launching will be easiest at the sunrise terminator, both because of the decreased cohesion and increased electric field strengths in this region. Data from the LEAM experiment saw the maximum reimpact flux at sunrise [2] in agreement with this hypothesis.

Additionally, Apollo 15 observed the strongest horizon glow signature during sunrise [19]. The reduced cleanliness of regolith due to absorbed water molecules is also possible on asteroids, as recent observations have demonstrated the presence of ice on the surface of asteroids [46, 6].

Although we have mainly discussed the results with cleanliness factors of $S = 0.1$ to $S = 1$, the lower cleanliness of $S = 0.01$ has been included due to uncertainties in the Hamaker constant for lunar and asteroidal regolith and experimental support for a two order of magnitude uncertainty in the cohesive force magnitude (discussed in Chapter 4). If the magnitude of the cohesion force is given in by the $S = 0.01$ curve in Figure 3.2, then the smallest particle size capable of lofting is approximately 5 microns (radius). As mentioned previously, the lunar horizon glow is thought to be caused by forward scatter of light by 5 micron dust grains. Thus, allowing for a two order of magnitude uncertainty in the Hamaker constant of lunar regolith, we are able to electrostatically loft dust particles of the same size as has been observed. Additionally, if 5 micron grains are lofted, then larger grains will also be lofted since the minimum electric field required to loft grains occurs for 15 micron radius grains for the $S = 0.01$ curve on the Moon. However, even if larger dust grains are lofted, they will reach lower peak altitudes than the smaller grains because the initial impulse when the particle separates from the surface (due to the breaking of the cohesive bond) will be greater for the smaller grains. Thus, a two order of magnitude decrease in the predicted cohesive force is required to enable the electrostatic lofting of grains in the terminator region of the Moon.

Either charge amplification or a two order of magnitude reduction in the cohesive force is required to loft 5 micron grains in the terminator region of the moon. Even applying the experimentally-observed level of charge amplification, we see that there is a dust particle size that is easiest to loft and that this size is significantly larger than the submicron-sized particles that have been suggested for dust motion in earlier work that neglected cohesion. A feasible particle launching method that considers cohesion must be articulated in order to accurately predict dust motion on airless bodies.

3.6 Conclusion

The movement of small dust particles due to electrostatic forces has been hypothesized to occur on the Moon and asteroids. However, there exists significant uncertainty in the method of launching these particles off the surfaces of these bodies. By taking an inventory of the forces affecting dust particles resting on stationary and seismically active surfaces, we have shown that the electric field strength required to launch a particle from the surface is significantly larger than the most optimistic current estimates of the electric fields thought to be present in the lunar terminator region, when particle charging is assumed to be governed by Gauss' law. By applying the same level of charge amplification that has been suggested by experimentation, we see that lofting may be possible for a range of particle sizes in the terminator region. We have also shown that the electric field strength required to launch 1-1000 micron particles from the Moon and asteroids is dominated by the cohesive forces present in the regolith. We have seen that variations in the cohesive strength more significantly influence the electric field strength required for particle launching than variations in surface gravity or seismic activity. Additionally, the strong cohesive force causes the preferential size for particle launching to be orders of magnitude larger than the 0.1-5 micron particles commonly considered, independent of the level of charge amplification assumed. The method through which dust particles are launched off the surface of an airless body is currently unknown. However, cohesion has been identified as a significant force in the launching process and should be considered in future attempts to understand particle launching methods and particle transport.

Chapter 4

Experimental Investigation of Electrostatic Dust Lofting

4.1 Introduction

Despite the range of phenomena attributed to electrostatic dust motion (from Lunar Horizon Glow to the Eros dust ponds), there has never been conclusive evidence that electrostatic lofting actually occurs *in situ*. The feasibility of electrostatic dust lofting continues to be a controversial topic [31], due to our lack of conclusive observational data and the potential implications for our understanding of the surface environment and evolution of airless bodies. As mentioned in Chapter 2, experimental investigations have demonstrated both electrostatic dust lofting and levitation. However, it is difficult to translate these experimental results to proofs of *in situ* feasibility, due to our lack of knowledge about the *in situ* plasma conditions. Previous attempts to numerically assess the feasibility of electrostatic dust lofting neglected the cohesion between grains. In Chapter 3, we showed that when cohesion is considered, there is an intermediate particle size that requires the smallest electric field strength to loft.

To date, there have been few studies of the influence of cohesion between grains on electrostatic dust motion. We will briefly review two studies that provide anecdotal evidence of the importance of cohesion in electrostatic dust lofting. The preferential lofting of larger (10+ micron) particles has been observed experimentally by the NASA Electrostatics and Surface Physics Laboratory and SETI Institute. Marshall *et al.* [34] have seen that under the influence of electrostatic forces due to incident SEM beams, aggregates (typically tens of microns in size) of small particles are seen to move off of a dusty surface, as opposed to individual submicron particles. Marshall *et*

al. have proposed that this behavior can be explained by applying Griffith's theory of fractures to powders, thus indicating that the powder is more likely to separate along voids rather than between submicron particles that are bonded through cohesive forces [34]. The motion of 20-30 micron aggregates observed by Marshall *et al.* rather than submicron particles supports our assertion that cohesive forces are important for understanding the movement of grains in a powder.

Additional support for the preferential lofting of larger particles comes from the engineering community studying how to remove accumulated dust from the surfaces of autonomous vehicles. Calle *et al.* have designed a shield that can clear itself of dust by applying an AC current to a series of filaments after a DC current has been used to polarize the dust particles [5, 4]. It has been seen that a larger voltage was required to clear the dust shields of particles under 10 microns in size due to their strong van der Waals bonds[1] .

In this chapter, an experiment supporting the preferential lofting of intermediately-sized grains discussed in Chapter 3 will be described. Piles of variously sized grains will be exposed to a plasma sheath. We see that piles of intermediately sized grains experience the most spreading, which supports the theory developed in Chapter 3.

4.2 Theory of Cohesion in Electrostatic Lofting

Prior evaluations of the feasibility of electrostatic dust lofting have assumed that dust lofting will occur if the upwards pointing electrostatic force on the dust is greater than the gravitation force holding it on the surface [32]. However, this sort of back-of-the-envelope feasibility study neglects the cohesion between dust grains, which is significant for small grains [24]. In [24] and Chapter 3, we presented the development of a theory for the electric field strength required for a given dust particle to be electrostatically lofted, which we will briefly review here. The cohesive force (in N) between a spherical dust particle and an infinite flat plate is:

$$F_{co} = -CS^2 d \tag{4.1}$$

[1] M. Hogue, 2010, Personal Communication

where $C = D/1.673 \times 10^{-18}$, D is the Hamaker constant, S is a non-dimensional index of the cleanliness of the powder and d is the diameter of the dust particle. The Hamaker constant is a property of the material (4.3×10^{-20} Joules for lunar soil [39] and $\sim 1 \times 10^{-21}$ Joules for the polystyrene microspheres used in this experiment [33]). The cleanliness index S is a measure of the thickness of the adsorbed molecules between the dust grain and the plate. Scheeres *et al.* [49] gives a more detailed discussion of the influence of cohesion on small bodies. In this experiment, the cohesion between two spherical grains is also of interest, in which case Eq. (4.1) would be modified by a factor of 0.5 (see Chapter 3 for full description of the cohesive force).

The gravitational force acting on a grain is given by:

$$F_{grav} = -\frac{1}{6}\pi d^3 \rho g_s \tag{4.2}$$

Dust particles are assumed to be spherical with diameter d and density ρ. The gravitation at the surface of the body is given by g_s.

The electrostatic force acting on the grains is simply the product of the grain's charge and the local electric field strength. We will assume that the charge on a grain resting on the surface is given by Gauss' law ($Q = EA\epsilon_0$), where Q is the charge on the grain, E is the local electric field, A is the cross-sectional area of the grain and ϵ_0 is the permittivity constant. Given this expression for the grain's charge, the electrostatic force felt by the grain is

$$F_{es} = E^2 \pi d^2 \epsilon_0 \tag{4.3}$$

Thus, electrostatic lofting will occur if:

$$F_{es} \geq -F_{grav} - F_{co} \tag{4.4}$$

Substituting in the expressions for the forces and solving for the electric field required for lofting gives:

$$E_{req} \geq \left[\frac{1}{6\epsilon_0} d\rho g_s + \frac{CS^2}{\pi \epsilon_0 d}\right]^{1/2} \tag{4.5}$$

By examining Eq. (4.5), it can be seen that for small particle sizes the cohesive term (second on the right hand side) dominates, while the gravity term (first on the right hand side) dominates

for larger particle sizes. Thus, there will be an intermediate particle size where the electric field required for lofting is minimized. The particle size of the minimum electric field strength is given by:

$$d_{minES} = \sqrt{\frac{6CS^2}{\pi\rho g_s}} \tag{4.6}$$

Thus, the smallest particles are not the most likely to be electrostatically-lofted. The goal of this work is experimentally demonstrate the validity of this theory.

4.3 Experimental Set-up

In order to test our hypothesis about the importance of cohesion in the electrostatic lofting of small dust grains, we placed small piles of uniformly sized polystyrene microspheres on a biased, conducting plate in an argon plasma. It has previously been shown that dust can be electrostaticallly lofted in this experimental set-up [59]. When the plate is biased, a plasma sheath develops and the dust grains feel an electrostatic force pointed away from the plate. At the edge of the pile, the electric field points both upwards and outwards, away from the center of the pile. Thus, if the electrostatic force is large enough to overcome gravity and cohesion, dust grains will be electrostatically lofted and redeposited away from the center of the pile. As the pile spreads, the electric field at the edge of the pile weakens. Thus, the pile will stop spreading when the electric field at the edge of the pile is less than the sum of the gravitational and cohesive forces. For a given electric field strength (supplied by the constant plasma environment) and a dust pile of uniformly sized spheres, if the pile does not spread, then the electrostatic force is not large enough to overcome the retarding forces (gravity and cohesion) that hold the dust on the surface. If a dust pile spreads, then the electrostatic force is at least initially larger than the retarding forces. The extent of spreading for piles of dust grains of various sizes indicates the electric field strength required for lofting: more spreading indicates a lower required electric field strength. Thus, in order to prove the theory from Chapter 3, we expect to observe the most spreading in piles of intermediately-sized graiins.

4.3.1 Plasma and Vacuum Chamber

A diagram of the set-up in the vacuum chamber can be seen in Figure 4.1. The vacuum chamber is spherically symmetric with a diameter of 51 cm and a height of 28 cm. Photos of the chamber in use and while open to load more dust can be seen in Figure 4.2. An argon plasma was created by an emitting filament. When heated, the filament emits electrons. Increasing the temperature of the filament increases the current from the filament. Biasing the filament causes the emitted electrons to be accelerated off the surface of the filament. The emitted electrons then collide with argon molecules, causing them to be ionized and the plasma to be produced. The highly energetic primary electrons were shielded from the graphite plate (that supported the dust piles) by a metallic plate. The graphite plate was biased, thus creating a plasma sheath above its surface. The dust piles on the graphite plate were illuminated from above with a desk lamp. The camera viewed the piles from the side, which allowed the pile spreading to be observed. The dust pile spreading was nearly impossible to observe from a top view. Additionally, a Langmuir probe and an emissive probe, both capable of vertical and rotational motion, were used. Prior to the introduction of the argon gas, the chamber pressure was $\sim 1 \times 10^{-9}$ Torr. With the argon, pressure in the chamber was 1×10^{-6} Torr. The graphite plate was biased to -60V and its floating potential was ~ -15V.

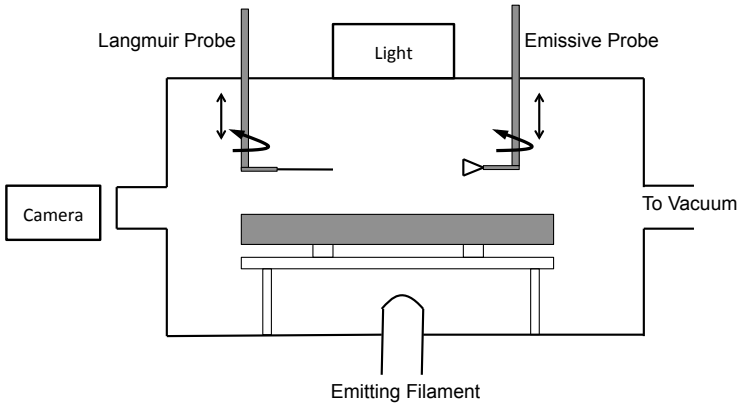

Figure 4.1: Diagram of vacuum chamber set-up. Not to scale. Note the graphite plate is shielded from the primary electrons by a small, metallic plate.

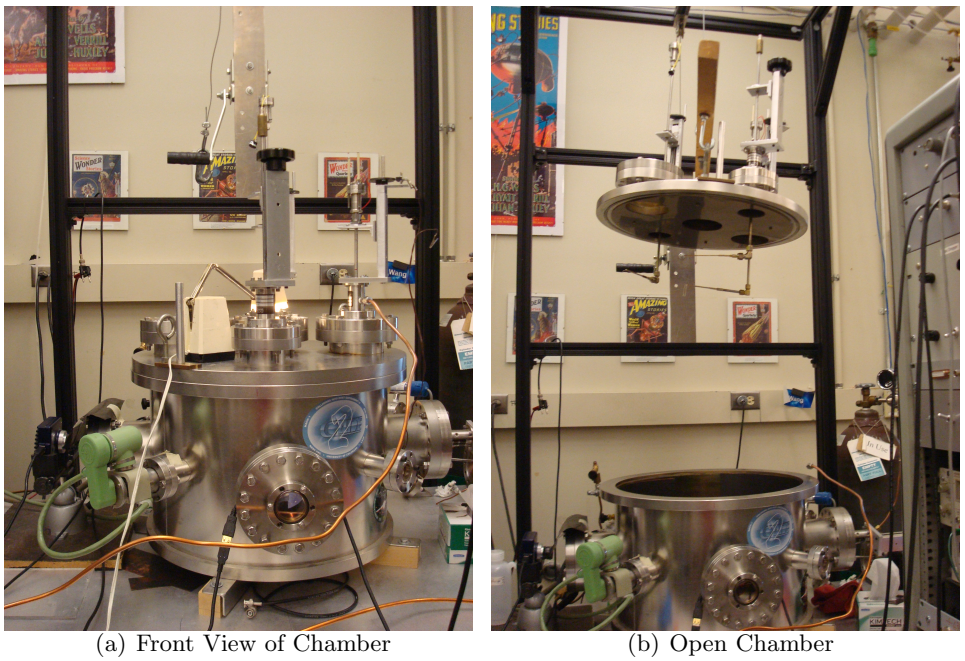

(a) Front View of Chamber (b) Open Chamber

Figure 4.2: Front views of the vacuum chamber, (a) in operation and (b) open to load more dust. Note in (b) it is possible to see the probes hanging down from the chamber lid.

4.3.2 Dust

The dust used in this experiment was highly uniform polystyrene microspheres, produced by Thermo Scientific. These dust grains are sold under the name "DRI-CAL Particle Size Standards" and are certified by NIST to be of the proper diameter. Five different size dust samples were used (see Table 4.1). Note the very small standard deviation in the grain sizes. We will refer to the dust by their nearest integer size in the text. The density of the dust used is 1.05 g/cm^3 (as given by the product information).

Highly uniform piles of polystyrene microspheres were created by filling 4 mm diameter holes drilled into 1.5 mm thick sheets of metal (referred to here as the 'pile form plates'). Extreme care was taken to ensure that no dust particles were scattered away from the central pile prior to the experiment. Dust piles were placed on the conducting plate using a pile form plate, scraping sheet, and plate guide (see Figure 4.3). Typically, the three hole pile form plate is used, so that two or three piles can be loaded at the same time (Section 4.4.1 discusses the dust loading procedure in

Table 4.1: Size distribution of the polystyrene microspheres used. Dust sizes will be referred to by their integer values: we will say '15 micron dust pile' as opposed to '14.9 micron dust pile'.

Nominal Diameter	Standard Deviation
5.3 μm	0.6 μm
10.0 μm	0.8 μm
14.9 μm	1.2 μm
20.0 μm	1.9 μm
24.8 μm	2.5 μm

depth). The dust is loaded onto the plates beside the holes and then scraped into the holes with the scraping sheet. Sometimes a single pile is unsatisfactory and has to be reloaded, in which case the single hole pile form plate is used. The plate guide is used to ensure that the three hole plate form is lifted perfectly vertically (see Figure 4.4).

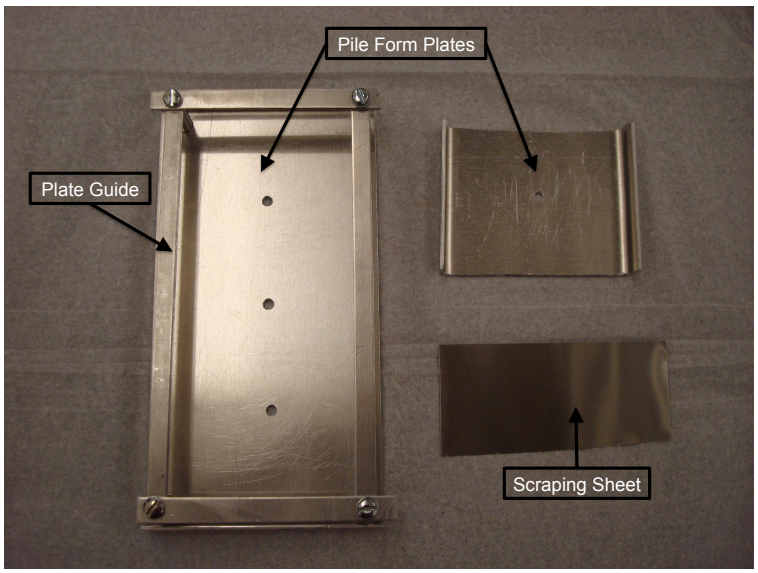

Figure 4.3: Two pile form plates, the plate guide and scraping sheet. The diameters of the holes in the pile form plates are 4 mm. The scraping sheet is used to scrape the dust (which is initially deposited on the pile form plate) into the holes.

Emissive probe measurements are taken above the 4mm dust piles, a 1cm dust pile, a 1cm rubber disk and a 4mm rubber disk. The disks and forms for these piles are shown in Figure 4.5. A photo of the dust piles on the graphite plate in the chamber after pile spreading can be seen in Figure 4.6.

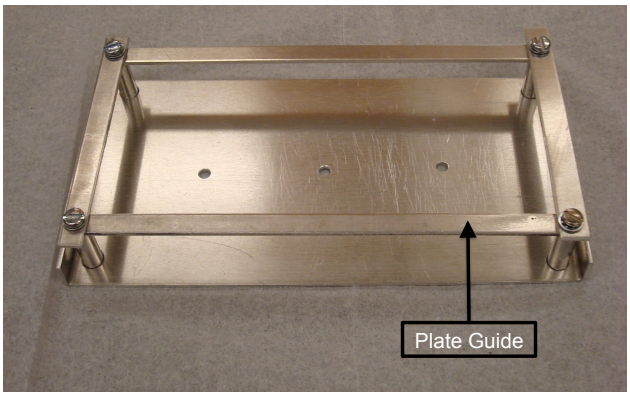

Figure 4.4: Side view of plate guide and three hole pile form plate. The plate guide is used to help lift the pile form plate straight up.

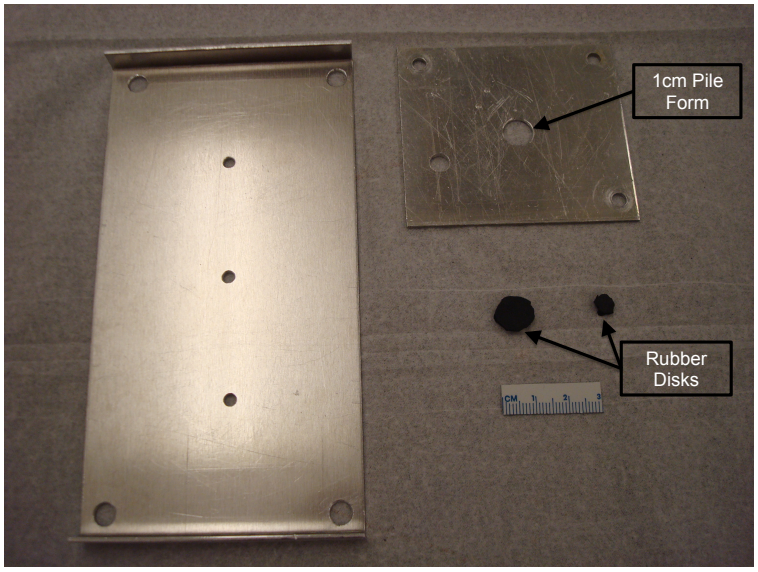

Figure 4.5: The three hole pile form plate, two rubber disks and the 1cm dust form plate. The legs of the plate guide sit in the holes in the corners of the three hole pile form plate. Only the center, 1cm diameter hole is used in the smaller plate.

4.3.3 Diagnostics

A 1.9 megapixel Meade camera mounted in a vice was used to automatically photograph the dust piles. The Meade camera came with the AutoStar Envisage software, which provided a GUI for adjusting the exposure time and automating the image capture process. The focus was manually adjusted. During the experiment, a photo was taken prior to biasing the graphite plate.

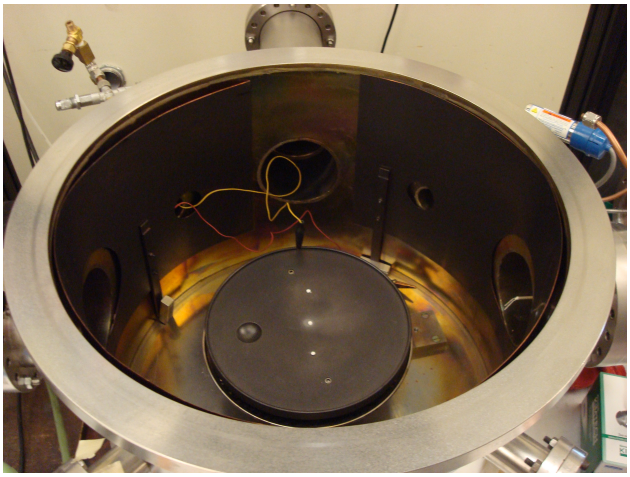

Figure 4.6: Top view of dust piles on the graphite plate in the open chamber. Note the alligator clip (yellow wire) attached to the graphite plate used to bias the plate. The crater (left hand side of the graphite plate) is not used in this experiment.

One photo was taken every minute for the first ten minutes after the plate was biased. Photos were then taken every five minutes for the following 50 minutes. Since this experiment is only concerned with the total extent of the pile spreading, only the first and last images were used. The additional images taken throughout the exposure to the plasma sheath could be used to characterize the rate of spreading of the dust piles.

For some of the experiments, an emissive probe was used to measure the vertical and horizontal plasma potential profiles above the dust and plate. Emissive probes are based on the same principle as Langmuir probes: when the potential of the probe is less than the potential of the plasma, the probe will collect a positive current and when the potential of the probe is greater than the potential of the plasma, the probe will collect a negative current. When the current to the probe is zero, it is at the floating potential. Given a range of potentials (in our case -80.5V to 10.2V), we identify the probe potential that results in a specified current (in our case, -0.1μA, which was calibrated using the inflection point method [54]). The plasma potential at this spatial location is then taken to be the probe potential. When the potential of the probe equals the potential of the plasma, the current to the probe will be slightly negative due to the thermal motion of the electrons, thus, the -0.1μA offset is used.

The emissive probe is manually placed above the dust piles using the chamber's top window to verify the position. The vertical motion of the probe is controlled manually and data is captured using a LabView program. The rotational motion of the emissive probe is controlled by a small motor and a LabView program. An image of the emissive probe connected to the motor can be seen in Figure 4.7.

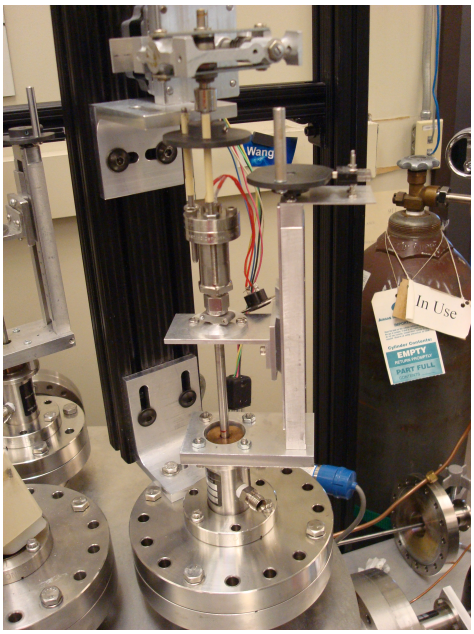

Figure 4.7: Emissive probe connected to motor.

A Langmuir probe is used to measure characteristics of the bulk plasma. Like the emissive probe, the wire is biased to a range of voltages and the resulting current to the wire is recorded. By plotting the current to the probe as a function of probe potential, it is possible to determine the electron density, electron temperature and plasma potential. The inflection point method is used to determine the plasma potential - the plasma potential is the point where the slope of the current vs potential plot (I-V plot, see Figure 4.8(a)) is maximized. For our plasma, the bulk plasma potential is 2.6V. Our plasma has a bi-Maxwellian distribution function. The two populations of electrons (hot and cold) can be seen by the non-linearity of the transition region of Figure 4.8(b). The electron temperatures are given from the inverse of the slope of the transition region of the ln(I)-V plot ($T_{e,cold} = 1.45$eV and $T_{e,hot} = 4.18$eV).

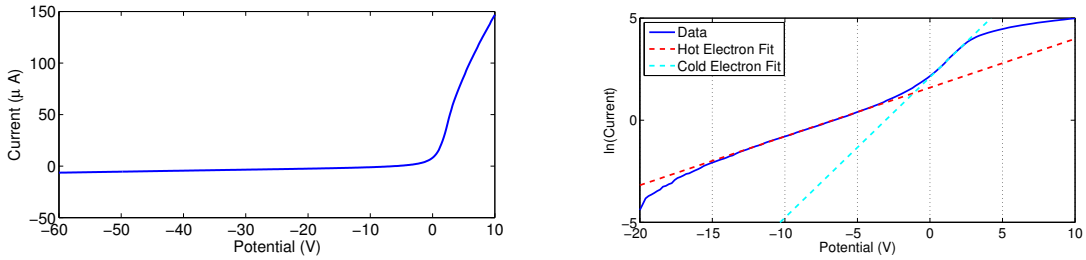

(a) I-V Plot (b) ln(I)-V Plot

Figure 4.8: Current vs potential plot measured with a Langmuir probe to determine the characteristics of the plasma. In (b), the ion current has been removed. Plasma Potential: 2.6V.

The number density of the electron species can be calculated from the saturation currents. The total saturation current is the current when the probe is at the plasma potential. The saturation current for the hot electron species is given by the intersection of the linear approximations for the two species (shown in Figure 4.8(b)). The saturation current of the cold electrons is simply the difference of the total saturation current and the saturation current due to the hot electrons. The electron density is given by:

$$n_{e,i} = \frac{I_{sat,i}}{v_{e,i} A_p q_e} \tag{4.7}$$

where $I_{sat,i}$ is the saturation current of the ith species, $v_{e,i}$ is the electron velocity of the ith species, A_p is the surface area of the probe ($2.29 \times 10^{-5}\mathrm{m}^2$), and q_e is the charge of an electron. The electron velocity is given by:

$$v_{e,i} = \sqrt{\frac{q_e T_{e,i}}{2\pi m_e}} \tag{4.8}$$

Note that $T_{e,i}$ must be given in electron-volts and m_e is the mass of an electron. From this analysis, the density of the cold electrons is $5.8 \times 10^{13}\mathrm{m}^{-3}$, the density of the hot electrons is $3.0 \times 10^{12}\mathrm{m}^{-3}$, and the total electron density is $6.1 \times 10^{13}\mathrm{m}^{-3}$. The effective temperature of the plasma is given by:

$$T_{eff} = \left[\frac{n_{e,cold}}{n_{e,tot} T_{e,cold}} + \frac{n_{e,hot}}{n_{e,tot} T_{e,hot}} \right]^{-1} \tag{4.9}$$

The effective electron temperature of our plasma is 1.50eV. More information on Langmuir probe analysis can be found in [56, 9].

4.4 Procedure

The following is a detailed description of the procedure used to run the experiments presented in this chapter, beginning with loading the dust into the chamber and ending with breaking the vacuum in the chamber. The procedure begins with the chamber lid open and the graphite plate free from dust.

4.4.1 Basic Pile Spreading

(1) Clean the graphite plate using a Kimwipe. This removes any remaining dust grains and evens out any excessively bright areas of the graphite. Disconnect the alligator clip from the plate in order to get more space while loading the dust.

(2) Clean pile form plates and scraping metal with ethanol to ensure that there are no foreign particles or dust grains from previous experiments in the forms.

(3) Place three hole pile form plate on the graphite plate in the chamber with the plate guide. Center the pile form plate on the graphite plate. Ensure that the pile form plate slides easily along the plate guide.

(4) Person 1 (in my case, Xu Wang) holds the pile form plate steady on the graphite plate with his fingers. Thumbs of Person 1 rest on the plate guide. It is necessary to hold the plate form steady in order to create uniform piles. Person 1 and Person 2 should be wearing gloves to avoid getting oils in the chamber. It is advisable for both Person 1 and Person 2 to wear N95 masks if handling small dust grains.

(5) Person 2 dispenses the dust onto the pile form plate near the holes on the plate. Do not pour the dust directly into the holes, as there is likely to be movement of the plate during the preparation of the piles. It can be very difficult to dispense the dust (especially the small, cohesive grains) onto the plate and periodically a small wire may be inserted into the dust container (shaped like an eye dropper) to break up clumps. For experiments using

5,15 and 25 micron particles, fill all 3 holes in the pile form plate. For experiments using 10 and 20 micron particles, only fill two of the holes to avoid interaction of the plasma sheaths of the piles.

(6) Once the dust for all the piles has been dispensed onto the pile form plate, Person 2 takes the scraping sheet and scrapes each sample of dust into the appropriate pile form hole. Between each dust particle size, clean the end of the scraping sheet with a Kimwipe. Scrape over each hole 3 times in order to ensure that the hole is completely filled and the dust piles are packed the same amount. Also, the slight vibrations caused by the scraping will break the bonds between the dust and the sides of the pile form plate. For very cohesive grains, it may be necessary to 'cut' the grains by using the scraping sheet in an up and down motion to break the cohesive bonds between grains and allow them to fall into the pile form hole.

(7) Once all the pile forms are filled, Person 1 slowly slides the pile form plate up along the plate guide. It is necessary to complete this step very carefully because if the dust drops from the pile form or the pile form is lifted unevenly, the piles will spread and be unusable.

(8) Inspect piles. Piles should be as cylindrical as possible. If there is a small amount of spreading, use a folded Kimwipe to remove the offending grains. If there is a large amount of spreading, use a Kimwipe to remove the pile and place a new pile using the one hole pile form. When using the one hole pile form, there is no plate guide, so it is imperative that Person 1 carefully lifts the plate.

(9) Use level to make sure the graphite plate is level. Adjust as necessary.

(10) Attach alligator clip to the graphite plate. This clip is used to bias the plate and should be covered as much as possible with an insulator to prevent sparking between the clip and the plate.

(11) Lower the chamber lid. If planning on doing emissive probe measurements, rotate the chamber lid so that the emissive probe (when rotated) can sweep over two piles. When

finished adjusting the lid, position the emissive probe and Langmuir probe to the side of the chamber.

(12) Close the chamber venting valve.

(13) Turn on the roughing pump. Slowly open the valve to the roughing pump. The valve must be opened slowly in order to avoid disturbing the dust piles by having a sudden large draft in the chamber.

(14) Once the chamber pressure has reached 30mT, turn on the turbopump. Do not turn on the turbopump at higher pressures or the pump fan blades may be damaged.

(15) Once the chamber pressure is less than 0.1mT, turn on the ion pressure gauge.

(16) Let the chamber pump down overnight. For this experiment, the dust particles were exposed to vacuum for 18-22 hours.

(17) (To occur following day) Note the pressure in the chamber. Pressure should be $\leq 1 \times 10^{-6}$mT. If the pressure is high, there is a leak. In use the Nitrogen gauge and a wand connect to an argon source to identify the leak. Most likely, it is necessary to change the grease along the rubber seal on the chamber lid. If the pressure is fluctuating, then the leak is likely from the emissive probe. Try moving the probe up and down or rotating to stop the leak. If the leak persists, attach a vacuum pump to the valve in the side of the emissive probe assembly.

(18) Open valve at top of argon canister.

(19) Vent argon hose to ensure that only argon is in the line connected to the chamber.

(20) Open rough valve between the fine tuning valve and the chamber. This will cause a slight, temporary increase in the chamber pressure as the residual gas in the line is sucked out by the turbopump.

(21) Open fine tuning valve until the pressure in the chamber is 1×10^{-3}mT.

(22) Turn on the filament bias and heating mechanism. Set the filament bias to ~ -40 V. Adjust the filament heating bias until the filament current is $\sim$ 180mA. The filament takes about twenty minutes to heat and produce a constant stream of electrons. Adjust the filament heating bias as necessary until the current is at $\sim$ 200mA.

(23) Set the graphite plate power supply to -60V. Make sure that the lead is not connected to the power supply!

(24) Open AutoStar Envisage (the software that controls the camera). Turn on the overhead light on the chamber. Adjust the camera focus as necessary. Adjust the exposure time (0.017 used here) and the Shadow Enhance (3 used here) as necessary. Set the Save Procedure to Nominal Operation. Press the Start button to take the photo of the dust piles prior to the application of the plate bias. Press Stop after the image has been captured.

(25) Set the Save Procedure to Time Lapse, with a Frame Time of 1 second, Wait Time of 1 minute, Total Time of 10:30 minutes.

(26) Connect the lead from the plate bias clip to the power supply that has been set to -60V.

(27) A script has been created with the AutoHotkey program to control the image capture program. Since the camera program is designed to control a telescope, before every image is captured, a pop-up will appear that warns the user that the telescope is not connected. The AutoHotkey program will automatically press the OK button on the pop-up allowing the program to capture the image. Start the AutoHotkey program now. It will begin taking photos every minute for 10 minutes.

(28) Once the AutoHotkey program has finished, adjust the Save Procedure in the AutoStar Envisage program so that the Wait Time is 5 minutes and the Total Time is 50:30 minutes.

(29) Adjust the AutoHotkey program to have a Wait Time of 300 seconds.

(30) Run the AutoHotkey program. It will take photos every 5 minutes for 50 minutes.

(31) While the program is running, adjust the filament heating voltage as necessary to ensure that the current remains at approximately 200mA.

(32) Towards the end of the program, inspect the images taken and make sure that the piles are no longer spreading. If the piles appear to still be spreading, run the experiment longer.

(33) After the program is done running (and the piles are not longer spreading), it is possible to make emissive probe and Langmuir probe measurements (see Section 4.4.2 and Section 4.4.3).

(34) After all desired measurements have been made, turn off the light above the chamber. Turn the plate bias to zero and unplug the lead.

(35) Turn the filament emission and heating biases to zero. Turn off the power sources.

(36) Close the fine tuning argon valve. Close the valve on the top of the argon canister. Once the pressure in the chamber has stabilized, close the rough argon valve (between the fine tuning valve and the chamber).

(37) Turn off the turbopump and ion pressure gauge. Wait 15 minutes to allow the turbopump to slow down. It is necessary to wait in order to avoid damaging the pump blades.

(38) Close the valve from the chamber to the roughing pump. It is necessary to close this pump in order to avoid sucking oil from the roughing pump into the chamber when repressurizing the chamber.

(39) Turn off the roughing pump. Slowly open the venting valve.

(40) Once the pressure in the chamber reaches atmospheric pressure (about 580 T in Boulder), attach the pulley system to the chamber lid and lift the lid.

(41) Clean the dust out of the chamber using a vacuum cleaner.

4.4.2 Emissive Probe

Both horizontal and vertical emissive probe measurements were taken. This protocol will assume that the dust piles are done spreading and that the plasma environment has not been changed. Essentially, this protocol would be inserted before Step 34 in the above protocol. Prior to pumping down the vacuum chamber, the lid of the chamber must be positioned so that the emissive probe can be positioned above the center of the piles of interest. We have found that it is only possible to position the probe so that it will be above the center of two of the three dust piles for a given vacuum chamber lid placement. Thus, after measurements have been taken above two piles, it is necessary to break vacuum, reposition the chamber lid and pump down the chamber again in order to measure the potential over the third pile. The emissive probe measurements used are based on the method described by [16].

(1) Manually rotate the probe into the desired position above the center one of the dust piles. Adjust the height of the probe to the desired location (here, 3mm or 5mm).

(2) If doing a horizontal emissive probe sweep, attach the motor to the probe (see Figure 4.7). Make sure that the motor mount is level in order to ensure that the rotation occurs as desired. For a vertical profile, ensure that the probe is the desired height above the pile (usually start 3mm above the pile).

(3) Connect the motor power source (horizontal only) and the data cord.

(4) Open the LabView Emissive Probe program (either horizontal or vertical) and ensure that the data collection is set to the proper port.

(5) For the horizontal collection, test the LabView program's control of the motor to make sure the probe will sweep over both piles.

(6) Set the power supplies for the emissive probe to ~ 10V and ~ -80V.

(7) Turn on the power supply for the motor (9V) (horizontal only). If doing a vertical test,

instead connect the 'Clicker' box to the emissive probe, so that the data is collected at the proper heights. When collecting a vertical profile, the potential is measured every 5mm.

(8) Adjust the emission until the current is stable.

(9) For the horizontal collection, set the desired direction and extent of the probe rotation and run the LabView program. For the vertical collection, run the program and begin to manually crank the rotating disk to move the probe up.

4.4.3 Langmuir Probe

A Langmuir probe is used to measure the potential of the bulk plasma, the electron temperature and the plasma density. Although we do not use these parameters in any calculations, they are documented in order to ensure the reproducibility of the experiment. Additionally, it is advisable to measure the plasma potential at the beginning of any set of experiment runs in order to ensure that the vacuum chamber is clean. In theory, a plasma should have equal numbers of electrons and ions, and consequently have a net negative charge of zero. Since the plasma is contained by the walls of the vacuum chamber (which are grounded), in equilibrium the net current to the chamber walls will be zero. Since electrons are much lighter than ions, if the plasma potential at the wall is the same as the plasma potential of the bulk, then the net current to the wall will be negative. Thus, there must be some potential barrier in order to ensure a net current of zero to the wall. As a result, in a clean vacuum chamber, the bulk potential of the plasma is slightly positive, since the wall is grounded. If the vacuum chamber is dirty (for instance, there is oil residue on the walls), electrons will accumulate on the dirt, which is insulating. The electrons accumulated on the oil act to effectively lower the potential of the chamber walls. In equilibrium, the net current to the walls continues to be zero. Thus, the potential barrier between the bulk and the walls still exists, but the potential of the bulk plasma is decreased and can become negative.

As with the emissive probe measurements, this protocol would be inserted before Step 34 in the basic dust spreading protocol. The goal is to characterize the plasma environment.

(1) Disconnect the graphite plate from the power source. Position the probe in the bulk plasma (at least 5cm above the plate).

(2) Increase the filament heating, until the current is approximately 400mA.

(3) Bias the probe +150V for 1 minute to vaporize off any contaminants (usually pump oil). The probe will glow violet.

(4) Turn off the probe heating element and return the filament current to the normal level (200mA).

(5) Connect the data cord. Set the probe bias range from -60V to 10V.

(6) Run the Langmuir Probe LabView program to collect the current-voltage characteristics.

4.4.4 Image Analysis

In order to quantitatively assess the spreading of the dust piles, a script was written to compare the final image of the piles to the initial image taken immediately after the graphite plate was biased. The base and center of each pile within starting image were located manually. Since the camera was not manipulated during the experiment, the location of the piles were the same for each image. The brightness values of the image at the start of the experiment were subtracted from the brightness values of the image at the end of the experiment. Any pixels with a residual reflectance of less than 1% were set to zero. Pixels in the initial image with a minimum reflectance of 25% were used to create a mask of the initial pile location. The reflectances of pixels in the mask were set to zero, thus removing the possibility of exaggerated spreading measurements due to brightening of the pile during the experiment. The resulting 'negative' showed the pixels that increased in brightness over the course of the experiment, indicating spreading of the piles. The extent of the spreading was measured radially and averaged over the two sides of the piles. Since the base of the pile was located manually and was subject to error, the spreading was averaged

over all rows of the image (starting from the base of the pile) where the extent of spreading was increasing.

4.5 Results

Three dust piles (one with 5 micron particles, one with 15 micron particles, and one with 25 micron particles) were placed on the conducting plate in the vacuum chamber. The vacuum chamber was pumped down to a pressure of 1×10^{-9} Torr for approximately 20 hours. The duration of the dust in vacuum is important since increasing the duration in vacuum increases the strength of the cohesion between grains due to outgassing. Figure 4.9 shows grayscale images of the dust piles prior to biasing the plate and after being exposed to the plasma sheath for approximately one hour. Figure 4.10 shows false color images of the piles before and after spreading. The slight brightness about the center pile in Figure 4.10 is caused by a reflection from the back of the chamber and does not influence our results. Additionally, a small reflection can be seen below each pile in Figure 4.10. From Figure 4.10, it can be seen that the 15 micron pile (center in the image) spreads, while the other two piles (5 micron, and 25 micron) do not appear to spread from visual inspection. Since all three piles began with the same initial structure, we can infer that the initial electric field at the edge of all three piles was the same. Thus, the electric field required to loft the 15 micron particles was less than the electrostatic force supplied, resulting in spreading. However, the electrostatic force required to spread the other particle sizes was greater than that provided by the plasma environment. Thus, we can conclude that the electrostatic force required to electrostatically loft the 15 micron dust particles is less than that required to loft 5 micron and 25 micron particles. The experiment was repeated with 10 and 20 micron particle as well. The images were quantitatively analyzed as described in Section 4.4.4. The resulting average extent of radial spreading is given in Table 4.2. The data in Table 4.2 is presented graphically in Figure 4.11. Note that since both the 10 and 20 micron dust samples spread, it was necessary to only load 2 piles on the graphite plate at a time to avoid interactions between the plasma sheaths. A pile of 15 micron dust was included in every experiment so that the measured spreading could be compared with the 5, 15, and 25 micron

dust pile experiments.

Table 4.2: Radial spreading of dust piles after 1 hour exposure to a plasma sheath generated by a -60V biased plate. The data shown is for three trials, with the exception of the 15 micron dust, which was repeated nine times. Note that 5 pixels $\approx$ 1 mm.

Dust Diameter	Average Spreading (pixels)	Standard Deviation (pixels)
5 μm	1.75	0.354
10 μm	16.3	9.69
15 μm	53.8	15.3
20 μm	26.1	1.51
25 μm	1.5	0

From Table 4.2 and Figure 4.11, it can be seen that there is a significant difference in the average radial spreading of the pile of 15 micron dust as compared to the other dust sizes tested. Although we do not visually observe any spreading of the piles of 5 micron or 25 micron dust, our image analysis tool detected a very small degree of spreading of these piles. Additionally, the 10 micron and 20 micron dust particles are seen to spread less than the 15 micron dust, but more than the 5 micron and 25 micron piles.

Returning to our theoretical calculations, Figure 4.12 shows the electric field required to loft particles (given by Eq. (4.5)) for the polystyrene microspheres used. The three curves shown correspond to different levels of particle cleanliness (S), which correspond to the thickness of adsorbed molecules between the dust grains and the surface. The cleanliness of the sample determines the particle size where the minimum electric field required for lofting occurs (see Eq. (4.6)). Thus, in Figure 4.12, we have used three different values of cleanliness that result in the curve minimum being located at 10, 15, and 20 microns. However, we know that the true curve minimum is located between 10 and 20 microns because the other two piles exhibit less spreading. Thus, we are able to constrain the cleanliness of the dust samples used to between 0.03 and 0.06. Additionally, we have experimentally demonstrated the existence of the minimum electric field required for dust lofting at an intermediate particle size, as predicted by the theory presented in Chapter 3.

In addition to generally proving the theory provided in Chapter 3, the increased spreading

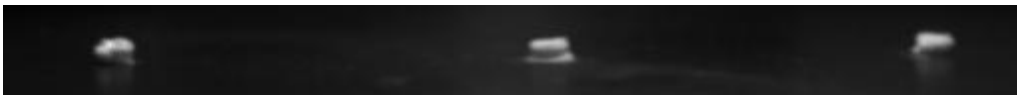

(a) Before

(b) After

Figure 4.9: 3 piles of polystyrene dust before and after being exposed to the plasma sheath for 1 hour. The dust particles in the left pile have a nominal diameter of approximately 5 microns. Similarly, the middle pile has 15 micron dust, and the right pile has 25 micron dust. The diameter of each pile is 4 mm.

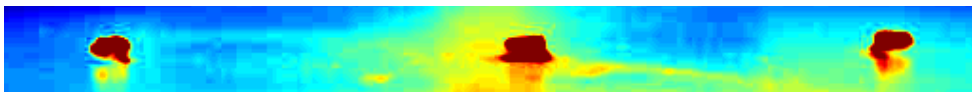

(a) Before

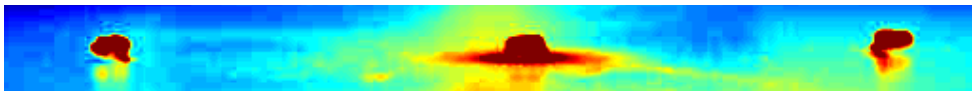

(b) After

Figure 4.10: False color images of the dust piles shown in Figure 4.9, used in order to more easily see the extent of the pile spreading.

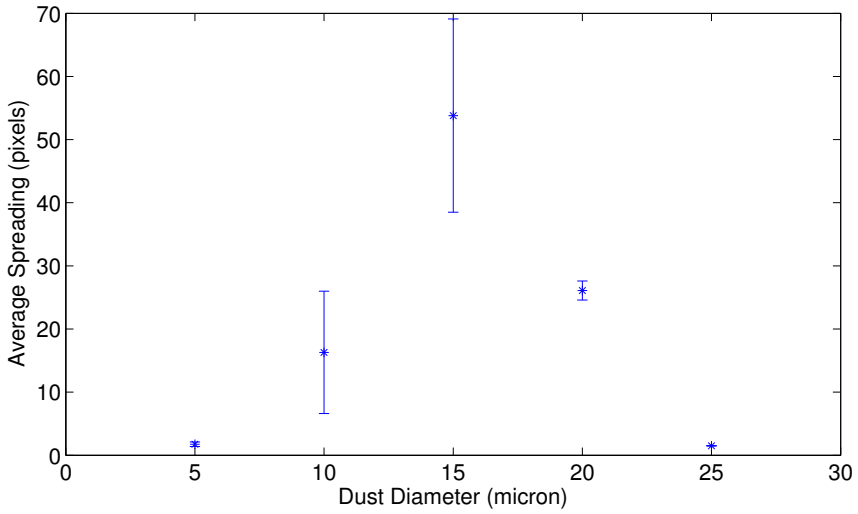

Figure 4.11: Plot of dust spreading as a function of size with 1-σ error bars.

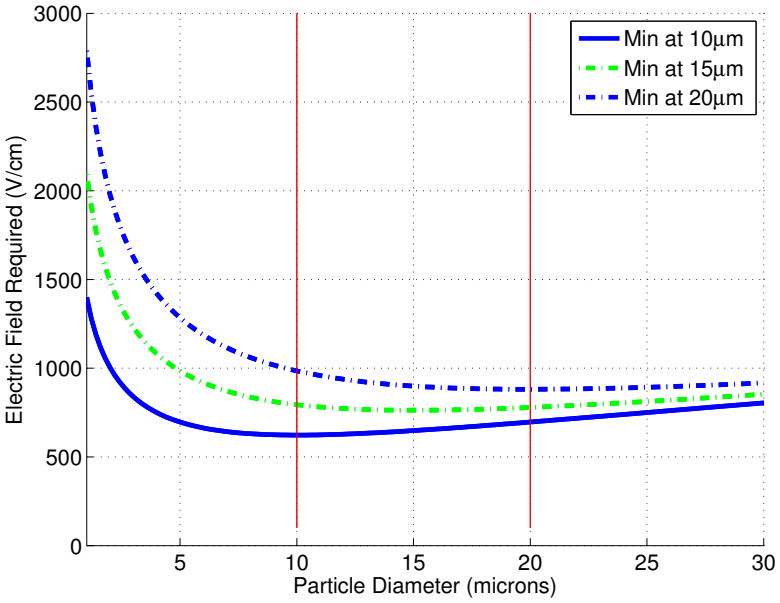

Figure 4.12: Electric field required to loft dust particles as a function of particle diameter calculated from Eq. (4.5). Values of cohesion were used that resulting in the electric field minimum being at a particle size of 10, 15, or 20 microns. The true curve must be between the curves with the minima at 10 and 20 microns.

of 10, 15 and 20 micron particles compared to larger and smaller particles also proves the general form of the electrostatic force felt by a insulating dust grain on the plate. In the development of

the theory presented in Chapter 3 and Section 4.2, we assume that the charge on the grain is given by Gauss' law. Thus, the $F_{es} \propto E^2 d^2$. By comparing the measured electric field strength and that predicted by theory, we will discuss later in this chapter that, as predicted in Chapter 3, there is likely some charge amplification beyond the level predicted by Gauss' law. However, the presence of a cohesion dominated leg of the curve of the electric field required for lofting (where decreasing the particle size increases the electric field required for lofting), proves that, even for very small insulators, the charge on the particles is proportional to the Gauss' law prediction.

We have also taken emissive probe measurements of the horizontal variation in the plasma potential at several heights after the dust has stopped spreading. The emissive probe is only used after the dust stops spreading because it does not yield reliable measurements at the beginning of the experiment due to interaction with mobile dust. In order to record the horizontal variation in the plasma potential, the emissive probe is rotated. Since the dust piles are placed in a straight line in the chamber, the rotating emissive probe only measures the potential above the center of two piles for a given placement of the probe. Thus, in order to obtain the potential variation above the third pile, it is necessary to break vacuum and reposition the probe. In Figure 4.13 we present the potential measured in Data Captures 1 and 2, where the plasma conditions are as similar as possible, but not strictly identical between the two measurements. The 'adjusted' data is created by simply shifting the Data Capture 2 to match the peak potential obtained in Data Capture 1. Each of the potential peaks in Figure 4.13 corresponds to a pile of dust (from left to right: 5 micron, 15 micron, 25 micron). The width of the central peak in Figure 4.13 confirms our visual observation that the pile of 15 micron dust spreads more than either the 5 micron or 25 micron dust. The potentials measured by the probe are influenced by the 2D nature of the emitting wire (which is approximately the same length as the diameter of the dust piles). Thus, at a given height, the probe may be measuring both the potential in the sheath above the dust pile as well as the sheath above the conducting plate. Since the 15 micron pile has spread, the potential measurement at the center of the pile is less influenced by the plate sheath than the potential measurement at the center of the other two piles. Thus, the maximum potential of the central peak is larger than

that of the other two peaks. This hypothesis is supported by the observation that the maximum potentials of the other two peaks are approximately equal, as would be expected since they both have the same diameter. Note that the magnitudes of the potentials measured at 5mm above the dust piles (Figure 4.13(b)) are less than those measured at an altitude of 3mm (Figure 4.13(a)), as expected.

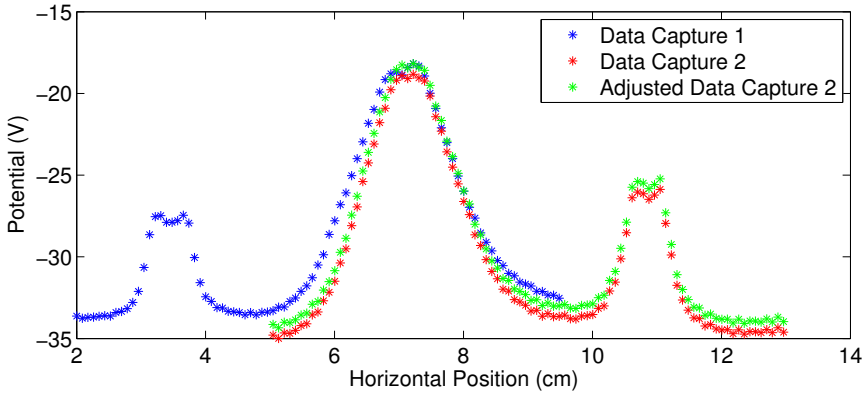

(a) Altitude of 3mm

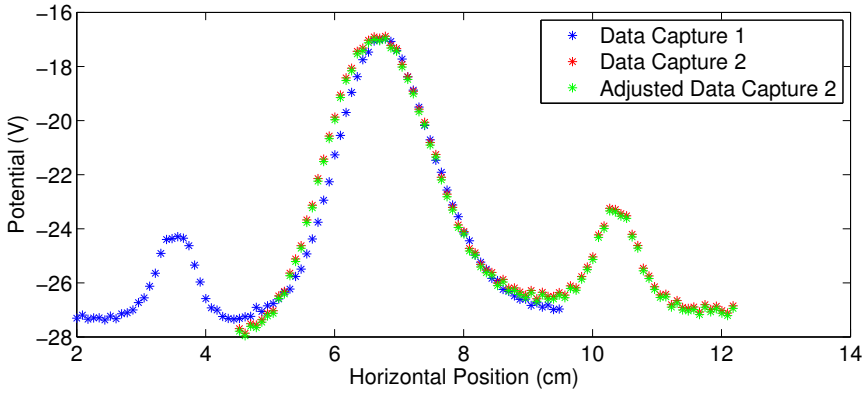

(b) Altitude of 5mm

Figure 4.13: Horizontal variation in the plasma potential. Note that the dust piles are approximately 1.5mm thick. The peak seen on the left is the pile of 5 micron dust particles, the center peak is above the 15 micron dust, and the right peak is above the 15 micron dust pile. The data was taken in two separate runs in order for the emissive probe to be centered over the dust piles of interest (either the 5 and 15 micron piles or the 15 and 25 micron piles). Since the vacuum had to be broken between the two measurements, the plasma conditions between the two measurements are not identical. The 'adjusted' data is simply Data Capture 2 shifted down so that the peak potential matches that measured in Data Capture 1.

Figure 4.14 shows the horizontal electric field at an altitude of 3mm above the conducting

plate. The electric field was calculated by numerically differentiating the smoothed potential data, since the electric field is just the gradient of the potential. Note that the electric field at the edges of the pile of 5 micron and pile of 25 micron dust is greater than the electric field at the edges of the pile of 15 micron dust. This agrees with our hypothesis about the mechanism of dust spreading. Recall, we have stated that if the electric field is large enough to overcome gravity and cohesion, the dust pile will spread. Thus, at the beginning of the experiment, the electric field at the edges of each of the piles should be the same since all the piles have the same form and experience the same plasma environment. Since the pile of 15 micron dust spreads more than the others, we know that the electric field required to separate the 15 micron particles from the surface is less than that required to loft 5 micron or 25 micron dust. The 15 micron dust pile will stop spreading when the electric field at the edge of the pile is not large enough to overcome gravity and cohesion. Thus, we expect the electric field at the edge of the pile of 15 micron dust to be less than that at the edge of the 5 micron and 25 micron piles. While we only present the calculated *horizontal* electric field (which is not directly responsible for electrostatic lofting), it is involved in breaking the cohesive bonds between grains, as required for lofting.

The horizontal electric field profile shown in Figure 4.14 was repeated for three trials. The average maximum electric field at the edge of each pile and standard deviation are shown in Table 4.3. Although the standard deviations are somewhat large, the data supports the assertion that the electric field at the edges of the 5 and 25 micron piles are larger than those of the 15 micron pile.

Table 4.3: Horizontal electric fields at the pile edges. Statistics from three experiments.

Dust Diameter	Average Electric Field (V/cm)	Standard Deviation (V/cm)
5 μm	17.4	4.53
15 μm	13.3	1.80
25 μm	19.2	3.65

Using the emissive probe, we also took measurements of the vertical potential profile above the dust piles. Since dust particles were observed to move and the plate was negatively biased (meaning

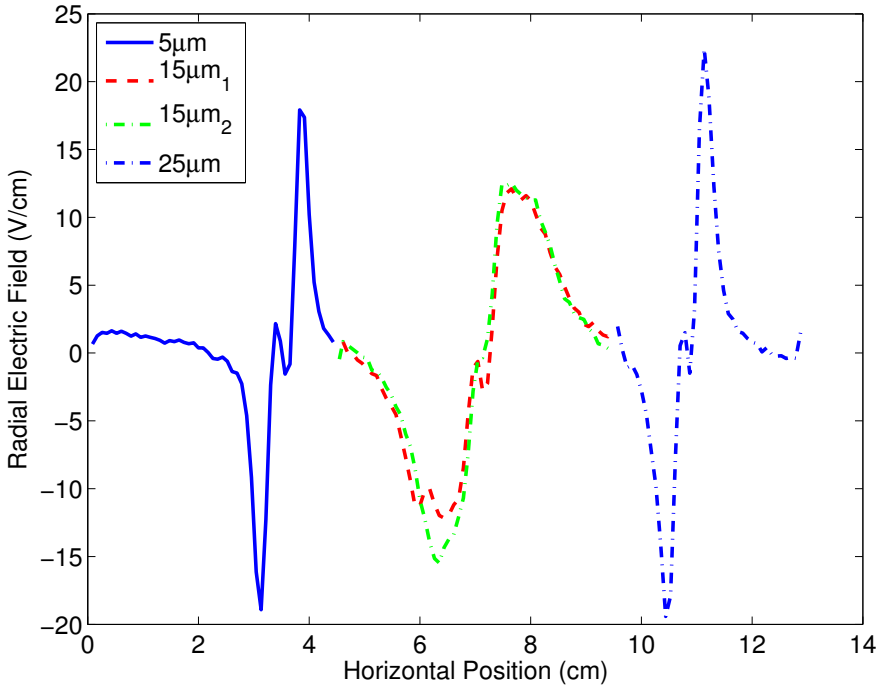

Figure 4.14: Horizontal electric field calculated numerically from smoothed measurements of the potential. The edges of the piles correspond the the extrema of the electric field. Note that the electric fields at the edges of the piles of 5 micron dust and 25 micron dust are greater than those at the edges of the pile of 15 micron dust. The positive electric field direction is defined to be to the right.

that the dust grains acquired a positive charge), we expected there to be a non-monotonic sheath above the dust piles. Additionally, the presence of a non-monotonic sheath in this experimental set-up had been previously observed by Wang *et al.*[59]. However, our ability to measure small scale variations in the plasma potential was limited by our measurement accuracy. Specifically, the length of our emitting wire was approximately the same as the diameter of our dust piles, the probe could only be brought within a few millimeters of the dust piles, and the probe recorded data only every 5mm in altitude. Given the experimental limitations, we were unable to measure a non-monotonic sheath above our 4mm diameter dust piles. Since part of our measurement limitations were due to the relative size of the dust pile with respect to the probe, we repeated our measurements above a 1cm diameter pile of dust. When the vertical potential profile was measured

above a 1cm diameter dust pile with the plate biased to -80V (resulting in a much larger plasma sheath), a potential minimum was detected at an altitude of 4mm above the dust pile. When the plate bias was decreased to -60V (as in the experiments here), a non-monotonic sheath was not detected. This is likely due to the small spatial extent of the plasma sheath for these conditions.

Although the horizontal electric field is not directly responsible for electrostatic dust lofting, it is involved in the breaking the cohesive bonds between grains. We estimate that the vertical electric fields are the same order of magnitude as the horizontal electric fields. The theoretically predicted electric fields required to loft dust (Figure 4.12) are an order of magnitude larger than the experimentally observed electric fields (Figure 4.13). In our model, we assumed that the dust charge was given by Gauss' law, which is probably a conservative estimate (see discussion in [24]). The charging of the dust particles could be an order of magnitude larger than the Gauss' law approximation, due to the discrete nature of dust charging, small scale electric field variations, and the complexity of charging an insulator [51].

4.6 Discussion and Conclusions

We have presented a theory that shows that strong inter-grain cohesion will dictate the electrostatic force required to loft small dust particles. Considering cohesion and gravity, we see that there exists a grain size that requires the smallest surface electric field to be lofted. This theory has been confirmed experimentally by placing piles of different sized grains on a biased plate in a plasma. In this experimental work, we have observed the movement of 15 micron grains, but negligible movement of larger or smaller grains. Additionally, we have seen moderate movement of 10 and 20 micron grains. Thus, the surface electric field required to electrostatically loft 15 micron polystyrene microspheres is less than that required to electrostatically loft 5 micron or 25 micron grains. The spreading of the pile of 15 micron grains has been confirmed both visually and by measuring the plasma potential at various altitudes above the piles of dust grains. Additionally, we confirm that the electric field required to loft 15 micron grains is less than that required by smaller and larger particles by measuring the horizontal electric field at the edge of these piles. We

find that the horizontal electric fields at the edges of the 5 micron and 25 micron piles are greater than those at the edges of the 15 micron pile. Thus, we have experimentally demonstrated that cohesion dictates the electric field strength required to electrostatically loft small grains and that intermediately-sized grains require a smaller electric field for lofting than smaller or larger grains. This has important implications for our interpretation of limb observations of airless bodies and future studies of the feasibility of electrostatic dust lofting.

Chapter 5

1D Dust Levitation Dynamics

5.1 Introduction

Although the occurrence of electrostatic particle lofting has not been definitively proven, it is necessary to understand the motion of dust particles in order to evaluate the feasibility of electrostatically-controlled dust motion as a creation mechanism for the Eros dust ponds and Lunar Horizon Glow. Since a realistic dust launching mechanism has not been identified, previous numerical studies of dust transport have specified initial particle charges and velocities that may or may not be representative of conditions present *in situ*. It has been seen that some particles experience an oscillatory motion (aka levitation) above the surface of the central body in simulations [38, 13, 28, 42]. Nitter *et al.* [38] propagate the trajectories of particles both in a monotonically decreasing and a non-monotonic sheath potential profile. Colwell *et al.* [13, 28] use a simplified sheath model from Grard and Tunaley [20] and investigate the accumulation of dust in craters on Eros.

There is also significant uncertainty in the structure of the plasma sheath near the surface of the Moon. Some information about the surface electric field strength can be inferred from Lunar Prospector measurements [21], but we have no direct measurements of the electric potential profile in the plasma sheath. Nitter *et al.* [38] proposed three possible structures of the electric potential profiles. Poppe and Horanyi [42] simulated the sheath in Particle-in-Cell code, where variations in the photoelectron emission distribution function can be modeled.

Although the evidence for electrostatic dust lofting as a natural phenomenon remains in-

conclusive, it is highly likely that dust particles will be lofted during future robotic or human exploration of asteroids and the Moon. Dust grains on the Moon and asteroids are highly abrasive and posed significant challenges for astronauts during the Apollo missions. We would like to understand the movement of dust particles released by exploration activities in order to prevent the formation of a dust cloud around rovers and the deposition of highly abrasive grains in the mechanisms of exploration systems. Additionally, dust shields relying on the electrostatic movement of grains have been developed to keep future lunar exploration vehicles free from dust grains [5]. However, the motion of the artificially charged grains that are cleared from the dust shields is not known. Thus, we would like to understand the motion of lofted dust particles both in order to understand the morphological evolution of these bodies and to predict the effects of future exploration missions on the natural environments.

The presence or absence of levitating dust has important implications both for our understanding of the evolution of asteroids as well as the design of future exploration missions to visit these bodies. Compared to ballistic dust motion, dust levitation provides a relatively quick method of redistributing the regolith across the surface of the body, which could be critical in determining the formation timescales of the Eros dust ponds. Additionally, if dust levitation occurs *in situ*, it will decrease the rate of dust lofting required to produce the dust population seen in spacecraft limb observations (such as those planned by the OSIRIS-REx asteroid sample return mission and the Lunar Horizon Glow observations).

This chapter explores the concept of dust particle levitation from a dynamical systems approach. We identify the location of the equilibria for the Moon and asteroids Eros and Itokawa for a range of particle sizes and three sheath types. The linear stability of the equilibria is assessed through eigenvalue analysis. The nonlinear stability of the system is also studied. We show that it is possible to predict the structure of the state space plot by inspecting the eigenvalues.

5.2 Equations of Motion of Mobile Dust Particles

A dust particle near the surface of an airless body is affected by gravity and an electrostatic force due to the charged particle's interaction with the local plasma environment. The equations of motion for a dust particle in a 1D system are given in Eq. (5.1) and Eq. (5.2), where m_d is the mass of the dust particle (assumed to be spherical), h is the altitude of the dust particle, Q_d is the charge of the dust particle, E is the electric field in the particle's immediate environment, g_s is the local surface gravitational acceleration of the body, and r_c is the radius of the body. A spherical $(1/R^2)$ gravity field is used, in contrast to earlier work ([28, 42]) that assumes a constant gravity field. We neglect any particle-particle interactions (such as collisions or electrostatic attractions) and assume that the dust does not influence the sheath structure. The charge of the particle varies with time (Eq. (5.2)), since the particle is moving through an inhomogeneous plasma environment. The time rate of change of the charge on the particle depends on the currents to the particle, the magnitudes of which are dependent on the time-varying charge on the particle and the altitude of the particle. Thus, since the particle charge is dependent on altitude, Eq. (5.1) and Eq. (5.2) are coupled.

$$m_d\ddot{h} = Q_d E - \frac{m_d g_s}{\left(\frac{h}{r_c}+1\right)^2} \tag{5.1}$$

$$\dot{Q}_d = \sum_i I_i \tag{5.2}$$

The currents flowing to the dust particle (I_i) are due to the solar wind electrons, solar wind ions, dust particle photoemission, and photoelectrons in the sheath. Not only are Eq. (5.1) and Eq. (5.2) coupled, but the system is also dissipative.

Asteroids and the Moon exist within the solar wind plasma. When the solar wind plasma interacts with an airless body's surface, the electrons in the solar wind tend to charge the body negatively. However, an airless body's surface is also charged due to photoelectron emission that occurs when ultraviolet radiation from the Sun excites the surface, which tends to charge the surface

positively. For the case of an asteroid or the Moon, the sunlit surface will be generally be positively charged (for more discussion of lunar surface charging see [21]). Since the surface is positively charged, it will attract electrons resulting in a higher electron density than ion density near the surface. This region is called the plasma sheath. A dust particle near the surface of an asteroid or the Moon will experience currents due to its interaction with the sheath, the solar wind, and its own photoemission. The electrostatic force felt by a charged particle is the product of the particle's charge and the local electric field. The charge on the dust particle varies with time and altitude. The electric field also varies with altitude and, of course, the characteristics of the plasma.

We will consider three types of plasma sheaths, based on the developments by Nitter *et al.* [38], Havnes *et al.* [25], and Grard and Tunaley [20]. Earlier work on dust motion near the asteroid Eros [13, 28] used a simple, analytically-described model of the sheath developed by Grard and Tunaley. In this model, which will be referred to as the analytically-described sheath, the solar wind density is assumed to be constant to the surface of the body. Essentially, only the photoelectron density varies with altitude, creating the potential variation. This sheath has a monotonically-decreasing potential profile. The description of the currents used in the earlier discussion of dust motion on Eros [13, 28] also assumes that the plasma is thermalized, while the development of the potential variation assumes that it is not thermalized. The analytically-described sheath is included for completeness since it has been used in earlier studies of dust motion on Eros.

We also use two sheaths described by Nitter *et al.* [38] (henceforth referred to as the numerically-described sheaths). The description of these sheaths is much more complicated than the analytical description presented by Grard and Tunaley because the density of all of the plasma species (solar wind ions, solar wind electrons, and photoelectrons) are allowed to vary in the sheath. We will be using the monotonically decreasing and non-monotonic potential profiles in [38]. The non-monotonic sheath has been shown to be energetically favorable by Nitter *et al.* [38] (i.e., the potentials in the non-monotonic sheath are less than or equal to the potentials in the monotonic sheath at all altitudes). Non-monotonic sheaths were also seen to develop in a PIC simulation by Poppe *et al.* [42]. Additionally, select Lunar Prospector observations seem to indicate the presence

of a non-monotonic sheath at the Moon [41].

Figure 5.1 shows comparisons between three key characteristics (the electric potential, the electric field strength, and the plasma species number density) of the three sheath types used as a function of altitude above the surface of the body. Note that the structure of the plasma sheath is independent of the mass of the central body. Looking at the potential profiles shown in Figure 5.1(a), we can see that there is an offset between the potential profiles of the numerically-described monotonic and non-monotonic sheaths. The defining characteristic of the monotonic sheath is that the potential monotonically decreases to zero. Although theoretically the potential and electric field for all sheaths must go to zero at $h = \infty$ (due to the quasi-neutrality of the solar wind plasma), in practice for the numerically-described monotonic sheath, we set the potential and electric field to zero when the potential becomes very small. The non-monotonic sheath's potential also approaches zero as the altitude approaches infinity, but it does so after the potential goes negative, since it is non-monotonic. The potential profile of the analytically described sheath is very different from those of the numerically described sheaths. The most substantial difference is that the condition that the potential must go to zero at $h = \infty$ is not enforced for the analytically-described sheath.

Inspecting Figure 5.1(b), we see that the electric field as a function of altitude is very similar for the two numerically-described sheaths. Note that the electric field is the negative gradient of the electric potential. Thus, for high altitudes, we see that the electric field in the monotonically-described sheath approaches zero, while it is negative for the non-monotonic sheath. This result is accentuated when the solar incidence angle (measured from the surface normal) is increased. Additionally, we see that the analytically described sheath has a much larger surface electric field than the two numerically-described sheaths. The rate of decay of the analytically-described sheath is also slower than the numerically-described sheaths, which will be important in later discussion of equilibria altitudes.

In Figure 5.1(c), the number densities of the photoelectrons, solar wind electrons and solar wind ions are plotted for the three sheaths used. Note that the analytical sheath assumes that the solar wind electron and ion densities do not vary with altitude. Additionally, although not

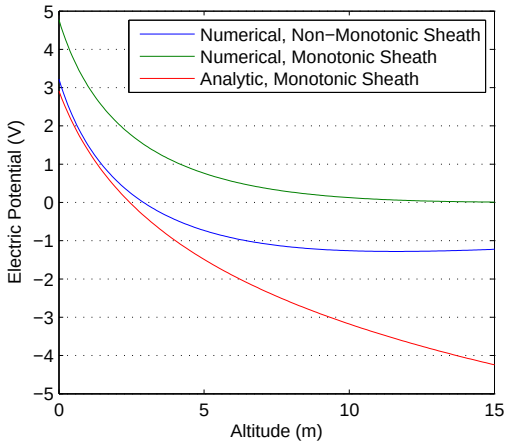

(a) Electric Potential

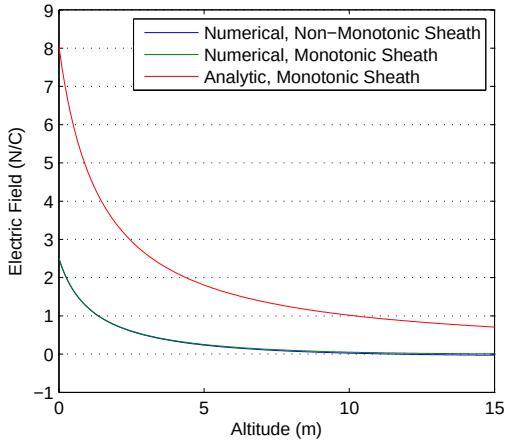

(b) Electric Field

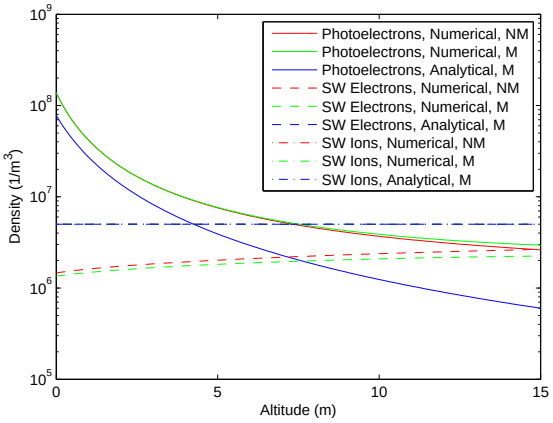

(c) Species Density

Figure 5.1: Comparisons of the three sheath types used in this work, with all parameters calculated at the subsolar point. In Figure 5.1(c), NM is a non-monotonic sheath and M indicates a monotonic sheath.

visible at the resolution of Figure 5.1(c), the density of the solar wind ions for the numerically-described sheath is slightly less than that used in the analytically-described sheath. We can see that there are large differences in the photoelectron densities between the numerically-described and analytically-described sheaths.

We will now discuss the charging currents and electric fields used in each sheath in more detail.

5.2.1 Dust Particle Charging Currents

The form of the charging currents to a charged dust particle vary depending on whether or not the plasma in the sheath is assumed to be thermalized. We assume that the velocity distribution function of the plasma is:

$$f_j(h, \mathbf{v}) = n_{j,k_j} \left(\frac{m_e}{2\pi k_B T_j} \right)^{3/2} \exp\left(-\frac{m_e \mathbf{v}^2}{2k_B T_j} + \frac{e(V(h) - V_{k_j})}{k_B T_j} \right) \tag{5.3}$$

where n_{j,k_j} is the number density of plasma species j at location k_j. The velocity distribution given in Eq. (5.3) only applies to electrons, both of solar wind origin ($j = e$) and photoelectrons ($j = p$). Note that the photoelectron current here is due to the interaction of photoelectrons in the plasma sheath with the dust particle and not due to the direct photoemission of the dust particle (which will be discussed later). $k_e = \infty$ and $k_p = 0$ because these are the two boundary conditions of the plasma flow. m_e is the mass of an electron, V is the potential of the plasma sheath at an altitude h above the surface, and V_{k_j} is the electric potential at location k_j. Note that $V_\infty = 0$, since the solar wind plasma is assumed to be quasi-neutral. T_j is the temperature (in K) of the plasma species. The current to a dust particle can be calculated using the velocity distribution by considering the flux of plasma species to the dust particle:

$$I_j(h) = -e \iiint_{L_v} v \sigma_e(v) f_j(h, \mathbf{v}) \, \mathrm{d}\mathbf{v} \tag{5.4}$$

where σ_e is the electron collisional cross section given by $\sigma_e(v) = \pi r_d^2 (1 + 2eU/(m_e v^2))$. e is the charge of an electron, r_d is the radius of the dust particle (assumed to be spherical) and U is the potential of the dust particle. The dust particle potential is related to its charge by $Q = 4\pi\epsilon_0 r_d U$, where ϵ_0 is the vacuum permittivity. Since the velocity distribution is isotropic and symmetric about the $\hat{h}$ axis, we can express Eq. (5.4) in spherical coordinates. Additionally, we make the substitution $s = v/t_j$, where $t_j = (2k_B T_j/m_e)^{1/2}$, which gives:

$$I_j = -2\pi e \int_{s_a}^{s_b} \int_{\phi_a}^{\phi_b} f_j(h, s) \sigma_e(s) s^3 \sin(\phi) \, \mathrm{d}\phi \mathrm{d}s \tag{5.5}$$

ϕ is the angle between the plasma particle velocity vector and the negative of the surface normal.

Previous studies of dust motion on Eros [13, 28] assume that the plasma is thermalized when calculating the currents to the dust particles. Thus, for the analytically-described sheath, we will use the currents given for the thermalized plasma. For the thermalized plasma, we can integrate Eq. (5.5) with the following limits: $s_a = 0$, $s_b = \infty$, $\phi_a = 0$, and $\phi_b = \pi/2$. The currents flowing to a positively charged dust particle are [25, 28]:

$$I_e = \pi r_d^2 e n_e \sqrt{\frac{8k_B T_e}{\pi m_e}} \left(1 + \frac{eU}{k_B T_e}\right) \tag{5.6}$$

$$I_p = \pi r_d^2 e n_p \sqrt{\frac{8k_B T_p}{\pi m_e}} \left(1 + \frac{eU}{k_B T_p}\right) \tag{5.7}$$

The currents experienced by negatively charged particles are [25, 28]:

$$I_e = \pi r_d^2 e n_e \sqrt{\frac{8k_B T_e}{\pi m_e}} \exp\left(\frac{eU}{k_B T_e}\right) \tag{5.8}$$

$$I_p = \pi r_d^2 e n_p \sqrt{\frac{8k_B T_p}{\pi m_e}} \exp\left(\frac{eU}{k_B T_p}\right) \tag{5.9}$$

For the unthermalized case, we will separate the current into "free" and "captured" parts as described by Nitter *et al.* [38]. "Free" plasma particles are those electrons that either hit the surface or escape to infinity. "Captured" electrons are reflected by a potential barrier in the plasma sheath. Note that the "captured" electron current consists of "two equal parts, moving in opposite directions"[38] because they are trapped in a potential well. There will not be any captured electrons if the plasma is fully thermalized because all possible species velocities are represented. For a numerically-described monotonic sheath in an unthermalized plasma, solar wind electrons will not be captured because they will be accelerated towards the surface. However, in the numerically-described monotonic sheath, photoelectrons will also be attracted towards the surface, resulting in their capture if they are not energetic enough to escape the sheath. Similarly, in non-monotonic sheaths, there will only be captured photoelectrons at altitudes below the potential minimum. Above the potential minimum, there will only be captured solar wind electrons because they will

be accelerated away from the surface in this region. The free and captured currents are given by:

$$I_{j,free} = -2\pi e t_j^4 \int_{s_1}^{\infty} \int_0^{\phi_m} f_j(h,s)\sigma_e(s)s^3 \sin(\phi)\, \mathrm{d}\phi \mathrm{d}s \tag{5.10}$$

$$I_{j,capt} = -4\pi e t_j^4 \left[\int_{s_1}^{\infty} \int_{\phi_m}^{\pi/2} f_j(h,s)\sigma_e(s)s^3 \sin(\phi)\, \mathrm{d}\phi \mathrm{d}s + \int_{s_2}^{s_m} \int_0^{\pi/2} f_j(h,s)\sigma_e(s)s^3 \sin(\phi)\, \mathrm{d}\phi \mathrm{d}s \right] \tag{5.11}$$

For a thermalized plasma, plasma species are assumed to express all possible velocities and incidence angles. However, for the unthermalized plasma, "free" plasma species in the sheath will have a minimum incidence velocity parallel to the h axis. Particles with incidence velocities less than the minimum will be "captured". The minimum incidence velocity is given from conservation of energy, assuming that all the energy of the particle is turned into potential energy either when it reaches some altitude in the sheath or reaches the surface of the dust particle. For a positively charged dust particle, the minimum incidence velocity is given by solving $1/2 m_e v^2 \geq e(V(h) - V_m)$ for v, which gives $s_1 = s_m$ where $s_m = (e(V(h) - V_m)/(k_B T_j))^{1/2}$, where V_m is the minimum potential in the sheath. Similarly, for $U \geq 0$, $s_2 = 0$. The corresponding maximum incidence angle is given by $\phi_m = \arccos(s_m/s)$. If the dust particle is negatively charged ($U < 0$), the electrons will be repelled by the dust particle. Thus, $s_1 = \max(s_m, s_u)$ and $s_2 = \min(s_m, s_u)$, where $s_u = (-eU/(k_B T_j))^{1/2}$. Referring again to Eq. (5.11), we see that the integration limits for the captured current contain the electrons that do not have enough energy to escape the potential well. Integrating gives (from Nitter *et al.*[38]):

$$I_{j,free} = B_j \left[\left(s_1^2 - s_1 s_m + \chi + 1\right) \exp(-s_1^2) - \sqrt{\pi} s_m \left(\chi + 1/2\right) \left(1 - \mathrm{erf}(s_1)\right) \right] \tag{5.12}$$

$$\begin{aligned} I_{j,capt} = {} & 2B_j \left[s_1 s_m \exp(-s_1^2) + (s_2^2 + \chi + 1) \exp(-s_2^2) \right] \\ & + 2B_j \left[-(s_m^2 + \chi + 1) \exp(-s_m^2) + \sqrt{\pi} s_m (\chi + 1/2)(1 - \mathrm{erf}(s_1)) \right] \end{aligned} \tag{5.13}$$

where $B_j = -\pi r_d^2 e n_{j,k_j} \sqrt{2k_B T_j/(\pi m_e)} \exp(s_{k_j})$, where $s_{k_j} = e(V(h) - V_{k_j})/(k_b T_j)$. Also, $\chi = eU/(k_B T_j)$. Note that there will be a different value of s_1, s_m, etc. for the two species considered (photoelectrons and solar wind electrons). Also, from our discussion of the captured electrons, it

is clear that for monotonic sheaths and non-monotonic sheaths at altitudes below the potential minimum, $I_{e,capt} = 0$. Similarly, for the non-monotonic sheath at altitudes above the potential minimum, $I_{p,capt} = 0$.

In our investigation of the thermalized plasma, the current to the dust particles due to the solar wind ions is neglected because the dust particle is assumed to be charged positively. However, in the unthermalized plasma the ion current is considered. Thus, the current due to solar wind ions in the unthermalized sheath is:

$$I_i = e n_{i,\infty} v_{i,\infty} \sigma_i \tag{5.14}$$

where $n_{i,\infty}$ is the number density of ions in the undisturbed solar wind, $v_{i,\infty}$ is the velocity of ions in the solar wind ($v_{i,\infty} = M\sqrt{k_B T_e/m_i}$), and σ_i is the collision cross section of the ions, given by:

$$\sigma_i = \pi r_d^2 \left(1 - \frac{2Y_d}{\alpha M^2 - 2Y(h)}\right) \tag{5.15}$$

Y_d is the nondimensional potential of the dust particle ($Y_d = eU/(k_B T_p)$), $\alpha = T_e/T_p$, M is the ratio of the ion velocity to the Bohm velocity, and $Y(h)$ is the nondimensional potential of the plasma at altitude h. If $Y_d > \alpha M^2/2 - Y$, then the ion does not have enough energy to overcome the potential barrier caused by the charged dust particle, thus causing the ion current to go to zero.

The current due to photoemission is important for both the thermalized and unthermalized plasma sheaths. The photoemission current for positively charged dust particles is:

$$I_{p,d} = \pi r_d^2 \frac{J_0}{d} \exp(-Y_d) \tag{5.16}$$

where J_0 is the photoemission current density (taken to be 4.5×10^{-6} A/m^{-2} [38]) and d is the distance of the body from the sun in astronomical units (assumed to be unity for this work). The photoemission current for negatively charged dust particles is given by:

$$I_{p,d} = \pi r_d^2 \frac{J_0}{d} \tag{5.17}$$

We have expressions for all the currents to the dust particles for both the thermalized and unthermalized sheaths. The time rate of change of charge on the dust particle is given by Eq. (5.18)

for the unthermalized sheath and Eq. (5.19) for the thermalized sheath. Note that the current in the thermalized sheath cover the full range of species velocities and thus there will be no "captured" particles. Additionally, the solar wind ion current is neglected in the thermalized sheath description.

$$\dot{Q}_d = I_i + I_{e,free} + I_{p,free} + I_{e,capt} + I_{p,capt} + I_{p,d} \tag{5.18}$$

$$\dot{Q}_d = I_{p,d} - I_e - I_p \tag{5.19}$$

5.2.2 Electric Field

The electric field varies with altitude above the surface. The electric field is related to the number density of the plasma species through Poisson's equation. We present three solutions to Poisson's equation that have been used in previous studies of dust motion by Nitter *et al.* [38] and Colwell *et al.* [13, 28]. In the form presented by Nitter *et al.*, all of the plasma species (solar wind ions, solar wind electrons, and photoemitted electrons) are considered in the solution of Poisson's equation. For this formulation, there is no analytic expression for the variation of the electric field with altitude. Colwell's work uses a description of the electric field given by Grard and Tunaley [20] that assumes that the number density variation of solar wind species is negligible and Poisson's equation can be solved only considering the number density of photoelectrons, resulting in an analytical description of the altitude variation of the electric field.

5.2.3 Numerically-Described Sheath

Here we will review the derivation of the plasma sheath equations given by Nitter *et al.* [38] for an unthermalized plasma sheath. We begin with the distribution function given in Eq. (5.3). As discussed previously, some of the electron population will be "captured", meaning that it will be trapped at some altitude range in the sheath either unable to escape (photoelectrons) or unable to reach the surface (solar wind electrons). Thus, for a monotonic sheath, some photoelectrons may not have enough energy to escape the sheath due to the potential variation. Photoelectrons in a non-monotonic sheath could also experience this behavior if they do not have enough energy to

reach an altitude above the potential minimum. In a non-monotonic sheath, solar wind electrons are also said to be captured if they do not have enough energy to reach the altitude of the potential minimum. Note that captured electron populations consist of two equal parts moving in opposite directions.

In order to get expressions for the number density of each population, we integrate the velocity distribution function over the range of relevant velocities. Since the "free" particles are able to reach the altitude of the potential minimum, we can determine the minimum velocity of these particles through energy conservation: $v_m(h) = \sqrt{2e(V(h) - V_m)/m_e}$. Thus, the number density of the "free" electron population is:

$$\begin{aligned} n_{j,free} &= \int_{v_m(h)}^{\infty} \int_{-\infty}^{\infty} \int_{-\infty}^{\infty} f_j \, \mathrm{d}\mathbf{v} \\ &= \frac{n_{j,k_j}}{2} \exp\left(\frac{e(V(h) - V_{k_j})}{k_B T_j}\right) \left[1 - \operatorname{erf}\left(\sqrt{\frac{e(V(h) - V_m)}{k_B T_j}}\right)\right] \end{aligned} \tag{5.20}$$

The "captured" electron population is given by:

$$\begin{aligned} n_{j,capt} &= 2 \int_{0}^{v_m(h)} \int_{-\infty}^{\infty} \int_{-\infty}^{\infty} f_j \, \mathrm{d}\mathbf{v} \\ &= n_{j,k_j} \exp\left(\frac{e(V(h) - V_{k_j})}{k_B T_j}\right) \operatorname{erf}\left(\sqrt{\frac{e(V(h) - V_m)}{k_B T_j}}\right) \end{aligned} \tag{5.21}$$

Note $k_e = \infty$ and $k_p = 0$.

Using energy and mass conservation, we can solve for the number density of the ions:

$$n_i = n_{i,\infty} \left(1 - \frac{2Y}{M_x^2 \alpha}\right)^{-1/2} \tag{5.22}$$

where $Y = eV/(k_B T_p)$, $\alpha = T_e/T_p$, $M_x = M\cos(\theta)$ where θ is the solar incidence angle measured from the vertical. Additionally, $M = v_{i,\infty}/v_B$, where $v_B = \sqrt{k_B T_e/m_i}$ is the Bohm velocity and m_i is the mass of an ion.

Additionally, the number density of photoelectrons at the surface is given by [38]:

$$n_{p,0} = \frac{J_0 \cos(\theta)}{d^2 e} \sqrt{\frac{2\pi m_e}{k_B T_p}} \tag{5.23}$$

where $J_0 = 4.5 \times 10^{-6}\text{A/m}^2$ [38], d is the distance from the sun in AU (assumed to be unity for this work), and θ is the solar incidence angle measured from the vertical.

Given these expressions of the number density of the plasma species, we can form Poisson's equation:

$$\frac{\mathrm{d}^2 V}{\mathrm{d}h^2} = \frac{-e}{\epsilon_0}\left(n_i - n_{e,free} - n_{p,free} - n_{e,capt} - n_{p,capt}\right) \tag{5.24}$$

ϵ_0 is the vacuum permittivity. Additionally, we define the Debye length: $\lambda = \sqrt{\epsilon_0 k_B T_p/(ne^2)}$, where $n = n_{p,0} + n_{e,\infty}/\alpha$. This definition of the total density preserves the traditional definitions of the Debye length in the cases where $n_{e,\infty} \gg n_{p,0}$ and $n_{p,0} \gg n_{e,\infty}$ [38].

We now express Poisson's equation in terms of the nondimensional potential Y. Next we use the relationship:

$$\frac{\mathrm{d}^2 Y}{\mathrm{d}h^2} = \frac{1}{2}\frac{\mathrm{d}}{\mathrm{d}Y}\left(\left(\frac{\mathrm{d}Y}{\mathrm{d}h}\right)^2\right) \tag{5.25}$$

Integrating and requiring that the electric field at the potential minimum is zero ($\mathrm{d}Y(h_m)/\mathrm{d}h = 0$) gives:

$$\left(\frac{\mathrm{d}Y}{\mathrm{d}h}\right)^2 = \lambda^2\left(F_i + F_{e,free} + F_{p,free} + F_{e,capt} + F_{p,capt}\right) \tag{5.26}$$

where the contributions from the plasma species are given by:

$$F_i = \frac{2n_{i,\infty}}{n}\alpha M_x^2\left[\sqrt{1 - \frac{2Y}{\alpha M_x^2}} - \sqrt{1 - \frac{2Y_m}{\alpha M_x^2}}\right] \tag{5.27}$$

$$\begin{aligned} F_{j,free} = &\frac{l_j n_{j,k_j}}{n}\left[\exp\left(\frac{Y - Y_{k_j}}{l_j}\right)\left(1 - \operatorname{erf}\left(\sqrt{\frac{Y - Y_m}{l_j}}\right)\right)\right] \\ &+ \frac{l_j n_{j,k_j}}{n}\left[\exp\left(\frac{Y_m - Y_{k_j}}{l_j}\right)\left(2\sqrt{\frac{Y - Y_m}{\pi l_j}} - 1\right)\right] \end{aligned} \tag{5.28}$$

$$\begin{aligned} F_{j,capt} = &\frac{2l_j n_{j,k_j}}{n}\left[\exp\left(\frac{Y - Y_{k_j}}{l_j}\right)\operatorname{erf}\left(\sqrt{\frac{Y - Y_m}{l_j}}\right)\right] \\ &- \frac{4l_j n_{j,k_j}}{\sqrt{\pi} n}\left[\exp\left(\frac{Y_m - Y_{k_j}}{l_j}\right)\sqrt{\frac{Y - Y_m}{l_j}}\right] \end{aligned} \tag{5.29}$$

Recall, Y_m is the nondimensional potential minimum for the given plasma sheath. $l_e = \alpha$ and $l_p = 1$. Additionally, as noted with the discussion of the currents for the unthermalized sheath, there will be no captured solar wind electrons for the monotonic sheath or for the non-monotonic

sheaths at altitudes below the potential minimum. For the non-monotonic sheath, there are no captured photoelectrons at altitudes above the potential minimum. It is assumed that the following quantities are given: T_p, the photoelectron temperature; α, the ratio of the solar wind electron and photoelectron temperature; θ, the solar incidence angle measured from the vertical; M, the ratio of the ion velocity in the solar wind to the ion acoustic velocity; $n_{i,\infty}$, the number density of ions in the solar wind; and d, the distance of the body from the sun in AU. The values of these parameters used in this work are given in Table 5.1. When solving for the potential profile, $M_x = \max(1, M\cos(\theta))$. The remaining unknowns are: $n_{e,\infty}$, the solar wind electron density at infinity; Y_0, the nondimensional potential at the surface; and Y_m, the nondimensional potential minimum. There are three constraints that we can exploit to solve for these variables: the solar wind is assumed to be neutral ($V(h=\infty)=0$), there is no electric field in the solar wind ($E(h=\infty)=0$), and there is no net current to the body (since the body is assumed to be in electrostatic equilibrium). In order to enforce the neutrality of the solar wind, we simply solve $n_{e,free} + n_{e,capt} + n_{p,free} + n_{p,capt} = n_i$ at $h=\infty$, using the species density distributions given in Eq. (5.20)-Eq. (5.22). The resulting constraint is:

$$n_{p,0}\exp(-Y_0)\left(1-\operatorname{erf}\left(\sqrt{-Y_m}\right)\right) + n_{e,\infty}\left(1+\operatorname{erf}\left(\sqrt{-Y_m/\alpha}\right)\right) - 2n_{i,\infty} = 0 \tag{5.30}$$

Requiring that the electric field is zero at infinity is equivalent to $\mathrm{d}Y/\mathrm{d}h = 0$. Solving gives:

$$\begin{aligned} &n_{p,0}\exp(-Y_0)\left[1-\operatorname{erf}\left(\sqrt{-Y_m}\right) - \left(1-2\sqrt{\frac{-Y_m}{\pi}}\right)\exp(Y_m)\right] \\ &+ n_{e,\infty}\alpha\left[1+\operatorname{erf}\left(\sqrt{\frac{-Y_m}{\alpha}}\right) - \left(1+2\sqrt{\frac{-Y_m}{\pi\alpha}}\right)\exp\left(\frac{Y_m}{\alpha}\right)\right] \\ &+ 2n_{i,\infty}\alpha M_x^2\left[1-\sqrt{1-\frac{2Y_m}{\alpha M_x^2}}\right] = 0 \end{aligned} \tag{5.31}$$

The condition that there is no net current to the body can be expressed by requiring the flux per

Table 5.1: Plasma parameters for the simulations of unthermalized plasma sheath.

Parameter	Value
Photoelectron Temperature (T_p)	1.47 eV
Solar Wind Electron Temperature (T_e)	15 eV
Solar Incidence Angle (θ)	0°
Ion Velocity Ratio (M)	10
Ion Number Density ($n_{i,\infty}$)	5000000 m^{-3}
Heliocentric Distance (d)	1 AU

unit area at the surface and infinity to sum to zero:

$$\begin{aligned}&\int_{v_m(0)}^{\infty}\int_{-\infty}^{\infty}\int_{-\infty}^{\infty} v_x f_p(0,\mathbf{v})\,\mathrm{d}\mathbf{v}\\ &+\int_{-\infty}^{-v_m(\infty)}\int_{-\infty}^{\infty}\int_{-\infty}^{\infty} v_x f_e(\infty,\mathbf{v})\,\mathrm{d}\mathbf{v}\\ &-n_{i,\infty}v_{i,\infty}\cos(\theta)=0\end{aligned} \tag{5.32}$$

where $v_m(h)=\sqrt{2e(V(h)-V_m)/m_e}$. Recall that $V(\infty)=0$. Integrating Eq. (5.32) gives:

$$n_{p,0}\exp(Y_m-Y_0)-n_{e,\infty}\sqrt{\alpha}\exp\left(\frac{Y_m}{\alpha}\right)+n_{i,\infty}\sqrt{\frac{2\pi\alpha m_e}{m_i}}M_x=0 \tag{5.33}$$

After solving these three equations simultaneously for $n_{e,\infty}$, Y_0, and Y_m, it is possible to numerically integrate Eq. (5.26) to get the potential variation as a function of height. Note during integration that $\mathrm{d}Y/\mathrm{d}h<0$ if $h<h_m$ and $\mathrm{d}Y/\mathrm{d}h>0$ if $h>h_m$. For monotonic sheaths, $\mathrm{d}Y/\mathrm{d}h<0$ for all altitudes. Once the potential variation in the sheath has been solved, it is possible to solve for the current flowing to a charged dust particle moving through the sheath.

After numerically integrating the nondimensional potential (Y), it is possible to solve for the electric field since, by definition, $E=-\mathrm{d}V/\mathrm{d}h$. Using this definition and solving for the dimensional quantity E gives:

$$E=\frac{-k_BT_p}{e}\frac{\mathrm{d}Y}{\mathrm{d}h} \tag{5.34}$$

5.2.4 Analytically-Described Sheath

The description of the photoelectron density and electric field used by Hughes *et al.* [28] and Colwell *et al.* is based on the development by Grard and Tunaley [20]. It should be noted

that Grard and Tunaley's development assumes that the solar wind plasma is not modified by its interaction with the body's surface. This simplification allows them to analytically solve for the potential profile, which otherwise must be solved by numerically integrating the potential as a function of altitude as is discussed in Section 5.2.3. Additionally, the potential profile is assumed to be monotonically decreasing. We begin by defining the photoelectron velocity distribution as twice the standard 1D Maxwellian velocity distribution:

$$f(v_0) = \sqrt{\frac{2k_B T_p}{m_e \pi}} \exp\left(\frac{-m_e v_0^2}{2k_B T_P}\right) \tag{5.35}$$

The velocity distribution used is *twice* the standard 1D Maxwellian velocity distribution because the velocities are only positive (i.e., photoelectrons are only emitted from the plate) and thus a factor of two is required in order for the integral of the probability distribution function to be equal to one ($\int_0^\infty f(v_0) = 1$). From continuity and conservation of energy, we can see that the number density at a particular velocity is:

$$n = \frac{n_0 v_0}{\left(v_0^2 - (2e/m_e)(V_0 - V(h))\right)^{1/2}} \tag{5.36}$$

Using the definition given in Eq. (5.36), the number density of photoelectrons is:

$$n_p = n_{p,0} \int_b^\infty \frac{v_0 f(v_0) \mathrm{d}v_0}{\left(v_0^2 - (2e/m_e)(V_0 - V)\right)^{1/2}} \tag{5.37}$$

where $b = [2e/m_e(V_0 - V(h))]^{1/2}$, which is the minimum velocity that photoelectrons must have at the surface in order to reach the altitude where the potential is V(h). Poisson's equation and the definition of the electric field ($E = -\mathrm{d}V/\mathrm{d}h$) give:

$$\frac{\mathrm{d}^2 V}{\mathrm{d}h^2} = \frac{1}{2}\frac{\mathrm{d}(E^2)}{\mathrm{d}V} = \frac{n_p e}{\epsilon_0} \tag{5.38}$$

Substituting our definition for the photoelectron density distribution (Eq. (5.37)) gives:

$$E^2 = \frac{2m_e n_{p,0}}{\epsilon_0} \int_b^\infty \left[v_0^2 - \frac{2e}{m_e}(V_0 - V(h))\right]^{1/2} v_0 f(v_0)\, \mathrm{d}v_0 \tag{5.39}$$

$$E = \sqrt{\frac{m_e n_{p,0}}{\epsilon_0 v_e}} \frac{\exp\left(\frac{-Ae}{m_e}(V_0 - V(h))\right)}{2^{1/4} A^{3/4}} \tag{5.40}$$

where $A = m_e/(2k_B T_p)$ and $v_e = \sqrt{k_B T_p/m_e}$. Note that a monotonically decreasing photoelectron sheath is assumed here. Thus, we know that $E > 0$. Since $E = -\mathrm{d}V/\mathrm{d}h$, we can integrate Eq. (5.40) and apply the condition that $V(h = 0) = V_0$ to solve for the potential variation as a function of height:

$$V(h) = V_0 - \frac{m_e}{Ae} \ln\left(\sqrt{\frac{m_e n_{p,0}}{\epsilon_0 v_e}} \left(\frac{A}{2}\right)^{1/4} \frac{eh}{m_e} + 1\right) \tag{5.41}$$

Substituting Eq. (5.41) into Eq. (5.40) gives an analytical description of the electric field as a function of altitude (h). If we solve Eq. (5.39) for the electric field at the surface, we get:

$$E_0 = v_e \sqrt{\frac{2mn_{p,0}}{\epsilon_0}} \tag{5.42}$$

Thus, Grard and Tunaley [20] give the following compact description of the electric field as a function of altitude:

$$E = \frac{E_0}{1 + \frac{h}{\sqrt{2}\lambda}} \tag{5.43}$$

where the Debye length is given by $\lambda = \sqrt{\epsilon_0 k_B T_p/(e^2 n_{p,0})}$. Similarly, we can solve for the altitude variation in the photoelectron density:

$$n_p = \frac{n_{p,0}}{\left(1 + \frac{h}{\sqrt{2}\lambda}\right)^2} \tag{5.44}$$

The solar wind electron density and photoelectron emission flux are given by Eq. (5.45) (units: m^{-3}) and Eq. (5.46) (units: electrons $\mathrm{m}^{-2}\ \mathrm{s}^{-1}$), where d is the distance from the Sun in AU. Note that $I_{ph0}e = J_0$ that is used in the numerically defined sheath.

$$n_e = \frac{5 \times 10^6}{d^2} \tag{5.45}$$

$$I_{ph0} = \frac{2.8 \times 10^{13}}{d^2} \tag{5.46}$$

The flux of photoelectrons on the surface gives the number density of photoelectrons at zero altitude (see Eq. (5.47)). The flux is multiplied by a factor of two to take into account the equal

Table 5.2: Electrostatic parameters for a particle launch at high noon from the equator.

Parameter	Value
Characteristic Electron Speed (ν_{pe})	719092 m/s
Photoelectron Number Density ($n_{p,0}$)	77.876 cm^{-3}
Debye Length (λ_D)	1.021 m
Electric Field Strength (E_0)	8.0588 N/C

number of photoelectrons moving towards and away from the surface.

$$n_{p,0} = \frac{2I_{ph0}\cos\theta}{\nu_{pe}} \tag{5.47}$$

$$\nu_{pe0} = \sqrt{\frac{2k_BT_p}{m_e}} \tag{5.48}$$

where θ is the solar incidence angle measured from the vertical, ν_{pe} is the characteristic photoelectron speed from conservation of energy and $n_{p,0}$ is the photoelectron density at the surface.

Through conservation of energy, $m_e v_e^2/2 - eV_0 = 0$ (the potential and kinetic energy of the dust particle at infinity is zero) and Grard's derivation, we can solve for the surface electric field as a function of the equilibrium surface potential (ϕ_s):

$$E_0 = \frac{2\sqrt{2}\phi_s}{\lambda_D} \tag{5.49}$$

The surface potential is calculated numerically by solving Eq. (5.52) for ϕ_s. For this work, motion was assumed to occur at the subsolar point (i.e., $\theta = 0°$). Some characteristics of the plasma environment at this location are given in Table 5.2. Note that for this development, the plasma sheath does not depend on the central body's distance from the sun because both n_e and I_{ph0} are proportional to d^{-2}.

$$I_e = n_e\sqrt{\frac{k_BT_e}{2\pi m_e}}\left(1 + \frac{e\phi_s}{k_BT_e}\right) \tag{5.50}$$

$$I_p = I_{ph0}\exp\left(\frac{-e\phi_s}{k_BT_p}\right)\cos\theta \tag{5.51}$$

$$I_{sw} - I_{ph} = 0 \tag{5.52}$$

5.3 Equilibria

The equilibria of both the numerically and analytically-described sheaths are of interest because they give indications of where dust particles are likely to levitate. Two equilibria have been identified for a specific particle size near the surface of the Moon [42]. We will identify equilibria for a range of particles sizes, central body masses and three sheath models. In order to locate the equilibrium state of the levitating particle, it is necessary to set $\ddot{h} = \dot{Q}_d = 0$ and solve:

$$\frac{Q_d E}{m_d} - \frac{g_s}{\left(\frac{h}{r_c} + 1\right)^2} = 0 \tag{5.53}$$

$$\sum I = 0 \tag{5.54}$$

5.3.1 Numerically-Described Sheath

In order to locate the equilibria, we begin by solving for the equilibrium dust particle potential over a range of altitudes of interest by calculating the current to a particle with a specified size, altitude, and charge (recall $Q_d = 4\pi\epsilon_0 r_d U$, where U is the dust particle's electric potential). Using Newton-Raphson's method to change the dust particle's charge, we iterate until the current flowing to the particle is approximately zero, satisfying Eq. (5.54) at a range of altitudes. It is now possible to iteratively solve for the altitude where Eq. (5.53) is satisfied, again using Newton-Raphson's method. The resulting equilibria for the Moon, Eros and Itokawa calculated at the subsolar point ($\theta = 0°$) for the monotonic and non-monotonic sheaths are shown in Figure 5.2 and Figure 5.3, respectively. The stability of the equilibria are indicated with varying point markers and will be discussed in more detail in Section 5.4.

The most apparent difference between the equilibria plots for the monotonic and non-monotonic sheaths is that the stable equilibria are not shown to extend down to small particle sizes for the monotonic sheath. Note that this 'cut-off' is due to the numerical nature of our calculations. Eventually, for the monotonic sheath, the plasma potential becomes very close to zero, at which point the electric field must be set to zero. Thus, in reality the stable equilibria exist for small particle

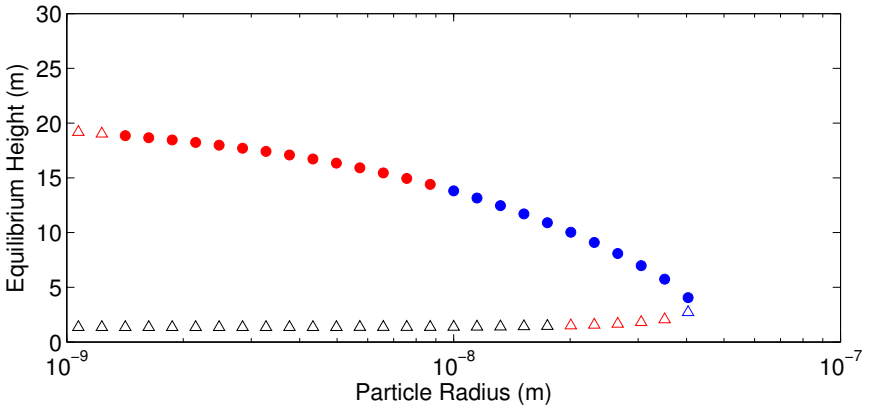

(a) Moon

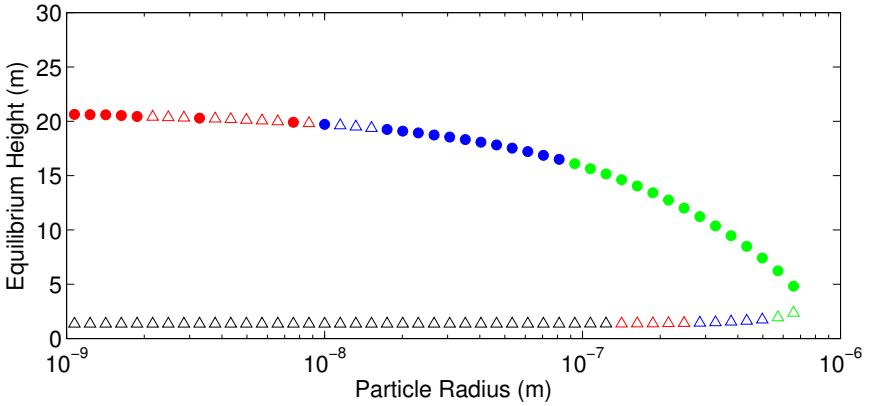

(b) Eros

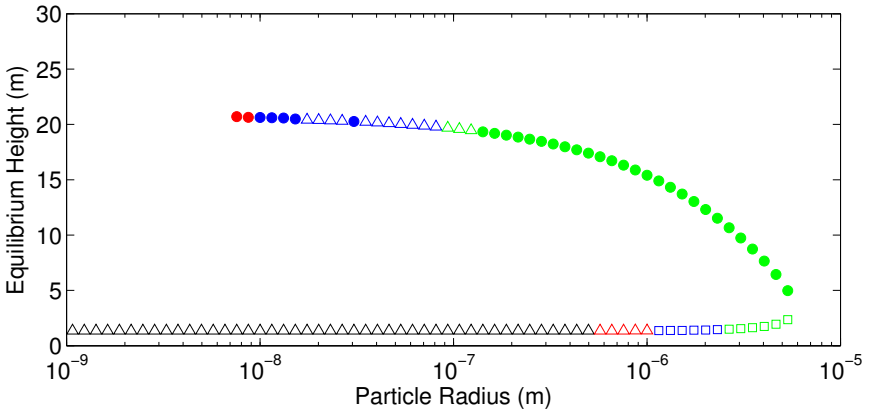

(c) Itokawa

Figure 5.2: Equilibrium heights for various particle radii and central bodies using the monotonic numerically described sheath. Solid circular points show the stable equilibria. The other points are unstable and the location of their eigenvalues will be discussed in Section 5.4. Points are colored according to the number of electrons of the equilibrium charge: $[0, 1)e$, black; $[1, 10)e$, red; $[10, 100)e$, blue; $\geq 100e$, green.

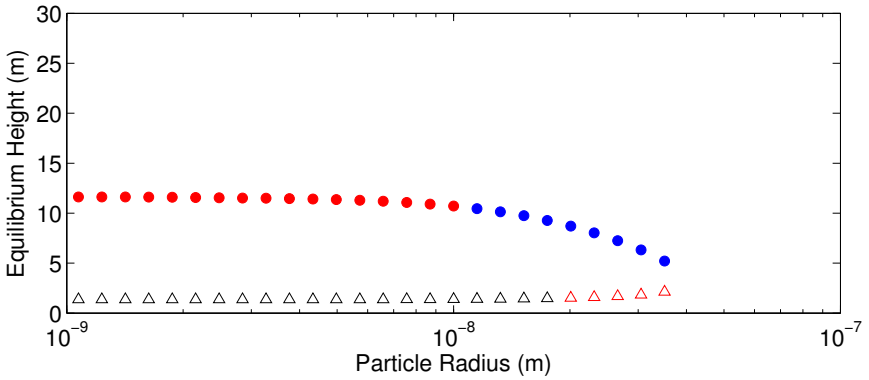

(a) Moon

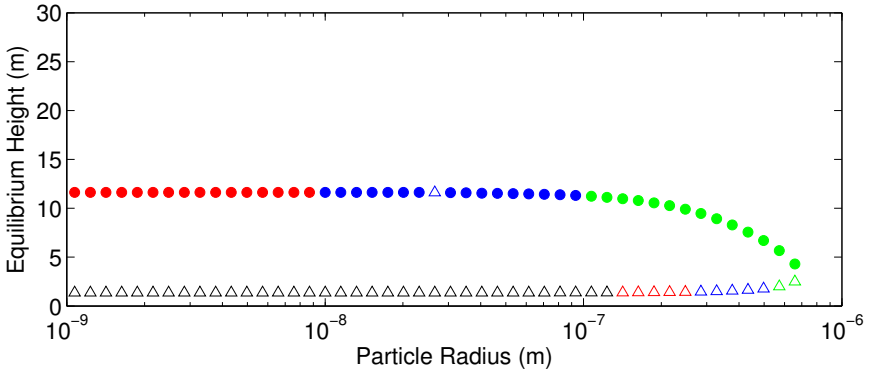

(b) Eros

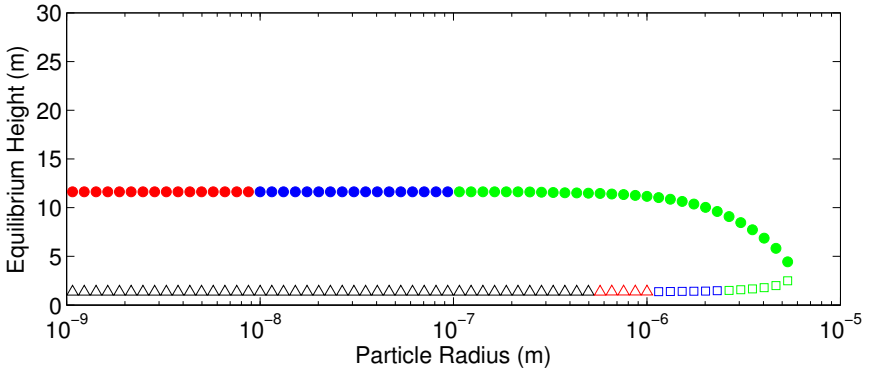

(c) Itokawa

Figure 5.3: Equilibrium heights for various particle radii and central bodies using the non-monotonic numerically described sheath. Solid circular points show the stable equilibria. The other points are unstable and the location of their eigenvalues will be discussed in Section 5.4. Points are colored according to the number of electrons of the equilibrium charge: $[0, 1)e$, black; $[1, 10)e$, red; $[10, 100)e$, blue; $\geq 100e$, green.

sizes, although at these equilibria the equilibrium charge is likely to be less than one electron, meaning that a dust particle could never reach this equilibrium state.

In Figure 5.2 and Figure 5.3, the number of electrons in the equilibrium charge is indicated by the color of the points. It can be seen that as the size of the particle increases, the equilibrium charge increases. Additionally, the effects of the discretized nature of charging will be negligible when propagating the trajectories of particles that have a large charge ($> 10e^-$). Note that the equilibria charges of the lower, unstable equilibria are lower than those of the stable equilibria for a given particle size. A weaker charge at lower altitudes is expected because the electric field strength will be larger at lower altitudes. The equilibrium charge for the dust particles appears to be relatively similar for a given particle size between the monotonic and non-monotonic sheaths.

The altitudes of the equilibria are relatively similar for the monotonic and non-monotonic sheaths. The equilibria altitudes are lower for the non-monotonic sheath because they cannot be higher than the altitude of the potential minimum, since the equilibrium dust potential is positive for altitudes above the potential minimum.

In order to make our results independent of grain shape, we plot the equilibria for the non-monotonic sheath (shown in Figure 5.3) as a function of charge to surface weight ratio in Figure 5.4. Note that when plotted in this form, the three curves for the different bodies in Figure 5.3 collapse to a single curve. Thus, Figure 5.4 allows us to generalize our analysis to non-spherical grains, assuming that the equilibrium charge of the particle is not influenced by its asphericity. The small amount of scatter that can be observed in Figure 5.4 is due to the significance of the radial gravity variation for the smaller bodies: the charge is divided by the weight of the particle at the surface.

5.3.2 Analytically-Described Sheath

As expected, locating the equilibria in the analytically-described sheath is much easier than in the numerically-described sheath. We can solve Eq. (5.53) (using the definition in Eq. (5.1)) for the equilibrium charge (Q_d) as a function of the particle height, since we have an analytical

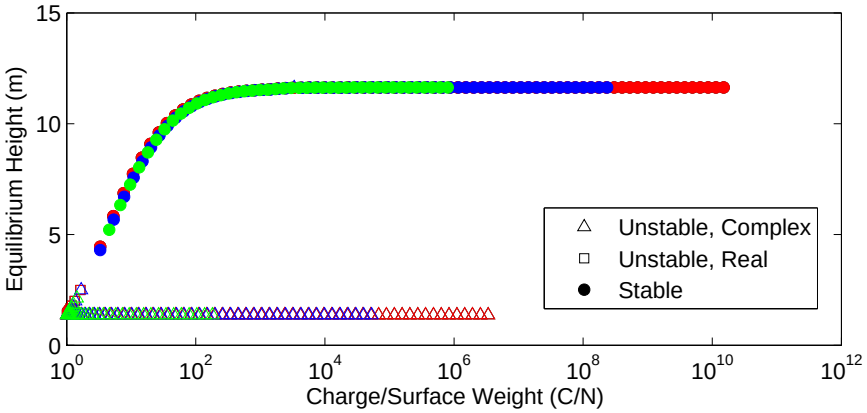

Figure 5.4: Altitude equilibria for the non-monotonic sheath as a function of charge per surface weight, allowing generalization to non-spherical dust grains. Green: Moon, Blue: Eros, Red: Itokawa.

description of the electric field:

$$Q_{d,eq} = \frac{m_d \mu \left(\sqrt{2}\lambda_D + h\right)}{\sqrt{2}\lambda_D E_0 \left(h + r_c\right)^2} \tag{5.55}$$

where the gravitational parameter μ is used ($\mu = g_s r_c^2$). In order to exactly solve Eq. (5.54), we must calculate $\dot{Q}_d$ for a range of altitudes and then interpolate to locate the equilibrium height. The resulting equilibrium heights for a given particle size and central body are shown in Figure 5.5. Figure 5.5 shows that for a given particle radius, there exists either one or three equilibrium altitudes, in contrast to the results for the numerically-described sheath. We note that the stable equilibria occur only along the portions of the curves with negative slope. A more detailed discussion linear and nonlinear stability of the equilibria shown in Figure 5.5 will be given in subsequent sections.

By making several approximations, it is possible to develop analytical descriptions of the equilibrium height curves shown in Figure 5.5 for equilibrium heights larger than the Debye length. Recall that a particle must be positively charged in order to levitate on the day side of the bodies considered. The current flowing to a positively charged particle from interaction with the electrons in the photoelectron sheath (I_p, see Eq. (5.7)) is proportional to $\left(1 + h/(\sqrt{2}\lambda_D)\right)^{-2}$. By assuming that the equilibrium height of interest is much larger than the Debye length, we can neglect the

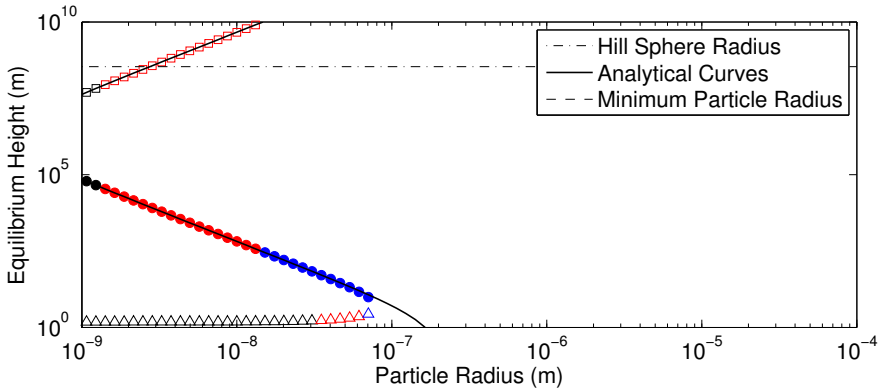

(a) Moon

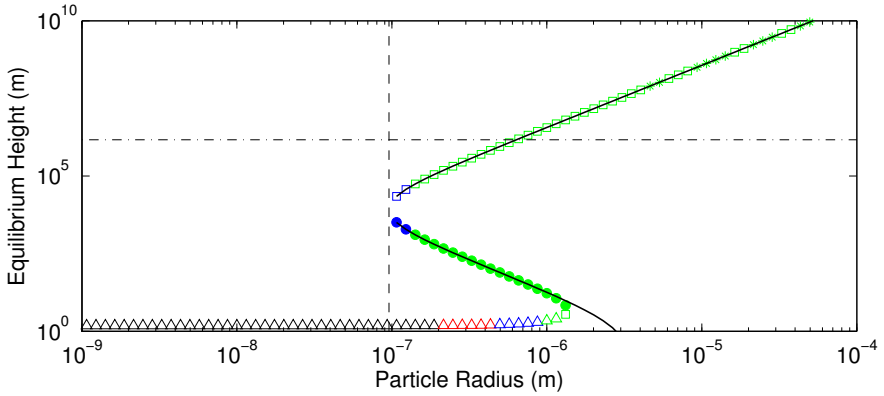

(b) Eros

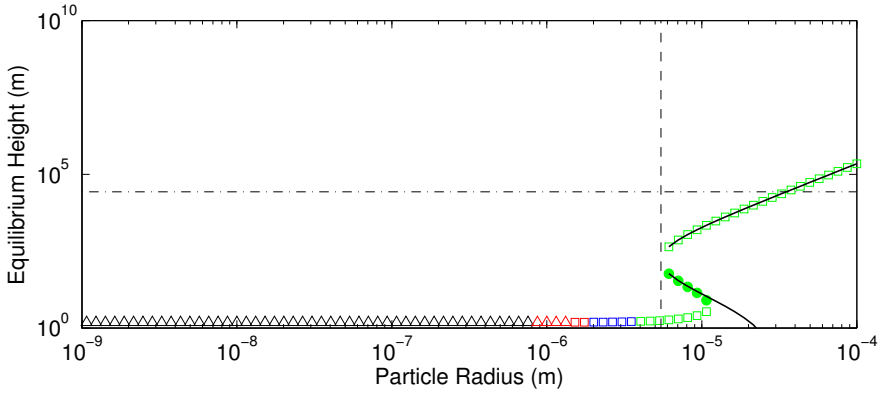

(c) Itokawa

Figure 5.5: Equilibrium heights for various particle radii and central bodies. Solid circular points show the stable equilibria. The other points are unstable and the location of their eigenvalues will be discussed in Section 5.4. Solid lines give the analytical approximation of the stable equilibria and upper unstable equilibria. Dashed lines show the analytical minimum particle size capable of stable levitation and the altitude above which particles are considered to escape (Hill Sphere radius).

photoelectron current (I_p). Additionally, we assume $eU/(k_B T_e) \ll 1$, which allows us to approximate the solar wind electron current by Eq. (5.8) instead of Eq. (5.6). With these assumptions, Eq. (5.54) becomes:

$$\pi r_d^2 e I_{ph0} \exp\left(\frac{-eU_{d,eq,an}}{k_B T_p}\right) - \pi r_d^2 e n_p \sqrt{\frac{8k_B T_p}{\pi m_e}} \exp\left(\frac{eU_{d,eq,an}}{k_B T_p}\right) = 0 \tag{5.56}$$

This equation is analytically solvable for the equilibrium particle potential ($U_{d,eq,an}$) and charge ($Q_{d,eq,an}$).

$$Q_{d,eq,an} = \frac{4\pi\epsilon_0 r_d}{A+B} \ln\left(\frac{I_{ph0}}{n_e}\sqrt{\frac{\pi m_e}{8k_B T_e}}\right) \tag{5.57}$$

$$A = \frac{e}{k_B T_p} \tag{5.58}$$

$$B = \frac{e}{k_B T_e} \tag{5.59}$$

We can then solve Eq. (5.53) (which takes the form of a quadratic equation) for the equilibrium height:

$$h_{eq,an} = \frac{m_d g_s r_c^2}{2\sqrt{2} Q_{d,eq,an} E_0 \lambda_D} - r_c \pm \sqrt{\left(r_c - \frac{m_d g_s r_c^2}{2\sqrt{2}\lambda_D Q_{d,eq,an} E_0}\right)^2 - r_c^2 + \frac{m_d g_s r_c^2}{Q_{d,eq,an} E_0}} \tag{5.60}$$

Taking the negative sign for the third term in Eq. (5.60) gives an approximation for the negative slope region of the curve in Figure 5.5 (i.e. the stable equilibria). Taking the positive sign gives an approximation for the upper positive slope region of the equilibrium height curve. Both curves are plotted on top of the numerically calculated equilibria in Figure 5.5 and it can be seen that they closely approximate the numerical results except when the equilibrium height approaches the Debye length. The decay of this approximation for low equilibrium altitudes is expected since the derivation assumes $h \gg \lambda_D$.

It is possible to approximate the size of the smallest particle that can be stably levitated for a given central body for the analytically-described sheath. At this lower stable levitation limit, the equilibrium height becomes complex. We thus solve Eq. (5.60) for the particle size that causes the

third term in Eq. (5.60) to be complex. Particle sizes satisfying the condition in Eq. (5.61) will not have a stable equilibrium state. The minimum particle size capable of stable levitation (given by Eq. (5.61)) is plotted in Figure 5.5 with vertical lines.

$$r_{d,ust} \leq \left[\frac{24 E_0 \lambda_D^2 \epsilon_0}{(A+B)\rho g_s r_c^2} \left(\frac{r_c}{\sqrt{2}\lambda_D} - 1 \right) \ln \left(\frac{I_{ph0}}{n_e} \sqrt{\frac{\pi m_e}{8 k_B T_e}} \right) \right]^{1/2} \tag{5.61}$$

There are several significant differences in the equilibria identified using the numerically-described sheath and the analytically-described sheath. First of all, the altitude of the stable equilibria are orders of magnitude higher in the analytically-described sheath than those identified in the numerically-described sheaths. The electric field at low altitudes is much larger for the analytically-described sheath than the electric fields of numerically-described sheaths. Conversely, the equilibrium dust potential is smaller for the analytical sheath than the numerically-described sheaths. The discrepancy between the electric fields is larger than that of the equilibrium dust potentials. Thus, the required electrostatic force for levitation will occur at higher altitudes for the analytical sheath than the numerically-described sheath.

The second major difference is the presence of high altitude unstable equilibria in the analytically-described sheath. The upper unstable equilibria likely exist because the gravity has weakened more quickly than the electric field. Upper unstable equilibria do not exist in the monotonic numerically-described sheath because the electric field goes to zero at much lower altitudes. High altitude unstable equilibria could not exist in the non-monotonic sheath because the electric field points towards the surface at altitudes above the potential minimum. Thus any particles that would be levitated above this altitude would require the dust particle's equilibrium charge to be negative, which will not happen because the current due to photoemission dominates the charging of the dust. The presence of the high altitude unstable equilibria dictates that there will exist a minimum particle size where stable equilibria exist for the analytically-described sheath. Although there is no clear minimum particle size that can experience stable levitation in the numerically-described sheath, low equilibria charging levels effectively limit the equilibria states that could actually be reached by levitating particles.

The maximum particle size that is capable of stable levitation is similar in all three sample sheaths used.

5.4 Linear Stability Analysis

It is expected that any *in situ* population of levitating dust particles will be observed near the stable equilibria. Dust particles that approach unstable equilibria will either escape the body's gravitation, reimpact or approach the stable equilibria. We linearize the system and define:

$$Q_d = Q_d^* + \delta Q_d \tag{5.62}$$

$$h = h^* + \delta h \tag{5.63}$$

where, h^* is the equilibrium height and Q_d^* is the equilibrium charge. Next, define $G = \ddot{h}$ (Eq. (5.1)) and $H = \dot{Q}_d$ (Eq. (5.2)). The linearized equations of motion of the system are thus:

$$\ddot{h} = \ddot{h}^* + \frac{\partial G}{\partial Q_d}\delta Q_d + \frac{\partial G}{\partial h}\delta h + H.O.T. \tag{5.64}$$

$$\dot{Q}_d = \dot{Q}_d^* + \frac{\partial H}{\partial Q_d}\delta Q_d + \frac{\partial H}{\partial h}\delta h + H.O.T. \tag{5.65}$$

The higher order terms are neglected. Note that at the equilibrium state:

$$\ddot{h}^* = 0 \tag{5.66}$$

$$\dot{Q}_d^* = 0 \tag{5.67}$$

Thus, we define the linearized system as:

$$\begin{bmatrix} \delta\dot{Q}_d \\ \delta\dot{h} \\ \delta\ddot{h} \end{bmatrix} = A \begin{bmatrix} \delta Q_d \\ \delta h \\ \delta\dot{h} \end{bmatrix} \tag{5.68}$$

$$A = \begin{bmatrix} H_Q & H_h & 0 \\ 0 & 0 & 1 \\ G_Q & G_h & 0 \end{bmatrix} \tag{5.69}$$

where the notation $H_Q = \partial H/\partial Q_d$ is used to simplify the expression and the partials are evaluated at the equilibrium state. The partials of the numerically-defined system are as follows:

$$\frac{\partial H}{\partial Q_d} = \frac{\partial I_i}{\partial Q_d} + \frac{\partial I_{e,free}}{\partial Q_d} + \frac{\partial I_{p,free}}{\partial Q_d} + \frac{\partial I_{e,capt}}{\partial Q_d} + \frac{\partial I_{p,capt}}{\partial Q_d} + \frac{\partial I_{p,d}}{\partial Q_d} \tag{5.70}$$

$$\frac{\partial H}{\partial h} = \frac{\partial I_i}{\partial h} + \frac{\partial I_{e,free}}{\partial h} + \frac{\partial I_{p,free}}{\partial h} + \frac{\partial I_{e,capt}}{\partial h} + \frac{\partial I_{p,capt}}{\partial h} + \frac{\partial I_{p,d}}{\partial h} \tag{5.71}$$

$$\frac{\partial G}{\partial Q_d} = \frac{E}{m_d} \tag{5.72}$$

$$\frac{\partial G}{\partial h} = \frac{2\mu}{(r_c + h)^3} + \frac{Q_d}{m_d}\frac{\mathrm{d}E}{\mathrm{d}h} \tag{5.73}$$

The partials with respect to the charge of the dust particle are:

$$\frac{\partial I_i}{\partial Q_d} = \frac{-2e^2 n_{i,\infty} v_{i,\infty} \pi r_d^2}{4\pi\epsilon_0 r_d k_B T_p \left(\alpha M^2 - 2Y\right)} \tag{5.74}$$

$$\begin{aligned}\frac{\partial I_{j,free}}{\partial Q_d} = {} & B_j \left(2s_1 \frac{\partial s_1}{\partial Q_d} - s_m \frac{\partial s_1}{\partial Q_d} + \frac{\partial \chi}{\partial Q_d}\right) \exp\left(-s_1^2\right) \\ & - 2s_1 B_j \left(s_1^2 - s_1 s_m + \chi + 1\right) \frac{\partial s_1}{\partial Q_d} \exp\left(-s_1^2\right) \\ & - B_j \sqrt{\pi} s_m \frac{\partial \chi}{\partial Q_d} \left(1 - \operatorname{erf}\left(s_1\right)\right) \\ & + 2B_j s_m \left(\chi + \frac{1}{2}\right) \exp\left(-s_1^2\right) \frac{\partial s_1}{\partial Q_d}\end{aligned} \tag{5.75}$$

$$\begin{aligned}\frac{\partial I_{j,capt}}{\partial Q_d} = {} & 2B_j \left[\left(1 - 2s_1^2\right) s_m \exp\left(-s_1^2\right) \frac{\partial s_1}{\partial Q_d} - \frac{\partial \chi}{\partial Q_d} \exp\left(-s_m^2\right)\right] \\ & + 2B_j \exp\left(-s_2^2\right) \left[2s_2 \frac{\partial s_2}{\partial Q_d} + \frac{\partial \chi}{\partial Q_d} - 2s_2 \left(s_2^2 + \chi + 1\right)\right] \\ & + 2B_j \sqrt{\pi} s_m \left[\frac{\partial \chi}{\partial Q_d} \left(1 - \operatorname{erf}\left(s_1\right)\right) - \left(\chi + \frac{1}{2}\right) \left(\frac{2}{\sqrt{\pi}} \exp\left(-s_1^2\right)\right) \frac{\partial s_1}{\partial Q_d}\right]\end{aligned} \tag{5.76}$$

Note that $\partial s_m/\partial Q_d = 0$ and $\partial B_j/\partial Q_d = 0$. If $Q_d < 0$, $\partial I_{p,d}/\partial Q_d = 0$. If the dust particle is positively charged, then:

$$\frac{\partial I_{p,d}}{\partial Q_d} = -\frac{r_d J_0 e}{4\epsilon_0 k_B T_p d^2} \exp\left(\frac{-eQ_d}{4\pi\epsilon_0 r_d k_B T_p}\right) \tag{5.77}$$

The partials with respect to the altitude of the dust particle are:

$$\frac{\partial I_i}{\partial h} = -\frac{4Y_d e n_{i,\infty} v_{i,\infty} \pi r_d^2}{\left(\alpha M^2 - 2Y\right)^2} \frac{\mathrm{d}Y}{\mathrm{d}h} \tag{5.78}$$

$$\begin{aligned}\frac{\partial I_{j,free}}{\partial h} &= \frac{\partial B_j}{\partial h}\left[\left(s_1^2 - s_1 s_m + \chi + 1\right)\exp\left(-s_1^2\right) - \sqrt{\pi} s_m \left(\chi + \frac{1}{2}\right)\left(1 - \operatorname{erf}\left(s_1\right)\right)\right] \\ &+ B_j\left(2s_1\frac{\partial s_1}{\partial h} - s_m\frac{\partial s_1}{\partial h} - s_1\frac{\partial s_m}{\partial h}\right)\exp\left(-s_1^2\right) \\ &- 2s_1 B_j\left(s_1^2 - s_1 s_m + \chi + 1\right)\frac{\partial s_1}{\partial h}\exp\left(-s_1^2\right) \\ &- B_j\sqrt{\pi}\frac{\partial s_m}{\partial h}\left(\chi + \frac{1}{2}\right)\left(1 - \operatorname{erf}\left(s_1\right)\right) \\ &+ 2B_j s_m\left(\chi + \frac{1}{2}\right)\exp\left(-s_1^2\right)\frac{\partial s_1}{\partial h}\end{aligned} \tag{5.79}$$

$$\begin{aligned}\frac{\partial I_{j,capt}}{\partial h} &= 2\frac{\partial B_j}{\partial h}\left[s_1 s_m \exp(-s_1^2) + (s_2^2 + \chi + 1)\exp(-s_2^2)\right] \\ &+ 2\frac{\partial B_j}{\partial h}\left[-(s_m^2 + \chi + 1)\exp(-s_m^2) + \sqrt{\pi} s_m(\chi + 1/2)(1 - \operatorname{erf}(s_1))\right] \\ &+ 2B_j\exp\left(-s_1^2\right)\left[\left(s_m - 2s_1^2 s_m\right)\frac{\partial s_1}{\partial h} + \frac{\partial s_m}{\partial h}s_1\right] \\ &- 4B_j s_2\frac{\partial s_2}{\partial h}\exp\left(-s_2^2\right)\left(s_2^2 + \chi\right) + 2s_m\frac{\partial s_m}{\partial h}\exp\left(-s_m^2\right)\left(s_m^2 + \chi\right) \\ &+ 2B_j\sqrt{\pi}\left(\chi + \frac{1}{2}\right)\left[\left(1 - \operatorname{erf}\left(s_1\right)\right)\frac{\partial s_m}{\partial h} - \frac{2s_m}{\sqrt{\pi}}\frac{\partial s_1}{\partial h}\exp\left(-s_1^2\right)\right]\end{aligned} \tag{5.80}$$

where $\mathrm{d}Y/\mathrm{d}h$ is defined in Eq. (5.26) and $\partial\chi/\partial h = 0$. Additionally, $\partial I_{p,d}/\partial h = 0$, since the photoemission is only dependent on the dust particle's charge. Recall that certain "captured" species currents (and their derivatives) are equal to zero depending on the altitude and sheath type.

The partials of the analytically defined system are given as follows:

$$\begin{aligned}&\frac{\partial F}{\partial Q_d} = -\frac{r_d q_e}{4\epsilon_0}\times \\ &\left[\frac{I_{ph0}}{k_B T_{pe}}\exp\left(\frac{-q_e Q_d}{4\pi r_d \epsilon_0 k_B T_{pe}}\right) + \frac{n_{sw}}{k_B T_{sw}}\sqrt{\frac{8k_B T_{sw}}{\pi m_e}} + \frac{N_{pe0}}{k_B T_{pe}\left(1 + \frac{h}{\sqrt{2}\lambda_{D0}}\right)^2}\sqrt{\frac{8k_B T_{pe}}{\pi m_e}}\right]\end{aligned} \tag{5.81}$$

$$\frac{\partial F}{\partial h} = -\pi r_d^2 q_e N_{pe0} \sqrt{\frac{8 k_B T_{pe}}{\pi m_e}} \left(1 + \frac{q_e Q_d}{4\pi r_d \epsilon_0 k_B T_{pe}}\right) \left[-\frac{2}{\sqrt{2}\lambda_{D0}} \left(1 + \frac{h}{\sqrt{2}\lambda_{D0}}\right)^{-3}\right] \tag{5.82}$$

$$\frac{\partial G}{\partial Q_d} = \frac{E_0}{m_d \left(1 + \frac{h}{\sqrt{2}\lambda_{D0}}\right)} \tag{5.83}$$

$$\frac{\partial G}{\partial h} = -\frac{Q_d E_0}{m_d \sqrt{2}\lambda_{D0} \left(1 + \frac{h}{\sqrt{2}\lambda_{D0}}\right)^2} + \frac{2 g_s}{\left(\frac{h}{r_c} + 1\right)^3 r_c} \tag{5.84}$$

Having calculated the partials, we can now solve for the eigenvalues and eigenvectors of the A matrix (Eq. (5.69)). The eigenvalues are the solutions to:

$$x^3 - H_Q x^2 - G_h x + H_Q G_h - H_h G_q = 0 \tag{5.85}$$

Stable eigenvalues have negative real parts while unstable eigenvalues have positive real parts. The eigenvalues are also related to oscillation frequency and damping rate of the trajectories about the equilibria.

In Figure 5.2, Figure 5.3, and Figure 5.5, the characteristics of the eigenvalues of the equilibria are indicated by the style of point marker used. Figure 5.6 gives a pictorial representation of the eigenvalue configurations observed and the corresponding marker used in Figure 5.2, Figure 5.3, and Figure 5.5. Note that for many of the equilibria, the motion is damped. For the Moon and Eros for both of the numerically-described sheaths, we can see that the real root moves to the left (i.e., from Figure 5.6(b) to Figure 5.6(a)) as we transition from the curve of the unstable equilibria to the curve of the stable equilibria. For Itokawa, the complex roots collapse to the real axis along the curve of the unstable equilibria (from Figure 5.6(b) to Figure 5.6(d)). Then, as we transition to stable equilibria, the real root in the right half plane moves left and the complex roots reappear (transition from configuration (d) to (a)). It's possible that the three stage stability transition seen for Itokawa occurs for the Moon and Eros as well, yet is not seen due to the coarse particle size grid used in Figure 5.2 and Figure 5.3. For the numerically-described monotonic sheath, the real eigenvalue appears to be very close to zero at small particle sizes, causing the transition from stable to unstable equilibria at the upper altitudes (Figure 5.6(a) to Figure 5.6(b)). The lower, unstable equilibria of the analytically-described sheath are similar to those of the numerically-described sheath. For the analytically-described sheath at the transition from the stable equilibria to the

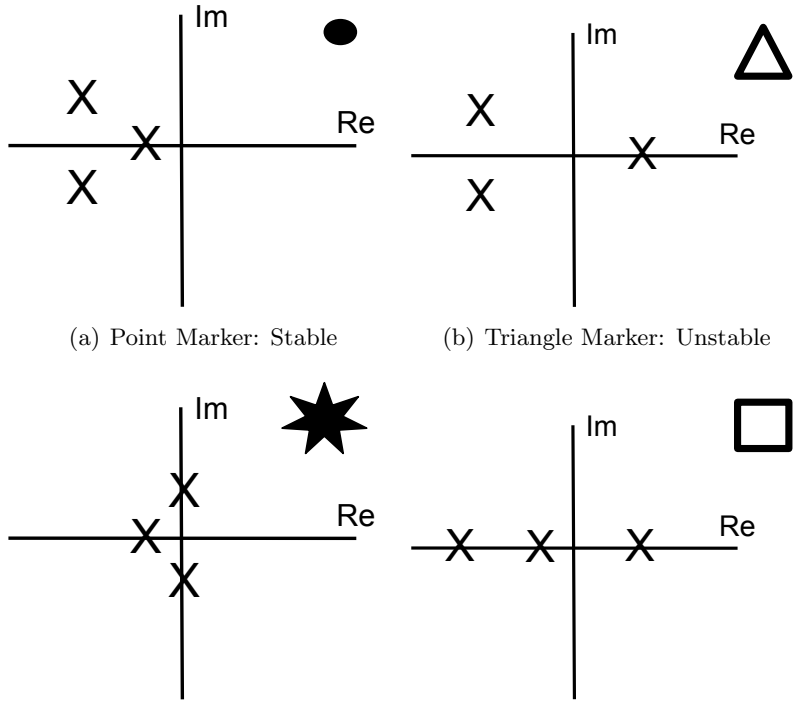

(a) Point Marker: Stable (b) Triangle Marker: Unstable

(c) Star Marker: Unstable (d) Square Marker: Unstable

Figure 5.6: Pictorial representation of the placement of eigenvalues used in Figure 5.2, Figure 5.3, Figure 5.5. The relative placement of the poles is not to scale.

upper unstable equilibria, we see that the complex roots collapse to the real axis and one of the real roots moves to the right half plane (Figure 5.6(a) to Figure 5.6(d)). At large altitudes above the Hill Sphere for Eros, we see the movement of the complex roots to and from the real axis (sometimes seeing purely imaginary roots like in Figure 5.6(c)).

In addition to telling us about the stability of the equilibria, the eigenvalues also give an indication of the time scales involved in the motion of the dust particles. The timescales calculated from the eigenvalues of the stable equilibria indicate the time that a dust particle will take to approach the equilibrium state (characteristic time of the real root) and the period of oscillation (from the complex root) about that state. The characteristic time of the real root and oscillation period of the complex roots for the stable equilibria for the three sheaths are plotted in Figure 5.7. The vertical lines correspond to the particle radii that will be used for the numerical analysis of the trajectories (green: Moon, blue: Eros, red: Itokawa) (see the Section 5.5 for more discussion).

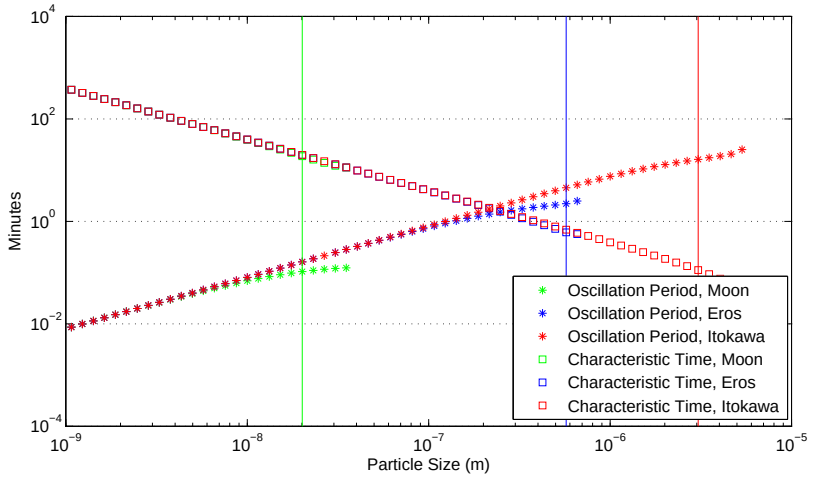

(a) Non-Monotonic Sheath

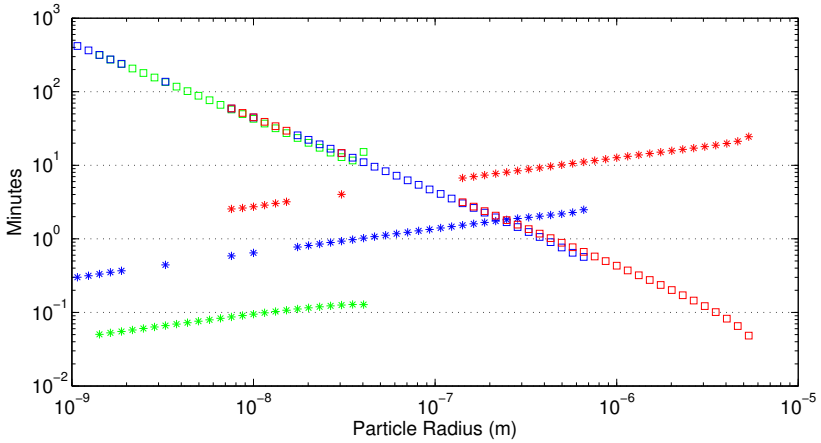

(b) Monotonic Sheath

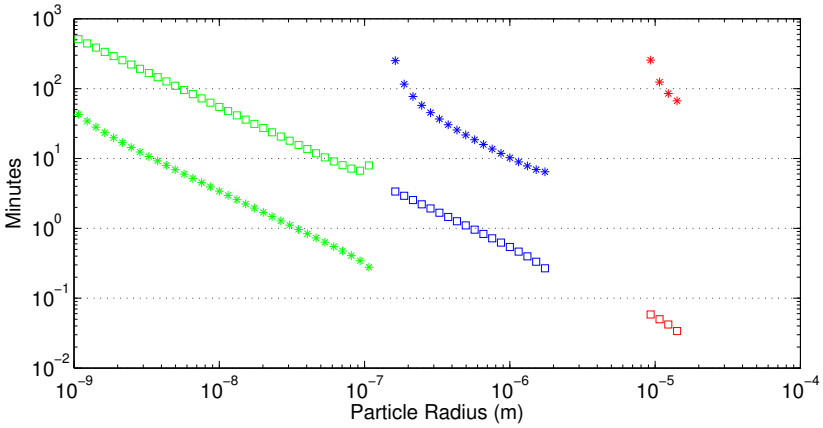

(c) Analytic Sheath

Figure 5.7: The characteristic times and oscillation period for the stable equilibria for the three sheath types. The vertical lines in 5.7(a) indicate the particle sizes used for trajectory simulations on the Moon (green), Eros (blue) and Itokawa (red).

For the three sheaths, we see that the characteristic times of the real root of the stable equilibria are fairly similar. In 5.7(c), there are distinct particle sizes for each central body. The characteristic time of the stable real eigenvalues follow a linear trend, decreasing with increasing particle size.

From Figures 5.7(a), 5.7(b) and 5.7(c), it can be seen that there are significant differences between the oscillation periods of the stable equilibria of the numerically-defined sheaths as compared to the analytically-defined sheath. For the numerically-defined sheaths (Figures 5.7(a) and 5.7(b)), the oscillation period increases with dust particle size, whereas the oscillation period follows the opposite trend for the analytically-described sheath. This deviation can be explained by examining the location of the stable equilibria in the sheath types. For the numerically-calculated sheaths, the altitudes of the equilibria are relatively constant. Small particles (which require a weaker electrostatic force to cancel gravity) will have smaller altitude fluctuations as they move about the stable state (and thus a shorter oscillation period), than larger dust particles. In the analytically-described sheath, the equilibria of smaller particles are at much larger altitudes than those of larger particles. Since the electric field is weaker at high altitudes, the small particles will exhibit large altitude oscillations about their stable equilibrium states, resulting in a longer oscillation period for small particles.

Despite the difference in slope between the numerically-described and analytically-described sheaths, the two monotonic sheaths (Figures 5.7(b) and 5.7(c)) show similar central-body dependent behavior. For the numerically-described monotonic sheath (Figure 5.7(b)), the oscillation period for a given particle size decreases when the mass of the central body increases. This trend is also seen for the analytically-described sheath (which is, of course, monotonic as well). The decrease in oscillation period with the increase in central body mass is expected since smaller altitude oscillations are likely to occur above more massive bodies, thus shortening the oscillation period.

Since only a small amount of energy is dissipated during each oscillation about the equilibrium state, we note that the characteristic time scale of the oscillation decay is much larger (on the order of days) than the approach of the particle to the stable equilibria. We have assumed that the plasma

environment is constant during the particle's motion. In actuality, though, the plasma environment experienced by the dust particle will vary greatly due to the rotation of the central body and the translational motion of the dust particle. The rotation period of the Moon is approximately 27 days. The rotation periods for Eros and Itokawa are 5.27 hours and approximately 12 hours, respectively. Comparing these rotation periods to the time scales shown in Figure 5.7, it can be seen that the approximation of a constant plasma sheath is likely valid for the approach of a dust particle to the equilibrium point (neglecting translational motion of the particle and equilibria where the equilibrium charge is less than one electron). However, it is likely that the structure of the plasma sheath will be significantly altered before the particle's oscillations about the stable equilibrium are significantly damped. The influence of a time varying plasma environment on the equilibria will be discussed in Chapter 6.

5.5 Nonlinear Stability Analysis and Initial Conditions for Levitation

While Figure 5.2, Figure 5.3 and Figure 5.5 give an indication of the stability of dust particles near equilibria, they do not fully characterize state space. The stabilities indicated in Figure 5.2, Figure 5.3 and Figure 5.5 are only valid locally about the equilibria, since the stabilities were calculated using the linearized system. To date, the identification of initial conditions that lead to dust particle levitation has been a tedious, trial and error procedure. From our linearized system analysis, we have identified low altitude unstable equilibria. Perturbing dust particles away from the unstable equilibrium state gives a preliminary map of the states that result in dust particle levitation. Unfortunately, we cannot propagate the perturbed states back towards the surface because the system is not time reversible (the current to the dust particle is dependent only on its height and charge). We can assess the behavior of dust particles near the equilibria by varying the initial conditions of dust particles along the eigenvectors of A (see Eq. (5.69)). Thus, the perturbed state is defined by:

$$\mathbf{X_{pert}} = \mathbf{X^*_{eq}} + C_1\mathbf{V_1} + C_2\mathbf{V_2} + C_3\mathbf{V_3} \tag{5.86}$$

where $\mathbf{X_{pert}}$ is the 3x1 vector of the initial state of the particle that has been perturbed away from the equilibrium state ($\mathbf{X^*_{eq}}$), $\mathbf{V_1}$, $\mathbf{V_2}$ and $\mathbf{V_3}$ are the eigenvectors of the A matrix evaluated at the equilibrium point, and C_1, C_2, and C_3 are randomly generated constants. Recall that the state ($\mathbf{X}$) consists of the particle's altitude, altitude rate and charge. Additionally, the perturbed state $\mathbf{X_{pert}}$ is taken to be the real part of the result given by Eq. (5.86) (the eigenvectors may be complex). The constants of perturbation may be positive or negative real numbers.

The eigenvectors point in the direction of the steepest slope. Thus, varying the initial particle state along the eigenvectors will result in the greatest change in the behavior of the trajectory. However, the eigenvectors change with the state, so large perturbations along the eigenvalues of the equilibrium state may not result in large variations in the final state. Thus, sometimes it is easier to simply manually sweep over a range of initial particle heights and charges in order to fully characterize the behavior of the system. This is the approach used.

5.5.1 Analytically-Defined Sheath

In order to fully understand the behavior of particles in state space, we plot particle trajectories for large perturbations away from their upper and lower unstable equilibria for a 0.57224 micron particle near Eros in Figure 5.8. From Figure 5.8, we see that some particles with positive initial altitude rates and initial altitudes both above and below the lower unstable equilibrium approach the stable equilibrium. As the initial altitude rate is increased further, the particles exhibit ballistic motion. When the initial altitude rate is increased above approximately 10 m/s (specific to this particle size), the particles approach our upper limit on particle altitude (the Hill Sphere) and the particles are assumed to escape. The tendency for particles to oscillate about the stable equilibrium at low initial altitude rates, and exhibit ballistic and escaping behavior at higher initial altitude rates agrees with preliminary work conducted by Colwell *et al.* [13]. Figure 5.8 also shows that some particles launched with negative initial altitude rates from altitudes near the lower unstable equilibrium fall back to the surface. This behavior agrees with our intuition of the problem since a large upwards acceleration (supplied by the electrostatic force) would be required to prevent

particles with a negative initial velocity from impacting the surface. However, it is possible that particles with a very small negative initial velocity could approach the stable equilibrium, but such initial conditions were not used in the creation of Figure 5.8.

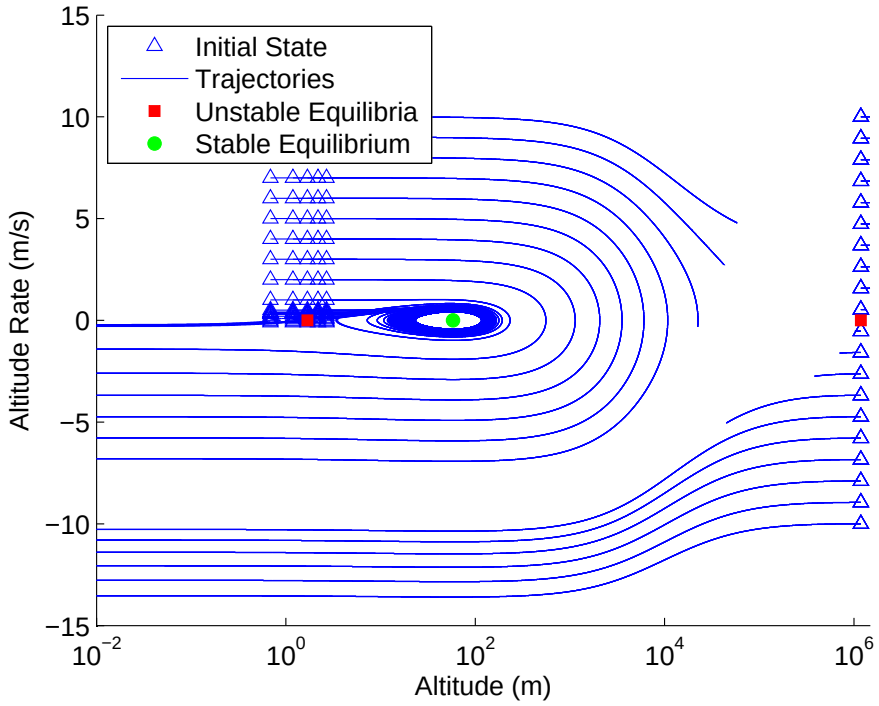

Figure 5.8: Altitude and altitude rate for 0.57224 micron radius particles near Eros for the analytically-defined sheath given initial conditions surrounding the unstable equilibria. Note that particles were considered to escape if they reached the altitude of the Hill Sphere (approximately 1.5×10^6 m).

Particles launched with a positive initial altitude rate at altitudes near the upper unstable equilibrium are assumed to escape since they pass the Hill Sphere altitude propagation limit. Particles launched with a negative initial altitude rate from altitudes near the upper unstable equilibrium state are seen to travel towards the surface and some are seen to impact the surface during the integration time period used. Particles placed near the upper unstable equilibrium will not oscillate about the stable equilibrium state because all of those particles would need to cross the ballistic trajectories before reaching the oscillatory trajectories, which would indicate two possible trajectories for a given state (at the intersection point). Since this is a 3DOF problem, variations

in particle charging could give the appearance of crossing trajectories in the 2D projection shown in Figure 5.8. The initial charge level for the trajectories shown in Figure 5.8 is the equilibrium charge at the unstable equilibrium. Very large deviations in the initial charge could potentially result in different behavior. Additionally, the discretized nature of particle charging is not included in the propagation of these trajectories.

5.5.2 Numerically-Defined Sheaths

In order to map out the states that lead to dust particle levitation, we first vary the initial particle height and altitude rate while setting the initial particle charge to the equilibrium value (results in Figure 5.9 and Figure 5.10). Generally, the state space plots for the non-monotonic and monotonic numerically-described sheaths (Figure 5.9 and Figure 5.10) are very similar. We see that the initial altitude of the particle has little influence on the fate of the dust particle unless the initial velocity is very close to that required for levitation. If the initial altitude rate (or velocity) of the dust particle is very high, particles appear to be on escape trajectories, as expected. Reducing the initial velocity results in ballistic trajectories. Further reducing the initial velocity results in the levitation of particles with initial altitudes at or above the equilibrium initial altitude. Particles with negative initial velocities generally fall to the surface.

Figure 5.11 shows a close-up view of the state space plot for the numerically-described non-monotonic sheath. It can be seen that some trajectories beginning at altitudes above that of the unstable equilibrium with a negative initial velocity approach the unstable equilibrium before being captured by the stable equilibrium. In the close-up plot, we can also more clearly see the ballistic trajectories of particles launched from altitudes below the unstable equilibrium. Additionally, Figure 5.11 shows the decay of trajectories towards the stable equilibrium. Since the oscillations of levitating grains are damped, energy is not conserved. Energy is lost due to the finite charging times of the dust grains. Essentially, the dust grains are not always in charge equilibrium at a given altitude. This method of energy dissipation has been discussed in [35].

Figure 5.12 and Figure 5.13 show the state space plots for particles capable of levitation

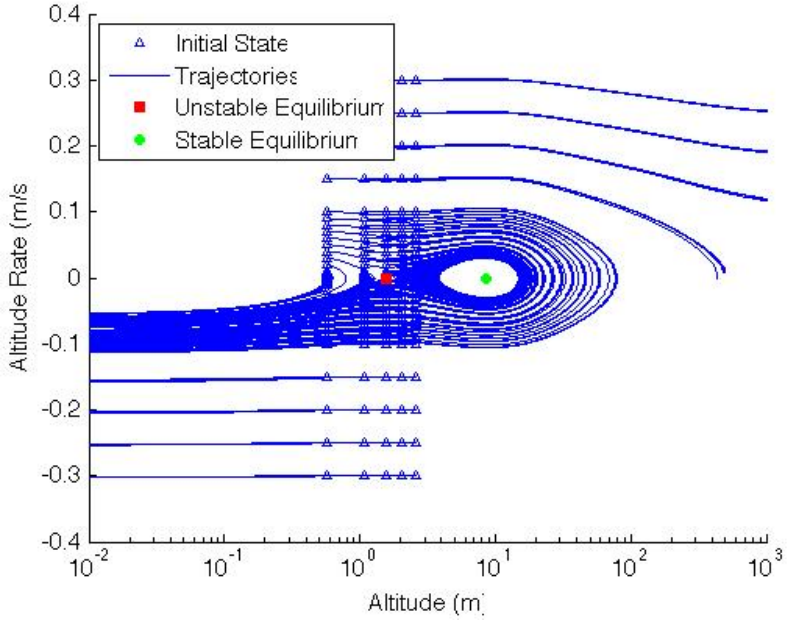

Figure 5.9: Altitude and altitude rate for a 3.05 micron radius particle near Itokawa using the numerically-described non-monotonic sheath.

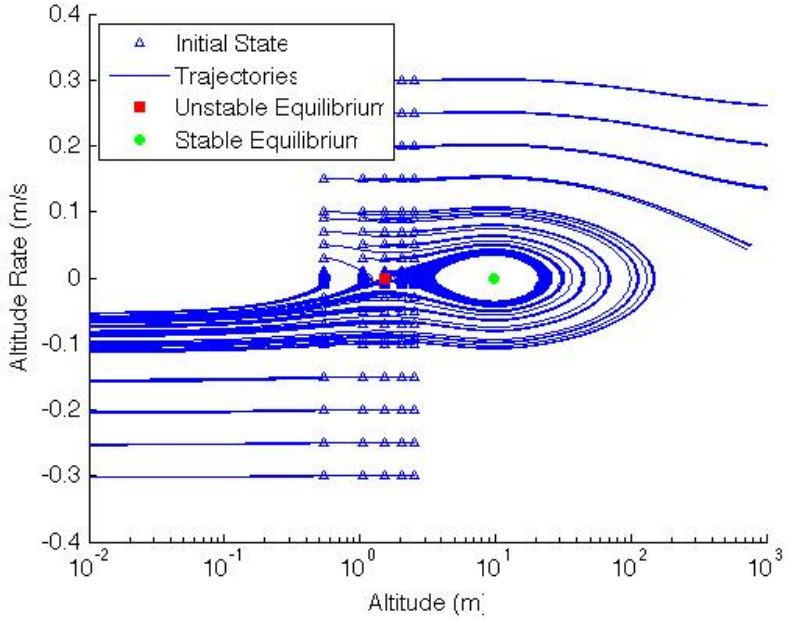

Figure 5.10: Altitude and altitude rate for a 3.05 micron radius particle near Itokawa using the numerically-described monotonic sheath.

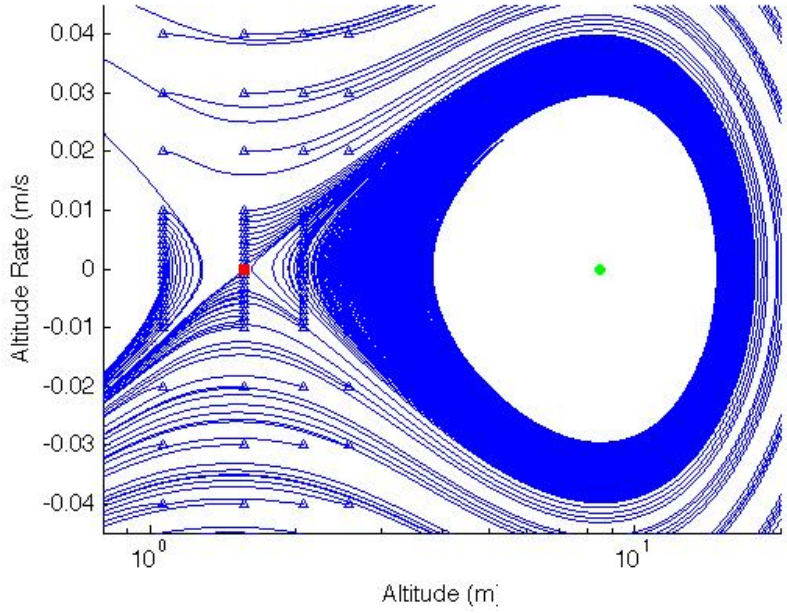

Figure 5.11: Altitude and altitude rate for a 3.05 micron radius particle near Itokawa using the numerically-described non-monotonic sheath.

on Eros and the Moon. Comparing Figure 5.9, Figure 5.12 and Figure 5.13, we see that there are significant differences in the structure of the state space plots as we switch central bodies and particles sizes. The three particle sizes used in the plots were chosen because they are close to the largest particle sizes capable of stable levitation on these bodies. On Itokawa, we see that for some initial conditions, the approximately 3 micron particle experiences slightly damped oscillations about the stable equilibria. However, for the particle near Eros (Figure 5.12), we see that the oscillations are much more quickly damped and the trajectory of the oscillatory particles looks like a spiral. The state space plot of the lunar trajectories (Figure 5.13) is also very different from those of Itokawa and Eros. It can be seen that the trajectories of the dust particles near the lunar surface experience damped oscillations about the *unstable* equilibrium before being ejected onto an oscillatory trajectory to the *stable* equilibrium. Fewer trajectories are shown in Figure 5.13 since the propagation of numerous small oscillations is time-consuming.

The very large differences in the state-space plots for the three bodies can be initially ex-

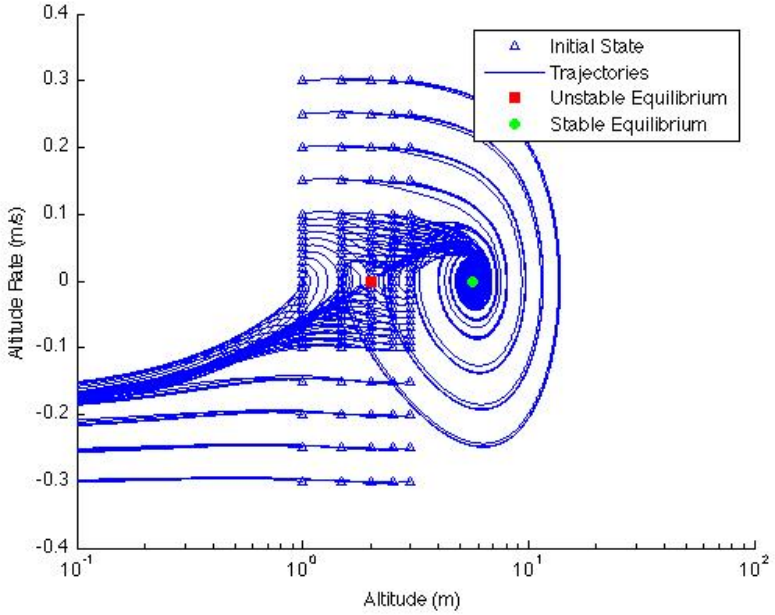

Figure 5.12: Altitude and altitude rate for a 0.57224 micron radius particle near Eros using the numerically-described non-monotonic sheath.

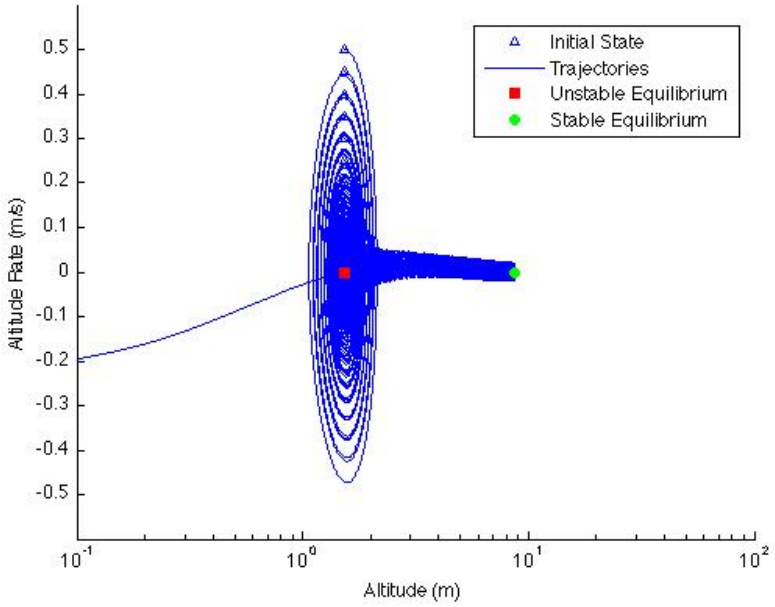

Figure 5.13: Altitude and altitude rate for a 0.0201 micron radius particle near the Moon using the numerically-described non-monotonic sheath.

plained by looking at the characteristic times and oscillation periods of motion about the stable equilibria (see Figure 5.7(a)). The characteristic time is calculated by taking the inverse of the real part of the eigenvalue. The oscillation period is defined as the product of 2π and the inverse of the imaginary part of the eigenvalue. From Figure 5.7(a), we can see that the relative magnitudes of the characteristic time and oscillation period are significantly different for the three bodies considered. (In Figure 5.7(a), the green vertical line indicates the particle size propagated on the Moon, the blue line indicates Eros, and the red line indicates Itokawa). We can see that for the particle size used on Itokawa, the oscillation period is much longer than the characteristic time. This agrees with our observation that the dust particles quickly approach the stable equilibrium and then undergo several oscillations about it. In contrast, the trend is reversed for the Moon: the oscillation period is much shorter than the characteristic time. Again, this agrees with our numerical observations, where we see that a particle undergoes many small oscillations before reaching the stable equilibrium. The values of the characteristic time and oscillation period for the particle size used on Eros are similar.

We can further understand the diverse behavior observed in the state space plots by plotting the characteristic times and oscillation periods for both the stable and unstable equilibria. Figure 5.14 shows the characteristic times of the real and complex roots for the unstable equilibrium, the oscillation period of the unstable equilibrium, the characteristic time of the real root of the stable equilibrium, and the oscillation period of the stable equilibrium for each body. The characteristic time of the complex root of the stable equilibrium is not shown because it is much larger than the other timescales (on the order of days). Again, the characteristic time of a real eigenvalue gives an indication of the time required for the dust particle to approach the equilibrium state. The characteristic time of the complex eigenvalue is the timescale of the damping of the oscillation. From Figure 5.14(c), we see that the shortest timescales are the oscillation periods of the unstable and stable equilibria. The characteristic time of the complex root and the real root of the unstable equilibria are also fairly comparable and shorter than the characteristic time of the stable equilibrium. Thus, by inspecting the eigenvalues alone, we can explain why we see

decaying oscillations about the unstable equilibrium before the trajectories are attracted to the stable equilibrium. Again, the timescales of motion of the particle on Eros are very similar. For Itokawa, we see that the shortest timescales are the characteristic times of the real roots of the stable and unstable equilibria. Thus, the particle approaches the stable equilibria and its motion is subsequently dominated by oscillatory motion with a relatively long period.

In order to test our hypothesis that from the eigenvalues we can predict the general structure of the state-space plots, we have created a second state-space plot for Itokawa using a 0.5722 micron dust particle (the same size of particle used to create the state space plot for Eros). We expect the state space plot for this particle size at Itokawa to be similar to that at Eros because, from inspecting Figures 5.14(a) and 5.14(b), we see that the relative magnitudes of the characteristic times and oscillation periods will be similar. From Figure 5.15, we see that the smaller sized particle does exhibit more spiral-like behavior (which was seen in the Eros state-space plot) than the originally-considered ~ 3 micron particle (Figure 5.9).

It is possible to more clearly identify the initial conditions that lead to dust particle levitation in Figure 5.16. We indicate the 'fate' of particles as a function of the initial conditions by using different marker types. It can be seen in Figure 5.16(a) (which displays the same data as Figure 5.9), that the range of initial velocities leading to dust particle levitation for a ~ 3 micron particle on Itokawa is very small (approximately 1 cm/s). Figure 5.16(a) shows that the range of initial velocities leading to dust particle levitation decreases as the launching altitude approaches the surface. Figure 5.16(b) shows the fate of particles launched from the unstable equilibrium altitude with a range of initial charges. It can be seen that the initial charge does not appear to significantly influence the range of initial velocities that results in dust particle levitation. Variation in initial charge could have a larger effect on the levitation initial conditions of particle sizes whose equilibrium charge is small. In Figure 5.16(b), there is one ballistic trajectory with an initial velocity of zero. This trajectory is the result of a particle initially placed exactly at the unstable equilibrium state.

By simply visually comparing Figure 5.9, Figure 5.12 and Figure 5.13, it can be seen that the

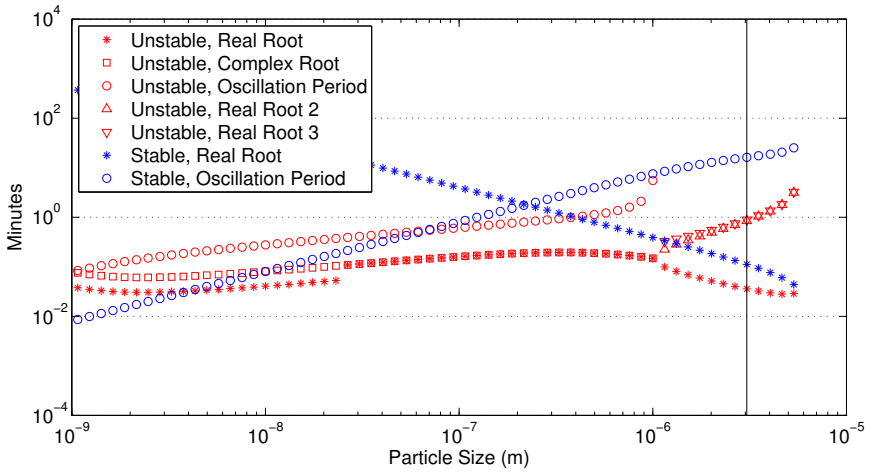

(a) Itokawa

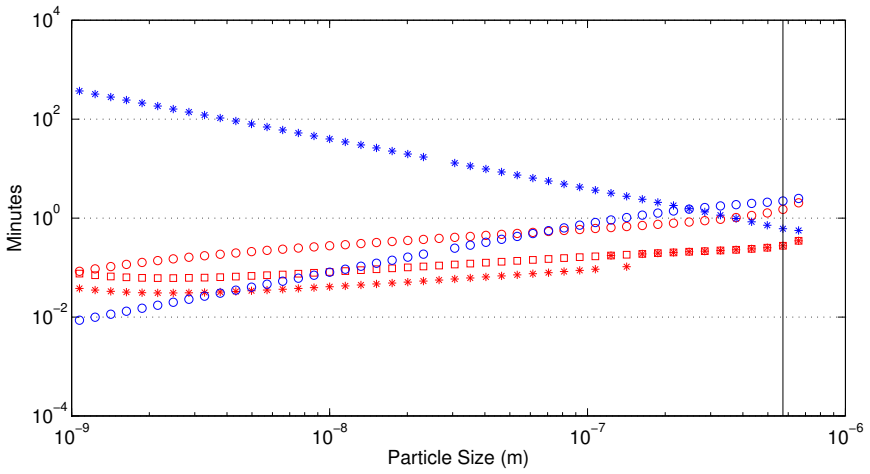

(b) Eros

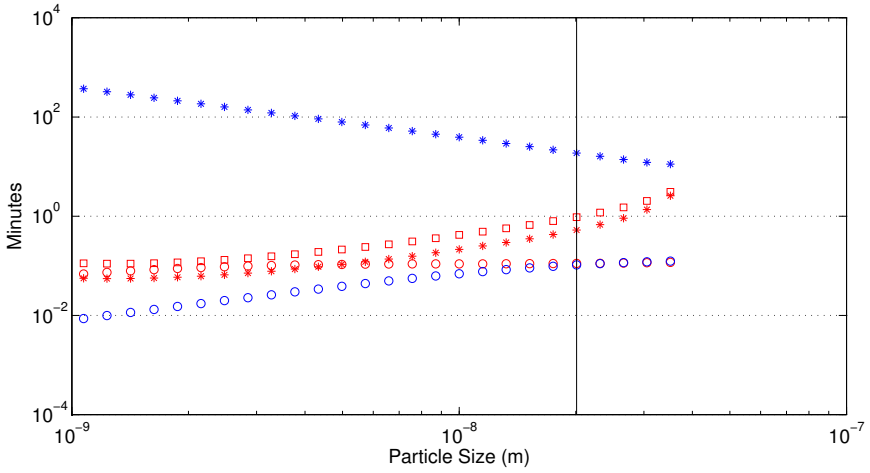

(c) Moon

Figure 5.14: Plots showing the characteristic times and oscillation periods of the unstable and stable equilibria for the three bodies studied using the non-monotonic sheath model. The particle size propagated on each of the bodies is indicated with the vertical black line. Note that for some particle sizes on Itokawa, there are three real roots.

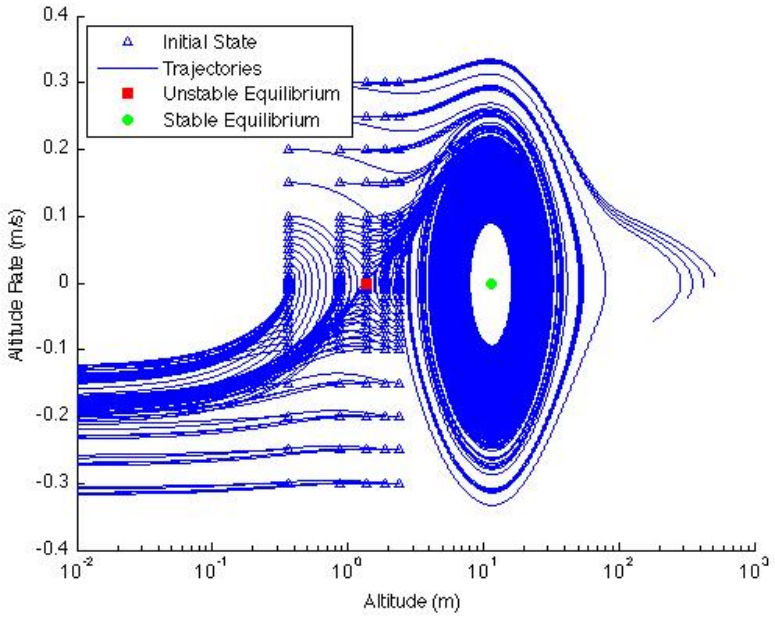

Figure 5.15: Altitude and altitude rate for a 0.57224 micron radius particle near Itokawa using the numerically-described non-monotonic sheath.

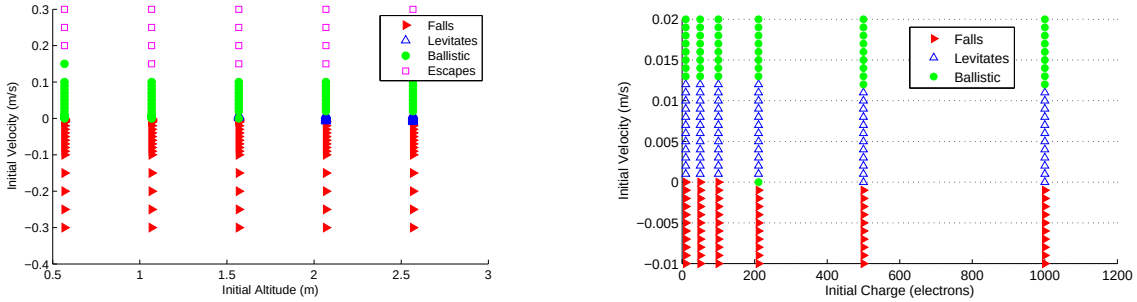

(a) Varied Altitude

(b) Varied Charge

Figure 5.16: Plots showing the fate of a 3.053 micron particle with varying initial conditions in the numerically-calculated non-monotonic sheath above Itokawa. When altitude is varied, the initial particle charge is set to the initial charge of the unstable equilibrium. When charge is varied, the initial altitude is set to the unstable equilibrium altitude. Similar results are seen for the numerically-calculated monotonic sheath.

range of initial velocities that results in dust particle levitation increases dramatically from Itokawa to the Moon, for the particle sizes used. Just as the structure of the state space plots could be explained through analysis of the eigenvalues, it is likely that the size of the initial condition space that results in levitation is tied to the characteristics of the eigenvalues. The size of the initial

condition space that results in levitation is more dependent on the particle size than on the central body. Figure 5.17 illustrates this dependency. In Figure 5.17, we see that the size of the initial condition space resulting in levitation for the same particle size is very similar between Itokawa and Eros. In contrast, comparing Figure 5.17(a)($\sim$ 0.5 micron on Itokawa) and Figure 5.16(a) ($\sim$ 3 micron on Itokawa), we see that there is very little similarity in the range of initial conditions resulting in levitation when the particle size is changed.

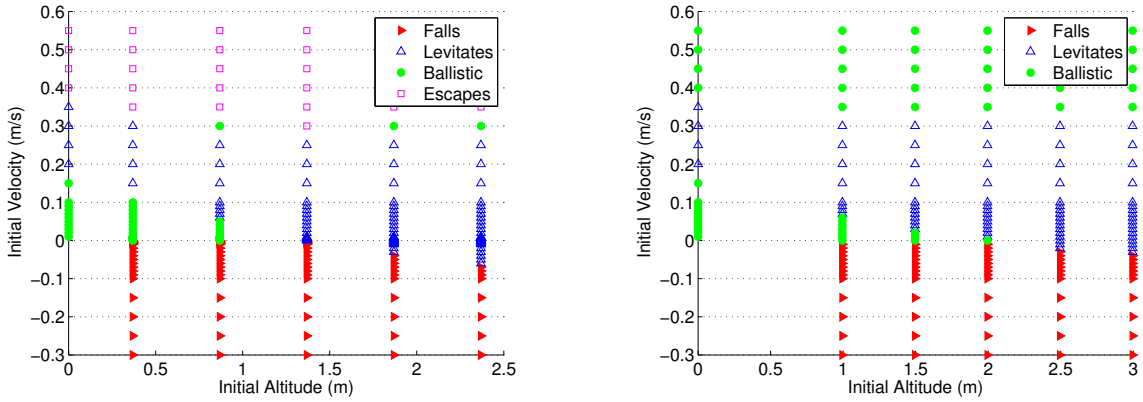

(a) Itokawa (b) Eros

Figure 5.17: Plots showing the fate of a 0.57224 micron particle with varying initial conditions in the numerically-calculated non-monotonic sheath above Itokawa and Eros. The initial particle charge is set to the initial charge of the unstable equilibrium.

5.6 Discussion

We are interested in dust particle levitation because of its implications for the morphological evolution of airless bodies and exploration mission design. We have identified the stable and unstable equilibrium altitudes as a function of particle size for the Moon, Eros and Itokawa for three different types of sheaths. The nonlinear analysis gives an indication of the range of initial states that will result in oscillation about the stable equilibria. Our discovery that the state-space behavior of particles and relative size of the initial condition space resulting in levitation can be predicted from the eigenvalues of the equilibria is a significant breakthrough in understanding levitation. By constraining the initial conditions that result in particle levitation, it will be much

easier to evaluate which particles from a given ejecta plume or that have been launched due to exploration activities will be likely to levitate. This will influence our understanding of previous lunar horizon glow observations and asteroid dust pond creation (see [47, 28]) as well as aid in the avoidance of the creation of dust clouds by exploration vehicles. Our predictions of the sizes of particles that levitate and the height at which they levitate could be used by future missions hoping to observe levitating particles.

We have shown that the stably levitated particle size, equilibrium state, and trajectory are dependent on the model of the plasma sheath used. The numerically calculated non-monotonic and monotonic sheaths described by Nitter *et al.* [38] are likely to be more representative of the plasma environment on the surface of these bodies than the analytical sheath model used by Colwell *et al.* [13, 28]. The analytical sheath model is much easier to calculate than the numerical model, however, it has two major inconsistencies: it assumes that the number densities of species other than photoelectrons are constant with altitude and the currents assume that the sheath is thermalized while the potential variation description assumes that it is not thermalized. Thus, we include the analytical model of the sheath because it has been used in previous studies of dust levitation [13, 28]. Additionally, there is uncertainty in the magnitude of the potential at the surface of these bodies. Variations in the potential and the electric field will change our predictions of the levitation heights and behaviors of particles. However, using our analysis method, it is possible to insert any sheath model and determine the equilibria and sizes of levitating particles.

The equilibria that have been presented exist at the subsolar point on these bodies. If dust particles are assumed to have some translational initial velocity component or the rotation of the central body is considered, then the dust particle will be exposed to a time-varying plasma environment. Under nominal sunlight conditions, as the dust particle moves away from the subsolar point, the electric field strength will decrease. The presence of small scale shadowing, such as would be seen in the terminator region, will cause complicated variations in the electric field strength. As the electric field strength decreases due to the movement of the dust particle away from the subsolar point, the stable equilibrium height will decrease and the dust particle will eventually

reimpact the surface. Note that although a stable equilibrium may exist for a given dust particle and a given plasma sheath profile, a particle that has been lofted in a stronger plasma sheath may not continue to oscillate in this region, since the electric field magnitude required to reverse the downward motion of the dust particle may not be present. The effect of a time-varying plasma environment will be discussed in Chapter 6.

Lunar and asteroidal dust particles are known to be very angular. Investigations of lunar regolith have shown that the surface area of regolith particles is eight times greater than the surface area of spherical particles with the same size distribution [7]. Additionally, the specific surface area of lunar dust particles (defined as the ratio of the surface area of a particle to its mass) is approximately 0.5 [7]. In this chapter, we have assumed that dust particles are spherical. The angularity of real regolith particles will result in a decreased mass for a particle with a given surface area. Additionally, the dust particle charging that has been described here assumes that the potential of the dust particle can be given by a point charge approximation. Thus, the charging of the dust particle will also be complicated by the non-spherical shape of the grains. Unfortunately, since the current to the dust particle has an exponential dependence on the electric potential of the dust particle, we cannot rewrite the equations of motion as a function of the specific surface area. Although we cannot remove the size dependence in our propagation of the trajectories, the results can be generalized by plotting the equilibria as a function of charge to surface weight ratio (instead of particle size) (see Figure 5.4). It should be noted that plotting the results as a function of charge to surface weight ratio neglects the influence of the particles' asphericity on their equilibria.

We have only considered dust particles larger than one nanometer in radius. We have chosen this as the smallest particle size considered because atomic radii are generally on the order of 0.1 nanometers. At atomic size scales, the physics of the problem may change as the "dust particle" becomes merely a large ion. Additionally, at very small particle sizes, the equilibrium charge is less than one electron. Since it is physically impossible to have fraction of an electron of charge, the dust particle could never reach the equilibrium state and discrete charging would become important in the propagation of the particle trajectories. It is possible for the dust particle to oscillate about

a non-physical equilibrium state, however, the dynamics of this motion may not be described by our current model.

Poppe *et al.* [42] create a PIC model of the plasma sheath near the Moon assuming two different distribution functions of emitted photoelectrons. Comparing our predicted levitation heights and particle sizes for the numerically-described non-monotonic sheath at the Moon to Poppe *et al.*'s predictions, we see that our results (see Figure 5.3(a)) are quite similar to those obtained for the Maxwellian distribution function in the earlier work. We see that our predicted levitation heights are slightly (approximately 2 m) higher than those predicted by Poppe *et al.*. There is good agreement between our results for the largest particle size capable of stable levitation and those obtained by Poppe using a Maxwellian photoelectron distribution. Additionally, we note that Poppe *et al.* do not identify the lower, unstable equilibria in their work. Some of the discrepancies between Poppe *et al.*'s results and those presented here may be due to the fact that Poppe *et al.* did not include any height dependent gravity strength variation and use slightly different photoelectron and solar wind electron temperatures.

Rennilson and Criswell [43] hypothesized that the Lunar Horizon Glow observed by the Surveyor spacecraft was due to the electrostatically-dominated movement of five micron (radius) particles close to the lunar surface. In all three sheaths that we have considered, the largest particle capable of stable levitation on the Moon is approximately 0.07 microns. Thus, if the observed Lunar Horizon Glow is in fact produced by scattering from five micron particles, then those particles are not levitating. The five micron particles could be exhibiting ballistic motion or escaping. Actual regolith grains are highly aspherical. Thus, it is likely that regolith grains of a given mass would have a much larger cross-sectional area (important for light scattering) than the spherical particles used in this study, which would increase our predicted maximum sizes for stable levitation. It is important to note the more general result of equilibria as a function of charge to particle surface weight presented in Figure 5.4.

It has also been suggested that the so-called "lunar streamers" observed by Apollo astronauts were caused by 0.01-10 micron dust particles at altitudes of 100 km above the lunar surface [62].

Stable equilibria at 100 km are only seen in the simplified analytically-described sheath (Figure 5.5(a)). Particles seen to levitate at this height are significantly smaller (0.1 nanometer-sized objects) than those predicted by earlier discussions of the "lunar streamers". 0.01-10 micron particles at this altitude would likely to be escaping from the Moon.

If levitating dust was responsible for the formation of the Eros dust ponds, then Figure 5.3 shows that the ponds contain particles smaller than 2 microns diameter, which is in agreement with observations requiring the particles to be smaller than 1 cm (pixel size) and possibly much smaller than 50 microns (in order to explain the relatively blue spectral signature of the ponds)[47].

Levitating dust particles have been seen experimentally by Sickafoose *et al.*[52] and Thomas *et al.*[58]. Sickafoose *et al.* specifically investigated the heights and charges of levitating dust particles. The sheath produced in their experimental set-up was unlike the sheaths that have been modeled here. The potential of the dusty surface was negative and the potential increased with altitude. From a model of the sheath potential profile, Sickafoose *et al.* identified the stable and unstable equilibrium. They also saw quite good agreement between the stable equilibria heights for a given dusty surface potential and the levitation heights observed. Additionally, it was seen that as the strength of the electric field increased, the particles levitated at higher altitudes. Unfortunately, the effect of dust particle size on levitation height was not examined.

5.7 Conclusion

Previous efforts to explore the motion of electrostatically-controlled dust particles have focused on characterizing the plasma sheath about the Moon. We have presented the first full dynamical-systems analysis of the motion of dust particles near the Moon and asteroids, using three models of the plasma sheath. This investigation identifies the equilibria of a range of dust particle sizes on these bodies. Additionally, we have conducted linear and non-linear stability analyses that show which particles will be capable of stable levitation. Our predictions of the behavior of dust particles are useful for understanding both the unperturbed natural environment of asteroids and the predicted response of the environment to future exploration activities.

Chapter 6

3D Dust Levitation Dynamics

6.1 Introduction

It has been seen that for a small range of initial conditions, dust particles can levitate (i.e., experience altitude oscillations) above the surface of an asteroid or the Moon (as discussed in Chapter 5 and [13, 28, 38, 42, 22, 23]). The *in situ* observations to date have not been capable of distinguishing between levitating grains and ballistic grains. Thus, there is no proof that electrostatic levitation occurs *in situ*. In Chapter 5, we constrained the range of initial conditions (velocity and charge, for a dust particle of a given size) that result in dust particle levitation. Thus, once the *in situ* dust lofting mechanism has been identified, it will be possible to determine if dust levitation occurs *in situ* or if it is a numerical artifact.

Chapter 5 investigated dust levitation in the 1D system. In the 1D system, we assume that the dust motion occurs in a constant plasma environment (the electric potential only changes with altitude). The plasma environment of above any given point on the body is dictated by the solar incidence angle on the surface. In the 3D system, the dust particle will experience different plasma environments as it translates across body, where the surface experiences different solar incidence angles. Particularly on fast rotating asteroids, the variation in the plasma environment due to the translation of the dust grain may significantly influence the trajectory of the grain. Thus, we study the levitation behavior of dust particles in a varying plasma environment in order to determine how the trajectories in real systems will be affected by a varying plasma environment.

6.2 Pseudo-3D System

Before implementing a fully 3D system, we approximate the 3D system by simply varying the plasma environment in the 1D model. The plasma environment does not change continuously in this model; instead the solar incidence angle is changed at certain time steps to roughly simulate the variation in the plasma environment that would be experienced in reality. Additionally, the pseudo-3D model does not include the centripetal or Coriolis accelerations.

6.2.1 Problem Description and Methods

As shown in Chapter 5, the behavior of levitating dust particles depends on the plasma sheath model that is used. In our studies of 3D dust motion, only non-monotonic potential profiles described by Nitter *et al.*[38] are used. The presence of a non-monotonic potential profile occurring *in situ* is supported by data from the Lunar Prospector mission [41] and PIC simulations [42]. Some of the parameters of the plasma are given in Table 6.1. The characteristics of the plasma sheath will vary based on the solar wind density, solar wind electron temperature and photoelectron temperature used in the model. It is necessary to numerically integrate to obtain the plasma potential profile (see Figure 6.1).

Table 6.1: Electrostatic parameters for the plasma sheath at the subsolar point. All values given are calculated at the subsolar point, except the solar wind density and plasma temperatures, which are independent of solar incidence angle.

Parameter	Value
Solar Wind Density	5.000 cm^{-3}
Solar Wind Electron Temperature	15.00 eV
Photoelectron Temperature	1.470 eV
Plasma Potential at Surface	3.225 V
Photoelectron Number Density at Surface	138.5 cm^{-3}
Debye Length	0.7643 m
Electric Field Strength at Surface	2.505 N/C
Altitude of Potential Minimum	11.63 m

Again, we assume that the dust particles and the central body are spherical and do not consider any interactions between dust particles. As given in Chapter 5, the one dimensional

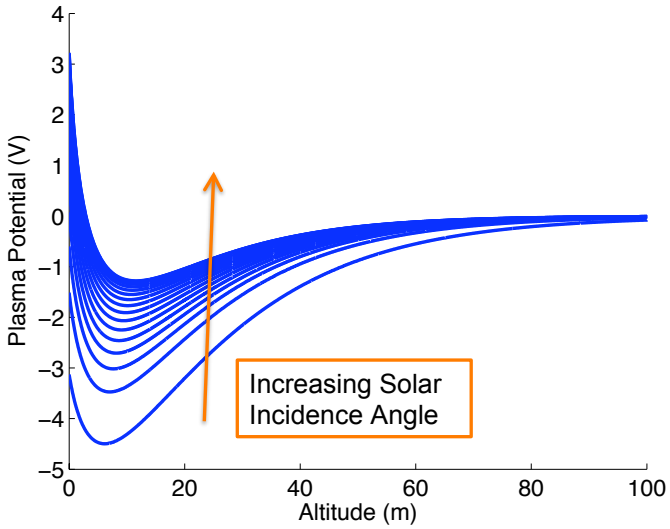

Figure 6.1: Electric potential as a function of altitude for a variety of solar incidence angles. The curve minima become shallower as the solar incidence angle increases (i.e., move away from the subsolar point).

equations of motion of a charged dust particle in a plasma sheath are modeled as:

$$m_d \ddot{h} = Q_d E - \frac{m_d g_s}{\left(\frac{h}{r_c} + 1\right)^2} \tag{6.1}$$

$$\dot{Q}_d = I_i - I_e - I_p + I_{pd} \tag{6.2}$$

where m_d is the mass of the dust particle (density assumed to be 3 g/cm^3), g_s is the gravity at the surface of the spherical body, h is the particle's altitude, r_c is the radius of the central body, E is the local electric field strength and q_d is the charge of the dust particle. The dust particle's charge is time varying due to several currents: solar wind electrons (I_e), solar wind ions (I_i), photoelectrons (I_p), and photoemission (I_{pd}). We use the form of the currents given by Nitter *et al.* [38] for this sheath. The currents to a given dust particle are time varying and depend on the local electric potential of the plasma (varies with altitude and solar incidence angle), the density of the plasma, and the charge of the particle. The charge of the dust particle is numerically integrated along with the altitude when propagating the trajectory. The discrete nature of particle charging is not included in our simulations and would only influence the trajectories of particles that have a very

small charge.

As discussed in Chapter 5, the equilibria of levitating dust particles are of interest because they give predictions of the altitudes at which particles can be observed to levitate, which has implications for our understanding of previous observations of dust motion on the Moon and will inform future missions that plan to observe levitating dust. Additionally, studying the equilibria constrains the range of dust particle sizes that are capable of levitation.

The equilibrium states are strongly tied to the plasma potential profile. Thus, the equilibria are a function of the solar incidence angle. Note that for the numerically-calculated non-monotonic sheath, a given particle size, central body mass, and solar incidence angle there are two equilibria: one stable and one unstable. Particles placed near the stable equilibria will approach the equilibria, while particles placed near the unstable equilibria will diverge. Dust particle levitation is the oscillation of particles about stable equilibria. Excluding the terminator regions, the electric field is strongest at the subsolar point, where the solar incidence angle (measured from the surface normal) is zero. Thus, as a dust particle translates across the surface of an asteroid away from the subsolar point, the altitude of the equilibria will decrease.

The electric field in the terminator regions is likely to be stronger due to the close proximity of lit and dark surfaces [15, 14]. The presence of rocks and craters will likely create numerous strong, but small scale electric fields in the terminator region. Thus, dust motion in the terminator region is not discussed in this work due to the complexity of the plasma environment there.

6.2.2 Results

We want to test the hypothesis that dust particles will oscillate about the stable equilibrium state even if that equilibrium state changes, assuming a slow rate of change. Thus, as a dust particle translates away from the subsolar point, it will oscillate about states closer and closer to the surface, since the electric field is weakening. Recall that we are not considering dust motion in the terminator region due to the complex plasma environment there. Additionally, we are interested in the magnitude of the altitude oscillations due to the weakening of the plasma environment. If

small variations in the plasma environment cause large altitude oscillations, then levitation will not result in long distance dust transport because particles will reimpact during altitude oscillations due to plasma environment variations even though stable equilibria may still exist.

We consider a 0.572 micron radius dust particle launched from the subsolar point above a spherical Eros in the 1D system with the initial state of the dust particle given in Table 6.2. These initial conditions are chosen because it is known from the analysis in Chapter 5 that they produce levitation. Additionally, we launch the dust particle from some altitude below the stable equilibria so that the numerical system will naturally approach the stable equilibrium. The trajectory is then propagated for 2500 seconds, which is long enough to see noticeable damping in the oscillations about the stable equilibrium (see Figure 6.2(a)). After 2500 seconds, the solar incidence angle is changed to 1° and the trajectory is propagated for 500 seconds. The solar incidence angle is subsequently increased by 1° every 500 seconds (see Figure 6.2). The 1° per 500 second rate of variation in the solar incidence angle corresponds to 50 hour rotation period. This step-wise variation in the solar incidence angle approximates the continuous variation that would be experienced in a truly 3D model. Additionally, the step-wise variation of the solar incidence angle should cause a more marked overshoot of the equilibrium state than would be seen in a continuously varying model.

Table 6.2: Initial conditions for the numerical simulation discussed in this chapter. Dust particle radius is 0.572 microns and density is 3 g/cc.

Initial Height	0.995 m
Initial Velocity	0.250 m/s
Initial Charge	1.76×10^{-17} C

The first key observation from Figure 6.2 is that the numerically calculated equilibrium state is approximately 5mm above the state about which the dust particles are oscillating. We use the Newton-Raphson method to solve for the equilibrium state, thus we must specify an acceptable error while iterating for the solution. In this case, the tolerance that we have specified has resulted in a 5mm error in our solution of the equilibrium altitude, which could be improved in future work, but is not necessary given the much larger uncertainty in the *in situ* plasma environment.

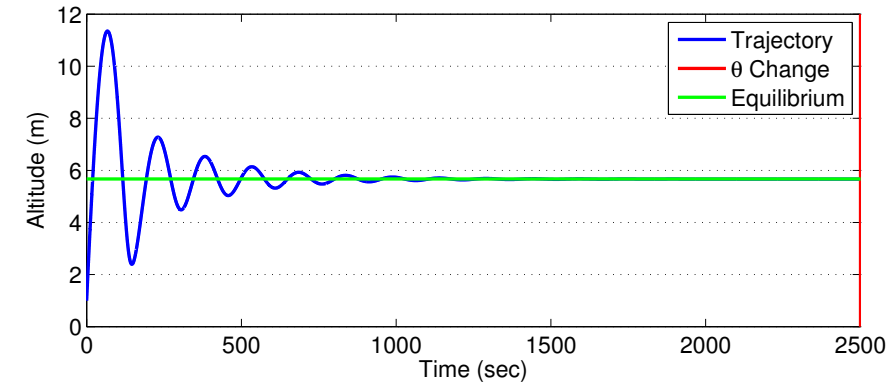

(a) Subsolar Point

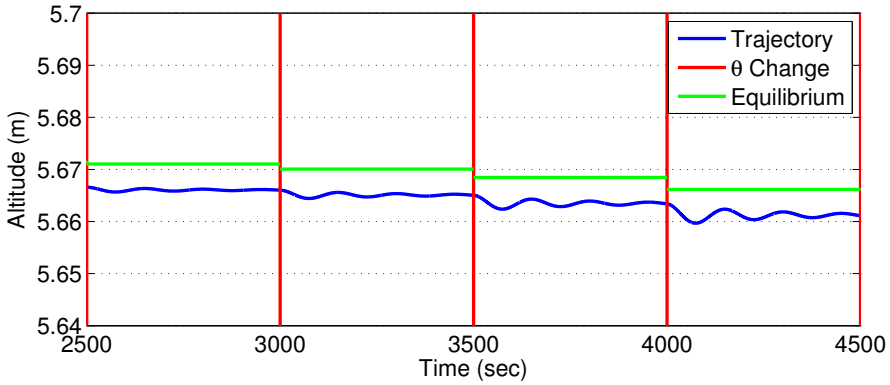

(b) θ =1°- 4°

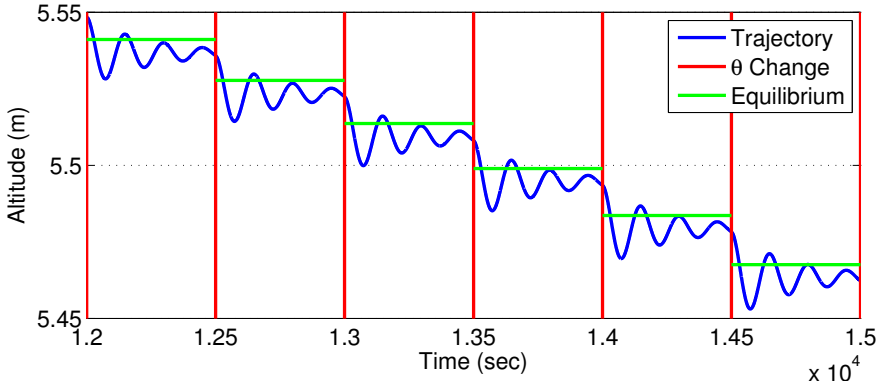

(c) θ =20°- 25°

Figure 6.2: Investigation of the impact of a varying plasma environment variation on particle trajectories in the 1D system. The solar incidence angle (θ) and thus, plasma environment, is changed at each of the red vertical lines. This simulates a dust particle traveling away from the subsolar point.

Secondly, it can be seen in Figure 6.2 that, as predicted, the dust particles oscillate about the moving equilibrium state. Thus, provided that the translational velocity of the dust particle is slow enough, it is likely to oscillate about progressively lower equilibria as it moves to regions of increased solar incidence angle. Note that this trend may not continue in the terminator region, due to the complex plasma environment there.

Finally, Figure 6.2 shows the amplitude of the altitude oscillations about the moving equilibrium state. From Figure 6.2(c), it can be seen that the maximum oscillation amplitude is approximately 2 mm. Given these small altitude oscillations, it is unlikely that including a time varying potential profile will cause the premature impact of levitating dust particles, since the stable equilibria states are at least 1 m above the surface for all of the solar incidence angles considered. At faster rates of solar incidence angle variation, the altitude oscillation amplitudes may increase, but it is unlikely that they would increase to the extent required to deposit dust particles in regions where stable equilibria still exist for that particle size.

6.3 Fully 3D System

In the previous section, we explored dust motion in step-wise varying plasma environment and saw that particles oscillated about the varying equilibria, which approach the surface as the solar incidence angle increases. The previous simulation did not include the full dynamics of a rotating body. In this simulation, we will include the full dynamics of a rotating central body as well as a continuously varying plasma environment.

6.3.1 Problem Description and Methods

Again, we follow the description by Nitter *et al.* [38] of the plasma sheath vertical potential variation and the charging currents to the dust particles. Although Nitter *et al.* describe only the variation in the plasma profile normal to the surface, we numerically approximate the electric field in latitudinally and longitudinally varying directions.

We propagate the dust particle in a body-fixed rotating frame, where the body is assumed

to be rotating about the Z axis, which is normal to the plane of the equator. The inertial X axis points towards the sun and the body fixed X axis points towards the sun at the initial epoch. Additionally, we assume that the central body rotates at a constant rate. Thus, the acceleration of the particle in the body-fixed frame is given by:

$$\begin{bmatrix} \ddot{x} \\ \ddot{y} \\ \ddot{z} \end{bmatrix} = \frac{-\mu}{R^3}\vec{\mathbf{R}} + \frac{q_d E_h}{m_d}\hat{\mathbf{R}} + \frac{q_d E_\phi}{m_d}\hat{\mathbf{d}}_\phi + \frac{q_d E_\psi}{m_d}\hat{\mathbf{d}}_\psi - 2\begin{bmatrix} -v_y \\ v_x \\ 0 \end{bmatrix}\omega_z + \begin{bmatrix} x \\ y \\ 0 \end{bmatrix}\omega_z^2 \tag{6.3}$$

where μ is the gravitational parameter of the body, v_i is the component of the body-fixed velocity in the ith direction, R is the magnitude of the position vector (and $R = h + r_c$), $\vec{\mathbf{R}}$ is the position vector of the dust particle in the rotating frame and $\hat{\mathbf{R}}$ is the normalized position vector. E_h is the electric field in the radial direction given by Nitter *et al.* [38]. Figure 6.3 depicts the body fixed and particle-fixed reference frames. The electric fields in the longitudinal (E_ϕ) and latitudinal (E_ψ) directions are numerically approximated using the definition of electric field as the negative gradient of the potential profile. Thus, we step ± 1 degree in the $\hat{d_\phi}$ and $\hat{d_\psi}$ directions and use the negative slope as the electric field in these directions. Additional fidelity in the electric field could be achieved by using a Particle-In-Cell code to calculate the density of the plasma species. The present method for approximating the transverse electric fields is sufficient for our purposes of propagating dust particles about a spherical body. The fifth term in Eq. (6.3) is the Coriolis acceleration and the final term is the centrifugal force.

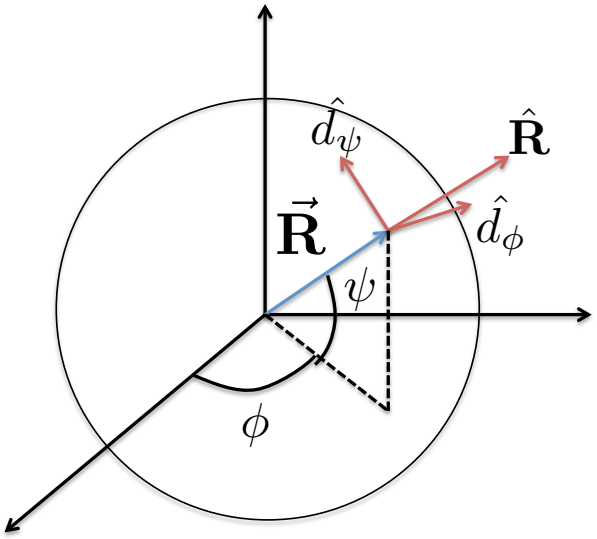

Figure 6.3: Diagram of the body-fixed and particle-fixed reference frames used.

The unit vectors of the particle-fixed frame are defined by:

$$\hat{\mathbf{R}} = \begin{bmatrix} \cos\psi\cos\phi \\ \cos\psi\sin\phi \\ \sin\psi \end{bmatrix} \tag{6.4}$$

$$\hat{d_\phi} = \begin{bmatrix} -\cos\psi\sin\phi \\ \cos\psi\cos\phi \\ 0 \end{bmatrix} \tag{6.5}$$

$$\hat{d_\psi} = \begin{bmatrix} -\sin\psi\cos\psi\cos\phi \\ -\sin\psi\cos\psi\sin\phi \\ \cos^2\psi \end{bmatrix} \tag{6.6}$$

In Section 6.2, we changed the solar incidence angle by 1° every 500 seconds, which corresponds to a rotation period of 50 hours. In the fully 3D system, the solar incidence angle will change continuously, and the rotation rate of the central body is 5 hours. The rotation rate of Eros is approximately 5 hours, thus in the 3D system we are more accurately simulating this body. The particle size and plasma parameters used in Section 6.2 are used in this system. In this simulation,

since the plasma environment changes continuously, we start the simulation with the dust particle placed at the same altitude, velocity and charge seen in the pseudo-3D investigation when the solar incidence angle is changed to 1°. Additionally, the particle is initially placed at a latitude of zero degrees, a longitude of 1 degree East of the subsolar point, and with the same angular velocity as the central body. The initial state used is given in Table 6.3. Although the initial state has a slightly negative initial velocity, it will be shown that this has little impact on the overall trajectory of the particle. In this chapter, we do not investigate the motion of the dust particles to this initial state; we are merely interested in the motion of the dust particles as the solar incidence angle changes.

Table 6.3: Initial conditions for the fully 3D numerical simulation discussed in this work. Dust particle radius is 0.572 microns and density is 3 g/cc. This state is identical to the state of the dust particle when the solar incidence angle changes to 1° in the pseudo-3D simulation.

Initial Height	5.67 m
Initial Vertical Velocity	-1.17 $\times 10^{-6}$ m/s
Initial Charge	6.93 $\times 10^{-17}$ C

6.3.2 Results

As mentioned previously, in this formulation of the dust propagation problem, we include an approximation of the transverse electric field. Thus, dust particles will be accelerated towards the poles and towards the terminator. Transverse electric fields were not included in the pseudo-3D formulation. We do not include the electrostatic force at solar incidence angles higher than 80°, due to the complexity of the potential variations in the terminator region. Additionally, for the present case, we launch the dust particle from the equator. Thus, there will be no net acceleration in towards either of the poles and the transverse acceleration will only serve to accelerate the dust particle towards the terminator region in the plane of the equator. Figure 6.4 shows a dust particle trajectory in the fully 3D formulation both with and without the transverse electric field.

Figure 6.4(a) shows the full trajectory of the dust particle with and without the transverse electric field included. The stable equilibria altitudes for each solar incidence angle are also plotted.

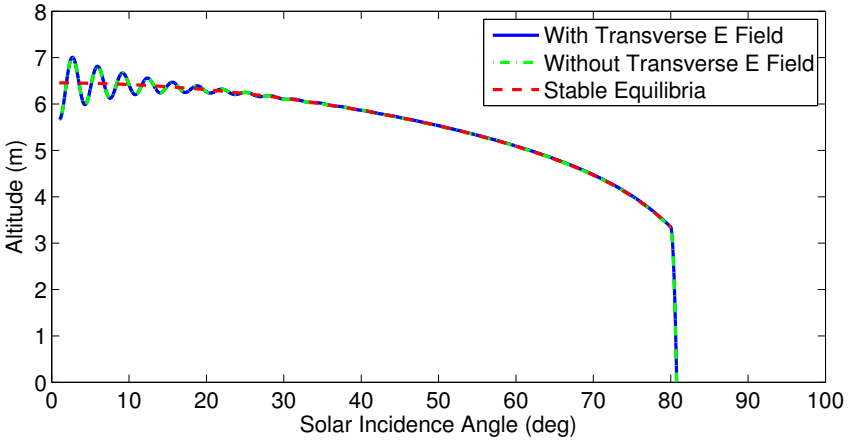

(a) Trajectories Compared to Equilibria

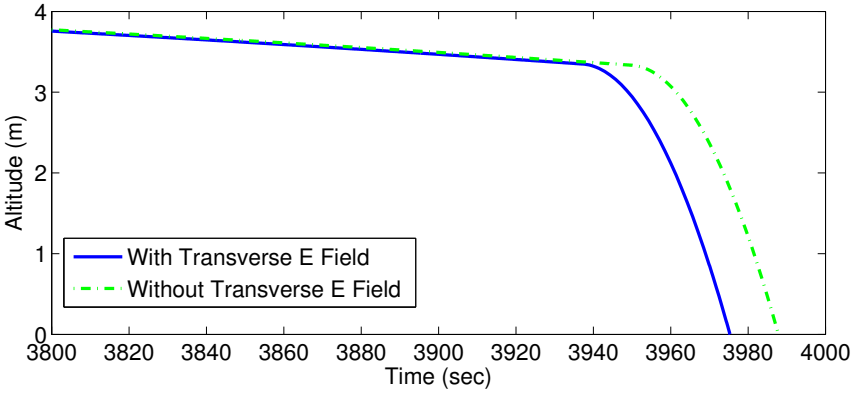

(b) Altitude Comparison

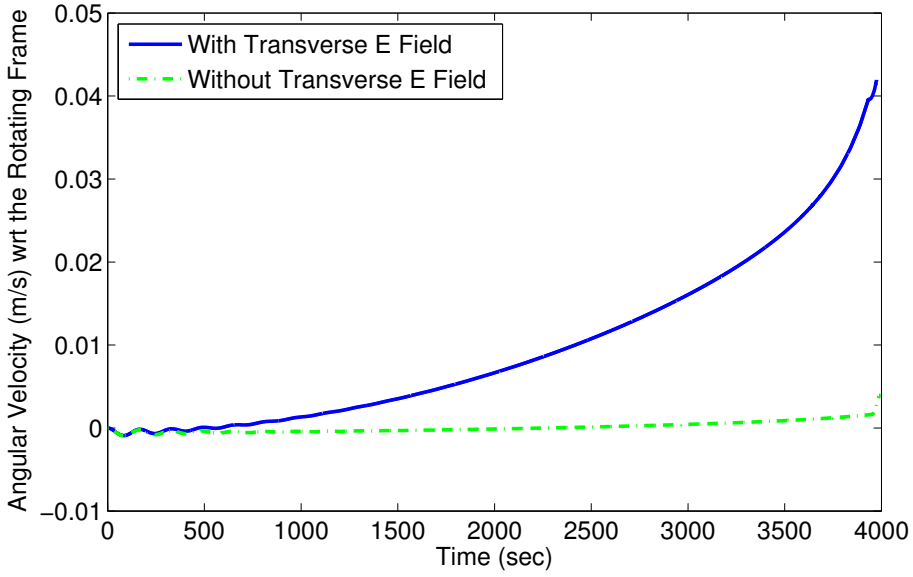

(c) Angular Velocity

Figure 6.4: Plots of trajectories including and neglecting the transverse electrostatic force for the fully 3D case with a ~ 0.6 micron particle above Eros. The trajectory was started one degree east of the subsolar point.

The equilibria are located numerically and are at slightly higher altitudes for the fully 3D system than for the 1D system due to the presence of the Coriolis and centrifugal accelerations. In Figure 6.4(a), it can be seen that the dust particles initially undergo large altitude oscillations. Recall that the dust particles are initially placed near the equilibrium state of the non-rotating system at a solar incidence angle of 1°. Thus, when placed in the rotating system, they experience an upwards acceleration in order to reach the higher equilibrium altitude of this system. The oscillations damp and it can be seen that the trajectories generally follow the stable equilibria; the particles approach the surface as the solar incidence angle increases. The electrostatic force is turned off at solar incidence angles larger than 80°. The particles impact the surface shortly after the electrostatic force disappears.

Figure 6.4(b) gives a close-up view of the two trajectories as a function of time. Figure 6.4(b) shows the effect of the transverse electric field, which acts to accelerate the dust particle towards the terminator. Thus, the trajectory that includes the transverse electrostatic force impacts the surface before the trajectory that neglects this force.

Figure 6.4(c) shows the angular velocity of the particles with respect to the body-fixed rotating frame. When the transverse electrostatic force is included, Figure 6.4(c) shows the angular velocity of the dust particle increasing with respect to the rotating frame. This supports the observation in Figure 6.4(b) that the dust particle experiencing the transverse electrostatic force impacts the surface before the particle where the transverse electrostatic force is neglected.

Figure 6.5 and Figure 6.6 show the trajectory of a dust particle in the fully 3D system with the same initial conditions as Figure 6.4 with the exception that it was started at 70° west of the subsolar point. Thus, during the initial part of the trajectory, the tangential electrostatic acceleration acts against the motion of the dust particle, essentially slowing its transit towards the subsolar point. From Figures 6.5(a) and 6.5(b), it can be seen that as the dust particle approaches the subsolar point, the altitude of the particle increases. Basically, after the initial oscillatory period, the trajectory follows the evolving equilibrium state (the equilibrium height increases as the solar incidence angle decreases to zero). Note that, as seen in Figure 6.4(a), the dust particle

reimpacts the surface shortly after the solar incidence angle reaches 80°, which is expected since the electrostatic force is turned off at this point. Additionally, the influence of the tangential electrostatic acceleration towards the terminator can be seen in Figure 6.5(c) since the velocity of the grain in the $\hat{\phi}$ direction decreases while the grain is west of the subsolar point.

It is also possible to see the influence of the transverse electrostatic force in plots of the time rate of change of the angular momentum ($\dot{H} = \vec{\mathbf{R}} \times \vec{\mathbf{a}}$, Figure 6.6(a)) and the specific orbital energy ($\dot{\mathcal{E}} = \vec{\mathbf{v}} \cdot \vec{\mathbf{a}}$, Figure 6.6(b)). Since the only non-radial component of the acceleration is the transverse electrostatic acceleration, it is straightforward to see that the time rate of change of the angular momentum will be negative until the dust particle passes the subsolar point, which is shown in Figure 6.6(a). Additionally, we see that the orbital energy (Figure 6.6(b)) is decreasing while the dust grain is west of the subsolar point, which makes sense because the tangential electrostatic acceleration is slowing the particle's motion about the body. During the oscillatory phase of the trajectory, the time rate of change of the orbital energy is occasionally positive because the particle also experiences radial velocity and acceleration components during this phase of the trajectory.

6.4 Discussion

We have investigated the influence of a time-varying plasma sheath on the levitation of dust particles using a modified 1D simulation and a fully 3D simulation. In the 1D simulation, we approximated a 3D system by triggering changes in the plasma sheath at specific time intervals. With these abrupt changes in the plasma sheath, the dust particle experienced altitude oscillations, but the magnitude of the oscillation was a small fraction of the total altitude, indicating that the dust particle would track the equilibria in a fully 3D system. In our simulations with the fully 3D system, we increased the rotation of the central body by a factor of 10 from the 1D simulation. This increase more accurately approximates conditions likely to be present on asteroids and, if anything, should cause increased altitude oscillation magnitudes. However, simulations showed that the dust particles experienced few altitude oscillations in the fully 3D system and closely followed the changing equilibria. In fact, oscillations were only observed at the beginning of the simulation

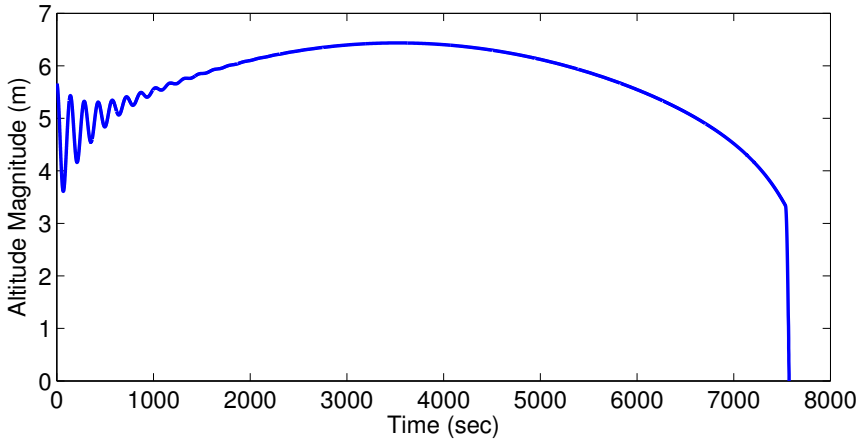

(a) Altitude

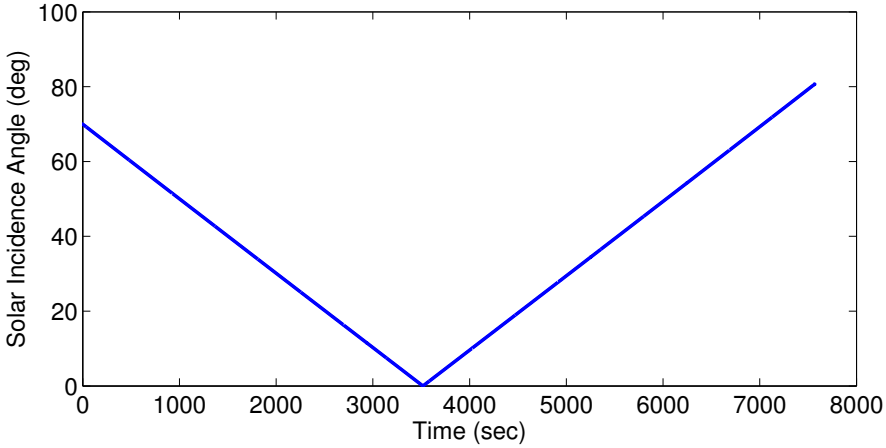

(b) Solar Incidence Angle

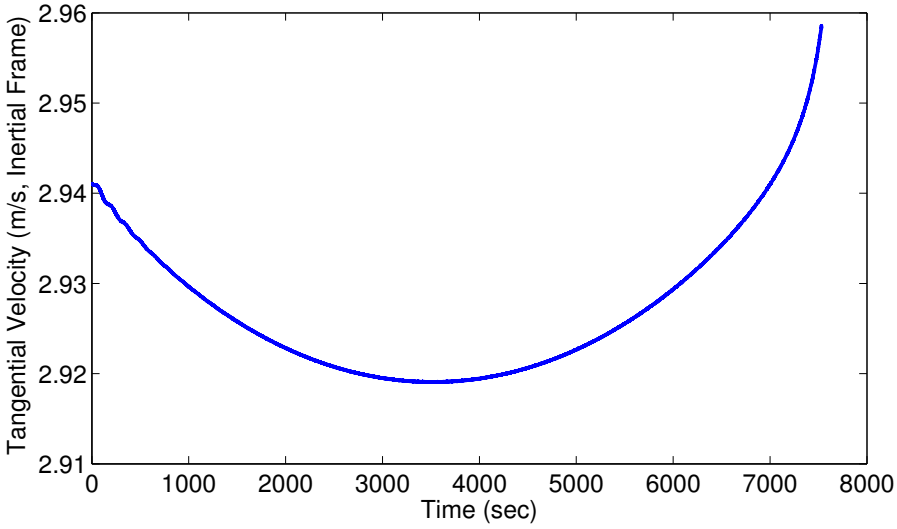

(c) Tangential Velocity

Figure 6.5: Plots of a trajectory including the transverse electrostatic force for the fully 3D case with a ~ 0.6 micron particle above Eros. The trajectory was started 70 degrees west of the subsolar point.

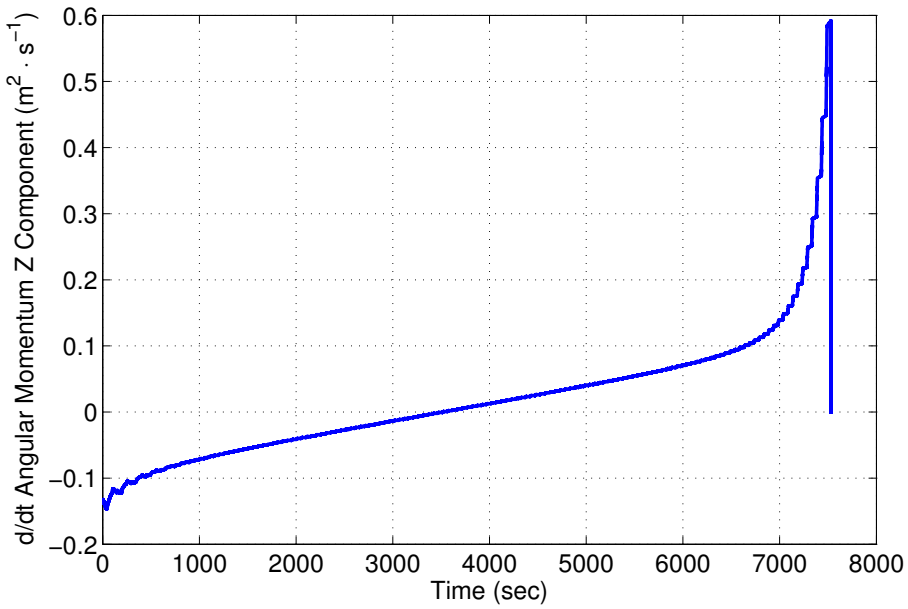

(a) Time Rate of Change of Angular Momentum

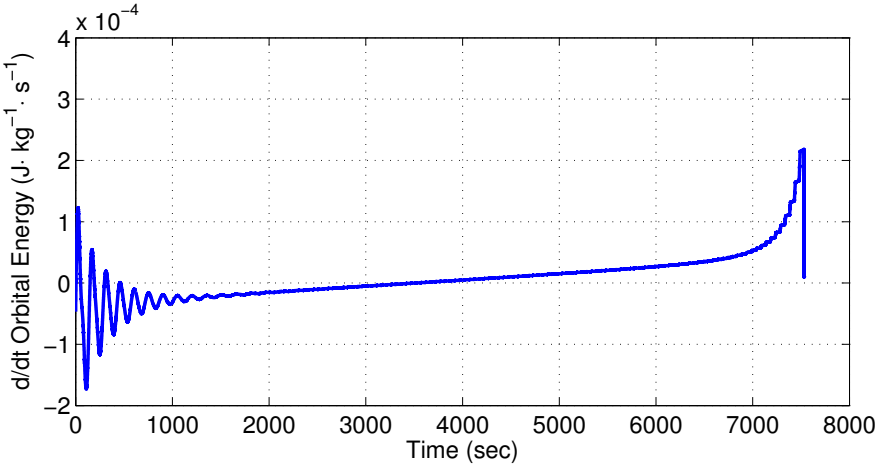

(b) Time Rate of Change of Orbital Energy

Figure 6.6: Change in orbit characteristics of a ~ 0.6 micron particle above Eros, propagated in the fully 3D system. The trajectory was started 70 degrees west of the subsolar point.

due to the discrepancy between the initial particle state and the equilibrium state for the rotating system. Additionally, in the fully 3D system, we implemented an approximation of the transverse electric fields. Since the particles were launched from the equator, no latitudinal accelerations were observed. However, comparing a trajectory including the longitudinal electrostatic acceleration to a trajectory that neglected the transverse electric field showed the the transverse electrostatic force

did significantly alter the trajectory.

6.5 Conclusions

The feasibility of dust levitation *in situ* has important implications for both for our understanding of the evolution of airless bodies and the design of spacecraft to visit these bodies. In Chapter 5, we constrain the range of initial conditions that result in dust levitation in a 1D system, assuming a constant plasma environment. In reality, dust particles will experience a varying plasma environment due to their translational motion. In this chapter, we have investigated the response of a levitating dust particle above the asteroid Eros to changes in the plasma environment. We have seen that dust particles oscillate about the time-varying stable equilibrium, for a rotation period of the central body of 5 hours. Thus, it is unlikely that a dust particle will reimpact during oscillations due to plasma environment changes. The sensitivity of these results to the rotation period of the central body will be studied in future work. This investigation shows that variation in the plasma environment due to central body rotation is unlikely to cause large altitude oscillation in the trajectories of levitating dust particles.

Chapter 7

Conclusions and Future Work

This thesis has investigated electrostatically-dominated dust motion on asteroids and the Moon. The influence of cohesion on electrostatic dust lofting is investigated analytically and experimentally. Additionally, the dynamics of levitating grains are investigated for 1D and 3D systems. While these investigations do not resolve the controversial question of whether or not electrostatic dust lofting and/or levitation occurs *in situ*, they do further the discussion of the feasibility of these processes and influence the interpretation of future spacecraft observations.

This thesis shows that cohesion, which has previously been neglected in analysis of the feasibility of electrostatic lofting, significantly influences predictions of the electric fields required for lofting and the particle sizes that are expected to be lofted. Given our model of cohesion, we see that the smallest, sub-micron particles require larger electric fields to loft than intermediate-sized ($>$ 100 micron) particles. Additionally, if the charging on a dust particle is assumed to be given by Gauss' law, the electric field required to loft particles is several orders of magnitude larger than that predicted to be present *in situ*. This preferential lofting of intermediate-sized grains has been proven experimentally as well. We experimentally demonstrate that 15 micron diameter dust grains are electrostatically lofted at lower electric field strengths than 5, 10, 20 or 25 micron grains. Additionally, we experimentally demonstrate that grain charging is not properly predicted by Gauss' law (as had been previously hypothesized), but that the charging is likely to be proportional to the Gauss' law prediction.

The preferential lofting of intermediately-sized dust particles has implications for our inter-

pretation of Lunar Horizon Glow observations and future limb observations of airless bodies. If the relatively small 0.2 micron (from the 'lunar streamer' observations [62]) or 10 micron (from the Lunar Horizon Glow observations [43]) particles observed are truly electrostatically lofted, then either the Hamaker constant for lunar regolith is incorrect or grain charging is amplified far beyond Gauss' law. Although intermediately-sized grains are easiest to loft, they will have a lower peak altitude than smaller grains. Thus, small grains may continue to be important for limb observations, although they may contribute less to regolith redistribution than larger grains.

A comprehensive study of the dynamics of electrostatic dust levitation is also presented. The dynamics are studied for three sheath models, a wide range of particle sizes, and three central body masses. The equilibria about which dust particles are expected to levitate and the largest particle sizes capable of levitation are identified for the three bodies. The particle sizes and altitudes that are expected for levitation are important for the interpretation of future limb observations of airless bodies. For the linearized analysis, the timescales of the motion are calculated and it is shown that from the timescales, the structure of the state space plot (essentially a non-linear stability analysis) can be predicted. For the non-monotonic numerically-defined sheath, we show that it is the particle size rather than the central body mass that dictates the structure of the state space plots (and correspondingly, the range of initial conditions that result in levitation). Our analysis of the initial conditions that result in levitation will aid in assessing the feasibility of electrostatic levitation occurring *in situ* once a feasible dust launching mechanism has been identified.

The dynamics of a dust particle in a time varying plasma environment (the 3D motion model) have also been studied. It has been seen that after the initial oscillation period, the dust particles move along the changing equilibria with minimal oscillations. Since the oscillations due to the changing of the equilibria are negligible, the particles do not reimpact until the electrostatic force is artificially turned off. Since the plasma environment is very complicated in the terminator region, the electrostatic force is turned off once the solar incidence angle reaches 80°.

The equilibria identified for the 1D system provide predictions of the altitudes that should be targeted by future missions hoping to observe levitating grains. Additionally, our estimates of

particle sizes likely to levitate for a given central body may be used by future missions with limb observations, since particle size directly influences the light scattered that would be observed by these missions. The possibility of levitating grains will also influence the predicted dust lofting rate required to produce the light scattering observed. Identifying the range of initial velocities that results in levitation is important for future surface exploration missions that are likely to cause dust to be released from the surface. Additionally, our understanding of the lifetimes of levitating dust in a varying plasma environment are also important for surface exploration missions.

The next step for studying electrostatic levitation is to include an accurate central body shape model with the proper plasma environment in the terminator region. When this thesis topic was proposed, I had planned to implement an accurate shape model of Eros during the study of the 3D dynamics of the dust particles. However, this was not pursued. Although the varying electrostatic and gravitational forces due to Eros' asphericity would undoubtably influence the trajectory of the particle on the dayside of the body, it is the behavior of the dust particles in the terminator region that is the most interesting since particles are likely to be deposited, launched and observed by spacecraft in this region. However, our numerically-defined sheath model is not accurate in the terminator region and so the results of a 2D Particle-In-Cell code should be used to define the sheath here. We chose to pursue the experimental verification of the theory of cohesion in electrostatic dust lofting, which was not proposed in the thesis proposal, instead of implementing the Eros shape model.

There are many additional experiments that could be done to further understand electrostatic dust lofting. The first topic that should be pursued is the influence of grain shape in electrostatic lofting. The experiment presented here used very uniformly sized, spherical polystyrene grains. The experiment should be repeated using narrowly sieved simulant samples. The asphericity of the simulant grains will likely to change the particle size that is easiest to loft and the results can be compared to a more detailed theory of cohesion. Secondly, the experiment should be repeated with different dust preparations. In this experiment, the dust was stored in tightly sealed eye-drop containers at atmospheric pressure and then exposed to vacuum for approximately 20 hours prior to

the beginning of the experiment. Storing the dust in a vacuum or exposing the dust to vacuum for a shorter period of time will change the strength of the cohesion between the grains. If the cohesion between the grains decreases (as is likely to occur if the grains are in vacuum for a shorter duration), then more spreading should be observed. Additionally, combining the results of the spreading with a different preparation with the results presented here will allow us to make predictions about the form of the grain charging's dependence on the particle size. Although the preparation would be difficult, a third possible experiment is to mix two different sized dust samples and observe the influence on spreading.

Finally, the most pressing topic impeding our assessment of the feasibility of electrostatic dust lofting is the lack of understanding of grain charging on the surface of an airless body. Our colleagues at Goddard Spaceflight Center [44] are attempting to address this issue by modeling the capacitance of the grains. Additionally, efforts have been made to measure the charge experimentally [59], however these efforts have been contaminated by triboelectric charging. By systematically measuring the cohesion between grains (using an atomic force microscope) and the electric field at very small scales near a dust pile while spreading is on-going, it should be possible to experimentally determine the charge on the grains.

Bibliography

[1] Willy Benz and Eric Asphaug. Catastrophic disruptions revisted. Icarus, 142:5–20, 1999.

[2] Otto Berg, Henry Wolf, and John Rhee. Lunar soil movement registerd by the apollo 17 cosmic dust experiment. In Interplanetary Dust and Zodiacal Light, volume 48 of Lecture Notes in Physics, pages 233–237. Springer Berlin / Heidelberg, 1976.

[3] Otto E. Berg, F. F. Richardson, and H. Burton. Apollo 17 Preliminary Science Report, chapter 16. Lunar Ejecta and Meteorites Experiment. NASA, 1973.

[4] C.I. Calle, C.R. Buhler, M.D. Hogue, M.R. Johansen, N.J. Van Suetendael, and et al. Development of a dust mitigation technology for thermal radiators for lunar exploration. In IEEE Aerospace Conference, number 1307, 2010.

[5] C.I. Calle, C.R. Buhler, J.L. McFall, and S.J. Snyder. Particle removal by electrostatic and dielectrophoretic forces for dust control during lunar exploraiton missions. Journal of Electrostatics, 67:89–92, 2009.

[6] Humberto Campins, Kelsey Hargrove, Noemi Pinilla-Alonso, Ellen S. Howell, Michael S. Kelley, Javier Licandro, T. Mothé-Diniz, Y. Fernández, and Julie Ziffer. Water ice and organics on the surface of the asteroid 24 themis. Nature, 464:1320–1321, April 2010.

[7] W. David Carrier, Gary R. Olheoft, and Wendell Mendell. Lunar Sourcebook, chapter Physical Properties of the Lunar Surface, pages 478–481. Cambridge University Press, 1991.

[8] A. Castellanos. The relationship between attractive interparticle forces and bulk behavior in dry and uncharged fine powders. Advances in Physics, 54(4):263–276, 2005.

[9] Francis F. Chen. Lecture notes on langmuir probe diagnostics. IEEE-ICOPS Meeting, June 2003.

[10] A.F. Cheng, N. Izenburg, C.R. Chapman, and M.T. Zuber. Ponded deposits on asteroid 433 eros. Meteoritics and Planetary Science, 37, 2002.

[11] R.N. Clark. Detection of absorbed water and hydroxyl on the moon. Science, 326:562–564, October 2009.

[12] J.E. Colwell, Scott Robertson, Mihály Horányi, Xu Wang, Andrew Poppe, and Patrick Wheeler. Lunar dust levitation. Journal of Aerospace Engineering, 22(1):2–9, January 2009.

[13] Joshua E. Colwell, Amanda A.S. Gulbis, Mihaly Horanyi, and Scott Robertson. Dust transport in photoelectron layers and the formation of dust ponds on eros. Icarus, 175:159–169, 2005.

[14] David R. Criswell and Bibhas R. De. Intense localized photoelectric charging in the lunar sunset terminator region: 2. supercharging at the progression of sunset. Journal of Geophysical Research, 82(7):1005–1007, March 1977.

[15] Bibhas R. De and David R. Criswell. Intense localized photoelectric charging in the lunar sunset terminator region: 1. development of potentials and fields. Journal of Geophysical Research, 82(7):999–1004, March 1977.

[16] D. Diebold, N. Hershkowitz, A.D. Bailey III, M.H. Cho, and T. Intrator. Emissive probe current bias method of measuring dc vacuum potential. Review of Scientific Instruments, 59(2):270–275, 1988.

[17] T.M. Flanagan and J. Goree. Dust release from surfaces exposed to plasma. Physics of Plasmas, 13:123504, 2006.

[18] A. Fujiwara, J. Kawaguchi, D.K. Yeomans, M. Abe, and et al. The rubble-pile asteroid itokawa as observed by hayabusa. Science, 312:1330–1334, 2006.

[19] David A. Glenar, Timothy J. Stubbs, James E. McCoy, and Richard R. Vondrak. A reanalysis of the apollo light scattering observations, and implications for lunar exospheric dust. Planetary and Space Science, 59(14):1695–1707, 2011.

[20] R.J.L. Grard and J.K.E. Tunaley. Photoelectron sheath near a planar probe in interplanetary space. Journal of Geophysical Research, 76(10):2498–2505, April 1971.

[21] J.S. Halekas, G.T. Delory, R.P. Lin, T.J. Stubbs, and W.M. Farrell. Lunar prospector observations of the electrostatic potential of the lunar surface and its response to incident currents. Journal of Geophysical Research, 113:A09102, 2008.

[22] Christine M. Hartzell and Daniel J. Scheeres. Dynamics of levitating dust near equilibria on asteroids. In Division of Planetary Sciences Conference. American Astronomical Society, October 2011.

[23] Christine M. Hartzell and Daniel J. Scheeres. Dynamics of levitating dust particles near asteroids and the moon. In AAS Spaceflight Mechanics Conference, number AAS 11-104. American Astronomical Society, 2011.

[24] C.M. Hartzell and D.J. Scheeres. The role of cohesive forces in particle launching on the moon and asteroids. Planetary and Space Sciences, 59:1758–1768, November 2011.

[25] O. Havnes, C.K. Goertz, G.E. Morfill, E. Gr´un, and W. Ip. Dust charges, cloud potential, and instabilities in a dust cloud embedded in a plasma. Journal of Geophysical Research, 92(A3):2281–2287, March 1987.

[26] L.O. Heim, J. Blum, M. Preuss, and H.J. Butt. Adhesion and friction forces between spherical micrometer-sized particles. Physical Review Letters, 83(16):3328–3331, 1999.

[27] M. Horányi, T. Munsat, S.H. Robertson, Z. Sternovsky, and X. Wang. Impact generated plasmas on the lunar surface. In American Geophysical Union Fall 2009 Meeting, number P32A-04, 2009.

[28] Anna L.H. Hughes, J.E. Colwell, and Alexandria Ware DeWolfe. Electrostatic dust transport on eros: 3d simulations of pond formation. Icarus, 195:630–648, 2008.

[29] K.L. Johnson, K. Kendal, and A.D. Roberts. Surface energy and the contact of elastic solids. Proceedings of the Royal Society London, pages 301–313, 1971.

[30] A.N. Krot. Bringing part of an asteroid back home. Science, 333:1098–1099, August 2011.

[31] Lucas Laursen. Apollo physicist launches noisy dustup over old moon data. Science, 332:1493, June 2011.

[32] Pascal Lee. Dust levitation on asteroids. Icarus, 124:181–194, 1996.

[33] S. Lin, S. Fraden, and Y. Hu. The potential energy of a pair of polystyrene spheres in alternating electric fields. In F.E Filisko and K.O. Havelka, editors, Proceedings of the Electrorheological Materials and Fluids Symposium 208th National Meeting of the American Chemical Society. Plenum Publishing, 1995.

[34] J. Marshall, D. Richard, and S. Davis. Electrical stress and strain in lunar regolith simulants. Planetary and Space Sciences, 2011, In Press.

[35] Frank Melandsø, Torsten K. Aslaksen, and Ove Havnes. A kinetic model for dust acoustic waves applied to planetary rings. Journal of Geophysical Research, 98(A8):13315–13323, 1993.

[36] H. Miyamoto, H. Yano, D.J. Scheeres, S. Abe, and et al. Regolith migration and sorting on asteroid itokawa. Science, 316:1011–1014, May 2007.

[37] T. Nitter, T.K. Aslaksen, F. Melandsø, and O. Havnes. Levitation and dynamics of a collection of dust particles in a fully ionized plasma sheath. IEEE Transactions on Plasma Science, 22(2):159–172, 1994.

[38] Tore Nitter, Ove Havnes, and Frank Melandsø. Levitation and dynamics of charged dust in the photoelectron sheath above surfaces in space. Journal of Geophysical Research, 103:6605–6620, 1998.

[39] H.A. Perko, J.D. Nelson, and W.Z. Sadeh. Surface cleanliness effect on lunar soil shear strength. Journal of Geotechnical and Geoenvironmental Engineering, 127(4):371–383, April 2001.

[40] C.M. Pieters, J. N. Goswami, R.N. Clark, M. Anndurai, J. Boardman, B. Buratti, J.-P. Combe, M. D. Dyar, R. Green, J.W. Head, C. hibbitts, M. Hicks, P. Isaacson, R. Klima, G. Kramer, S. Kumar, E. Livo, S. Lundeen, E. Malaret, T. McCord, J. Mustard, J. Nettles, N. Petro, C. Runyon, M. Staid, J. Sunshine, L. A. Taylor, S. Tompkins, and P. Varanasi. Character and spatial distribution of oh/h2o on the surface of the moon seen by m3 on chandrayaan-1. Science, 326:568–572, October 2009.

[41] Andrew Poppe, Jasper S. Halekas, and Mihály Horányi. Negative potentials above the day-side lunar surface in the terrestrial plasma sheet: Evidence of non-monotonic potentials. Geophysical Research Letters, 38:L02103, 2011.

[42] Andrew Poppe and M. Horanyi. Simulations of the photoelectron sheath and dust levitation on the lunar surface. Journal of Geophysical Research, 115:A08106, August 2010.

[43] J. J. Rennilson and David R. Criswell. Surveyor observations of lunar horizon-glow. The Moon, 10:121–142, 1974.

[44] Denis T. Richard, Michael R. Collier, Timothy J. Stubbs, John W. Keller, William M. Farrell, and John R. Marshall. A fractal model for the capacitance of lunar dust and lunar dust aggregates. American Geophysical Union, December 2011.

[45] James E. Richardson, H. Jay Melosh, and Richard Greenberg. Impact-induced seismic activity on asteroid 433 eros: A surface modification process. Science, 306:1526–1529, November 2004.

[46] Andrew Rivkin and Joshua P. Emery. Detection of ice and organics on an asteroidal surface. Nature, 464:1322–1323, April 2010.

[47] M.S. Robinson, P.C. Thomas, J. Veverka, S.L. Murchie, and B. Carcich. The nature of ponded deposits on eros. Nature, 413:396–400, September 2001.

[48] P.G. Rognon, J.N. Roux, M. Naaim, and F. Chevoir. Dense flows of cohesive granular materials. Journal of Fluid Mechanics, 596:21–47, 2008.

[49] Daniel J. Scheeres, Christine M. Hartzell, Paul Sánchez, and Micheal Swift. Scaling forces to asteroid surfaces: The role of cohesion. Icarus, 210:968–984, 2010.

[50] T.E. Sheridan and J. Goree. Observation of dust shedding from material bodies in a plasma. Journal of Geophysical Research, 97(A3):2935–2942, March 1992.

[51] T.E. Sheridan and A. Hayes. Charge fluctuations for particles on a surface exposed to plasma. Applied Physics Letters, 98:091501, 2011.

[52] A.A. Sickafoose, J.E. Colwell, M. Horanyi, and S. Robertson. Experimental levitation of dust grains in a plasma sheath. Journal of Geophysical Research, 107(A11):1408, November 2002.

[53] H. Sierks, P. Lamy, C. Barbieri, D. Koschny, and et al. Images of asteroid 21 lutetia: A remnant planetesimal from the early solar system. Science, 334:487–490, October 2011.

[54] J.R. Smith, N. Hershkowitz, and P. Coakley. Inflection-point method of interpreting emissive probe characteristics. Review of Scientific Instruments, 50(2):210–218, 1979.

[55] Z. Sternovsky, P. Chamberlin, M. Horányi, S. Robertson, and X. Wang. Variability of the lunar photoelectron sheath and dust mobility due to solar activity. Journal of Geophysical Research, 113:A10104, October 2008.

[56] Z. Sternovsky and S. Robertson. Langmuir probe interpretation for plasmas with secondary electrons from the wall. Physics of Plasmas, 11(7):3610–3615, July 2004.

[57] J. M. Sunshine, T.L. Farnham, L.M. Feaga, Olivier Groussin, Frédéric Merlin, Ralph E. Milliken, and Michael F. A'Hearn. Temporal and spatial variability of lunar hydration as observed by the deep impact spacecraft. Science, 326:565–568, October 2009.

[58] Edward Thomas, William E. Amatucci, Christopher Compton, and Brian Christy. Observations of structured and long-range transport in a large volume dusty (complex) plasma experiment. Physics of Plasmas, 9(7):3154–3158, 2002.

[59] X. Wang, M. Horányi, and S. Robertson. Experiments on dust transport in plasma to investigate the origin of the lunar horizon glow. Journal of Geophysical Research, 114:A05103, May 2009.

[60] X. Wang, M. Horányi, Z. Sternovsky, S. Robertson, and G.E. Morfill. A laboratory model of the lunar surface potential near boundaries between sunlit and shadowed regions. Geophysical Research Letters, 34:L16104, August 2007.

[61] H. Yano, T. Kubota, H. Miyamoto, T. Okada, D. Scheeres, Y. Takagi, K.Yoshida, M. Abe, S. Abe, O. Barnouin-Jha, A. Fujiwara, S. Hasegawa, T. Hashimoto, M. Ishiguro, M. Kato, J. Kawaguchi, T. Mukai, J. Saito, S. Sasaki, and M. Yoshikawa. Touchdown of the hayabusa spacecraft at the muses sea on itokawa. Science, 312:1350–1353, 2006.

[62] H.A. Zook and J.E. McCoy. Large scale lunar horizion glow and a high altitude lunar dust exosphere. Geophysical Research Letters, 18(11):2117–2120, November 1991.